Coating of surfaces of composite materials with enzymatically formed biosilica

Dissertation
zur Erlangung des Grades
"Doktor der Naturwissenschaften"

am Fachbereich Biologie
der Johannes Gutenberg-Universität in Mainz

vorgelegt von
Tarek Abbas Ali Elkhooly
geb. am 07.08.1978 in ELDAKAHLIA, Egypt

Mainz, 2014

Dekan:

Erster Berichterstatter:

Zweiter Berichterstatter:

Tag der mündlichen Prüfung: 07.03.2014

This thesis is based on the following 4 research articles, which are classified into two main categories: biotechnological application for chapters 2 and 3, Biomedical application for chapters 4 and 5.

Biotechnological application articles

Wiens M., Link T., Elkhooly T.A., Isbert S. & Müller W.E.G. (2012) Formation of a micropatterned titania photocatalyst by microcontact printed silicatein on gold surfaces. *Chemical communications* 48, 11331–3.

Elkhooly T.A., Müller W.E.G., Wang X., Tremel W., Isbert S., Wiens M. (2014) Bioinspired self-assembly of tyrosinase-modified silicatein and fluorescent core-shell silica spheres, submitted.

Biomedical application articles

Wiens M., Niem T., Elkhooly T.A., Steffen R., Neumann S., Schloßmacher U. & Müller W.E.G. (2013) Osteogenic potential of a biosilica-coated P(UDMA-co-MPS) copolymer. *Journal of Materials Chemistry B* 1, 3339–3343.

Wiens M.*, Elkhooly T.A.*, Wang X., Schröder H.C., Mohamed T.H. & Müller W.E.G., Cellular response on microcrystalline chitosan-polycaprolactone graft immobilized with enzymatically formed biosilica, unpublished.

Contents

Contents

Contents

Chapter 1

Introduction

1.1 Silicon and its metalloid oxides

Silicon is a tetravalent metalloid that is rarely found as a free element in nature. Instead, silicon is most often found surrounded by four oxygen atoms (orthosilicate, SiO_4^{4-}) that bridge to other silicon atoms to form a three dimensional lattice. Silicon was first isolated from its oxides and identified in 1824 by the Swedish chemist Jöns Jacob Berzelius (LeVier et al., 1995). In fact, the large abundance of silicon minerals in the Earth's crust (~ 90%) emphasizes the role of silicon as an element essential to all life processes. Thus, it has attracted much scientific attention in both medical and industrial fields (Perry & Keeling-Tucker, 2000). After calcium carbonate, amorphous hydrated silica (opal) is the second most abundant mineral formed by organisms for strengthening their skeleton, such as in frustules of diatoms, cell walls of certain higher plants, and sponge spicules (Perry & Keeling-Tucker, 2000). However, in the skeleton of vertebrates (bone and cartilage), silicon contributes significantly to the metabolic process of calcium phosphate mineralization by triggering certain signal cascades that lead to an increased bone density (Wang et al., 2012c). For application in humans, amorphous silica is preferentially synthesized by a sol-gel process rather than pyrolysis as nontoxic, biocompatible inorganic particles are produced (Zhang et al., 2012), whose surfaces can be easily functionalized for many subsequent applications such as drug and gene delivery (Sapsford et al., 2013). The term sol is referred to a stable dispersion of solid colloidal particles in organic or aqueous liquid; the particles remain suspended in the liquid phase because of their small size, which slows down their precipitation and agglomeration. On the other hand, the term gel is applied to continuous solid skeleton made of colloidal particles. Functional sol−gel silica particles are generally synthesized *via* hydrolytic polycondensation, at room temperature, of liquid precursors such as silicon alkoxides. Silicon alkoxides are not water soluble and exhibit low polarity of the

Si−O bond; therefore, an organic co-solvent and acid/base catalysis are required for the hydrolysis of their methoxy- or ethoxy groups into silanol groups (equation 1.1). Thereafter, polycondensation occurs by nucleophilic substitution (SN_2) of a Si–OH oxygen atom on another silicon atom, which leads to the formation of a siloxane bond (Si–O–Si) accompanied by releasing water (equation 1.2) or alcohol (equation 1.3).

$$-Si-OR + H_2O \leftrightarrow -Si-OH + ROH \tag{1.1}$$

$$-Si-OH + HO-Si- \leftrightarrow -Si-O-Si- + H_2O \tag{1.2}$$

$$-Si-OR + HO-Si- \leftrightarrow -Si-O-Si- + ROH \tag{1.3}$$

Sol-gel processes have been used mostly for the preparation of amorphous silica and silica doped materials because of their simplicity and capability of controlling the particle sizes, from the nano- to the microscale (Ciriminna et al., 2013). In Nature and at physiological conditions, the sol-gel driven formation of biosilica (i.e., biogenously formed silica) is controlled by the enzyme silicatein, originally isolated from the axial filament of siliceous sponge spicules. Silicatein accelerates both hydrolysis and condensation reactions of siliceous substrates, resulting in a gel-like silica polymer (Cha et al., 1999; Schröder et al., 2012).

1.2 Biosilicification

The term "biomineral" refers to the biological formation of hard skeleton under the control of various biomacromolecules such as silicateins in sponge or silaffins in diatoms. The biologically formed minerals are preferentially deposited as an amorphous phase which undergoes subsequent crystallization onto an organic matrix template leading to highly organized skeletal structures. The biomineralization mechanisms of vertebrates and invertebrates have been extensively reviewed in (Gower, 2008). In the case of silica-based biominerals, the term biosilicification is commonly used to describe the biomineralization process of both unicellular and multicellular organisms, including sponges, diatoms, radiolarians, choanoflagellates, and higher plants (Schröder et al., 2008). The initiation of silica skeleton formation from soluble precursors might occur intracellularly in silica deposition vesicles (diatoms) and silicasomes (marine sponges)

or extracellularly by using the versatile functionalities of a biomacromolecular matrix as template for mineral deposition (Müller et al., 2013d). Many biomolecules were found in biosilicifiying organisms to assist the deposition of silica nanoparticles on the way to developing their exterior skeleton (Dickerson et al., 2008). For instance, silaffin proteins were found in diatoms to have polyamine counterparts that promote non-enzymatically the precipitation of silica spheres by flocculation due to the fusion of oligomeric silicic acid (Gower, 2008). On the contrary, the development and morphogenesis of sponge siliceous spicules is controlled *via* interaction of silicatein subunits with the silicatein interacting protein silintaphin-1 and other sponge specific proteins (Wiens et al., 2009; Schloßmacher et al., 2011). Understanding these mechanisms of biosilicification provides valuable inspiration for the generation of new materials for medical and biotechnological application in the 21st century.

1.3 Siliceous spicule formation in sponges

The mechanism of spicule formation in marine sponge is of particular interest, because of the hierarchical structure of spicules and the related physical properties, including high mechanical strength (Aizenberg et al., 2005) and optical waveguiding (Aizenberg et al., 2004). Thanks to the extensive studies on the marine sponge *Suberites domuncula* by the group of Werner E.G. Müller*,* the essential biomolecules and molecular-biological processes involved in the formation of sponge spicules have been largely elucidated in the last decade (Wang et al., 2012b). Thus, it has been confirmed that spicule formation starts intracellularly in vesicles (silicasomes) within specialized sponge cells (sclerocytes) and is completed extracellularly (Schröder et al., 2007b). Spicule formation proceeds in two directions: (i) axially, *via* elongation of the axial canal that contains the axial filament and (ii) radially, by appositional layering of silica lamellae that are formed, initially, within organic cylinders. Interestingly, growth, morphology and maturation of spicules are genetically controlled by a multi-protein system, which is secreted by specialized, differentiated cells. However, the major role of spiculogenesis is played by the silicatein isoforms (α and β) in such that they catalyze the formation of amorphous hydrated silica nanoparticles and, simultaneously, template their layer-by-layer assembly. Spectroscopic analysis previously revealed that silicatein remains embedded

within the biosilica of spicules (Müller et al., 2010) and interaction was assumed to occur between silicatein serine residues and the silanol group of biosilica and/or condensed silicic acid oligomers (Wang et al., 2012b). Finally, the maturation of siliceous spicules requires water removal resulting in densified compact spicule structures. This syneresis-termed process has been correlated to the elimination of residual water (product of the polycondensation reaction) *via* membrane-associated aquaporin pores (Wang et al., 2012b).

1.4 Self-assembly pathways of axial filaments in sponge spicules

Self-assembly is the autonomous organization of components into patterns or structures without human intervention. Self-assembling processes are common throughout Nature and technology (Whitesides & Grzybowski, 2002). The main focus of this section is to illustrate the complex self-assembly pathway of the axial filament constituent proteins and compare it to the self-assembly studies that have been done on the silicatein-α isoform alone.

1.4.1 *In vivo* self-assembly of sponge proteins to filaments

The *in vivo* assembly of silicatein-α, a protein that is predominantly found in the axial filament of siliceous spicules, is associated with different proteins such as silicatein-β, silntaphin-1, silntaphin-2, and galectin in order to promote the assembly of highly ordered filamentous structures. These proteins organize themselves in stoichiometric manner, thereby presumably preserving their conformational structure and enzymatic activity within the self-assembled axial filament (Grishin & Phillips, 1994; Müller et al., 2013d). Briefly, experimental evidence has been presented that four silicatein-α molecules associate in tetrads (with their catalytic sites exposed outwards), comprising a central opening into which one silicatein-β molecule is inserted (Müller et al., 2007; Wang et al., 2012a). Thereafter, silintaphin-1, which co-localizes with silicatein in the axial filament as well as in protein layers surrounding spicules, acts as a scaffold that mediates assembly of the pentameric aggregates of silicatein-α/silicatein-β (4:1 molar ratio) into filaments *via* fractal intermediates. In this context, it is important to note that

silicatein-α shows an increased silicifying activity in the presence of silintaphin-1 (Schloßmacher et al., 2011). Subsequently, the silicatein-α/calcium binding protein silintaphin-2 is activated by the bone morphogenetic protein-1-like protein (BMP-1) and establishes a complex between silicatein and galectin *via* Ca^{2+} in order to form the organic cylinder of the growing spicules (Wang et al., 2012b). This complex assembly of multiple proteins that are secreted by specialized sponge cells promotes the organization of the axial filament in an axial canal within growing spicules and, concurrently, facilitates the facial silica deposition towards the formation of the first spicular lamella. The enzymatic activity and the biosilica templating ability of silicatein in axial filaments is surprisingly preserved, which might strongly relate to the stoichiometric organization of sponge proteins as well as the protection provided by surrounding biosilica lamellae. Accordingly, in the presence of orthosilicate, the siliceous spicules might feature an interesting self-healing property that allows repairing fractures after exposing the axial filament to soluble silica precursors (Müller et al., 2013d).

1.4.2 *In vitro* self-assembly of recombinant sponge proteins

Silicatein oligomers have the ability to form self-assembled 3D microfilaments with high aspect ratio through the self-organization of 2D fractal intermediates, which can be explained by the diffusion-limited aggregation (DLA) theory. According to this theory, colloidal particles move in a chaotic manner due to the Brownian motion and randomly cluster to form aggregates, as has been first proposed by Witten and Sander (1983). In addition to Brownian diffusion and aggregation, silicatein oligomers interact through hydrophobic interaction sites accessible on the protein surface to form interconnected fractal patterns that exhibit similar geometry to each other. Due to this resemblance in geometry and their dynamic motion, the fractals undergo self-organization and self-condensation into 3D axial filaments. In the axial canal of the siliceous spicule, as mentioned above, silintaphin-1 is required to stabilize the fractal intermediate of nanoscale silicatein aggregates due to the fast rate of the spicules growth (1–10 μm/h) (Müller et al., 2013d). Furthermore, the role of silintaphin-1 in the *in vitro* self-assembly of recombinant silicatein aggregates was demonstrated recently by allowing

aggregation for only very short periods (Schloßmacher et al., 2011): Whereas recombinant silicatein-α alone did not form fractal patterns, addition of a stoichiometric ratio of recombinant silintaphin-1 to silicatein-α resulted in fractally patterned aggregates, whose size increased with time. This suggests that silicatein-α assembly *in vitro* requires either a promoter to enhance and enlarge the size of its oligomeric aggregates or a longer period to allow an increased aggregate size. Indeed, the protein aggregate size seems to be essential in the assembly of fractal clusters in general (Van der Linden & Venema, 2007). Furthermore, the assembly of recombinant silicatein occurs only in the absence of the silicatein pro-peptide sequence, which has been shown to effectively inhibit silicatein aggregation and filament assembly (Müller et al., 2013c). In previous studies, sponge axial filaments were disassembled *in vitro* into silicatein fractals and oligomers that, subsequently, were transferred to conditions that allow a reassembly process (Müller et al., 2007; Murr & Morse, 2005). It is noteworthy mentioning that similarities in the fractal assembly of biomacromolecules were found in the case of proteins (Khire et al., 2010), peptides (Wang & Chau, 2009), and polysaccharides (Zhao et al., 2010). However, the difference to silicatein fractals is that these undergo self-organization and self-condensation to form filaments as proposed previously (Murr et al., 2009), compared to the assembly of the aforementioned biomacromolecules that ceases at the fractal stage.
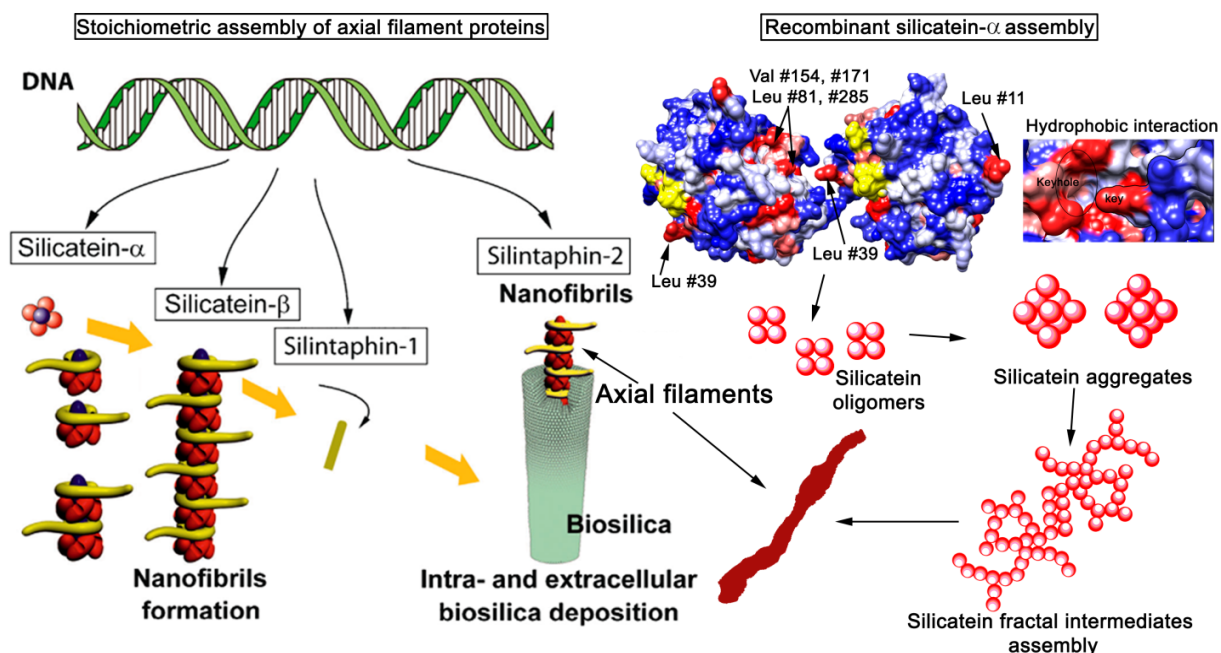
Scheme 1.1 Suggested *in vivo* self-assembly mechanisms of axial filament proteins expressed by sponge cells and the biomimetic *in vitro* self-assembly of recombinant silicatein-α. The left panel outlines the enzymatic synthesis of sponge spicules according to the reference (Wang et al., 2012b; with permission): After their expression, silicatein-α and silicatein-β monomers oligomerize in a stoichiometric manner by which four silicatein-α molecules form a tetramer, allowing one silicatein-β molecule to insert in the middle of the tetrad. During axial assembly of the proteinaceous filament, these pentameric oligomers are stabilized longitudinally by the silicatein interactor protein silintaphin-1. Additionally, activated silintaphin-2 provides Ca^{2+} ions required for complex formation between the silicatein oligomers and galectin, the main components of the organic cylinder surrounding the growing spicules. The right panel shows the hydrophobic domains on the silicatein-α surface that promote protein assembly in an aqueous media. The model of silicatein-α derived from the crystal structure of cathepsin L (PDB, ID code 1ICF) shows two anchors of leucine residues, acting as "key" and clusters of hydrophobic amino acid residues as "lock". As these hydrophobic clusters are present on the solvent-accessible surface of silicatein, they promote protein oligomerization by non-covalent driving forces, forming bigger aggregates with time. These aggregates will further assemble into filaments *via* formation of fractal intermediates as proposed by previous computer simulation (Murr et al., 2009).

1.5 Silicatein-α structure and activity

1.5.1 Silicatein-α secondary structure

Silicatein-α, the most abundant silicatein subunit in axial filaments of the spicules of the marine sponge *Suberites domuncula* is similar in sequence to the protease cathepsin L with an overall identity of 52% and a similarity of 65% in the amino acid residues (Fairhead et al., 2008, Cha et al., 1999). The major differences between the two sequences are the presence of a large number of hydroxyl containing residues (serine, threonine, and tyrosine) in silicatein-α and the substitution of the catalytic cysteine (C25) in cathepsin L for serine (S25) in silicatein-α (Schröder et al., 2007a; Fairhead et al., 2008). The structural studies on either native silicatein-α or recombinant silicatein-α after its folding are still in their early stages due to the harsh procedures required for the extraction of the former one from spicules or the low concentration available after folding of the later one (Patwardhan et al., 2010). However, the highly soluble monomer of cathepsin L exhibits 31% α-helices and 20% β-sheets in its secondary structure (Protein Data Bank ID: 3HHA) (Gunčar et al., 1999). Otherwise, FTIR spectroscopy of the axial filament of spicules of another marine sponge species, *T. aurantia*, revealed that both α-helix and β-sheet structures are present but that the latter structures are predominant (Croce et al., 2004). This structural conflict might arise from the presence of multiple proteins that contribute to the assembly of axial filaments (Wang et al., 2012b), as it is almost impossible to isolate only silicatein-α of filaments, without protein denaturation. Therefore, recombinant silicatein was expressed in *Escherichia coli* by cloning the genes from *S. domuncula* (Krasko et al., 2000) and *T. aurantia* (Cha et al., 1999) for catalytic functional and structural studies. Recombinant silicatein prepared in bacteria is insoluble (in inclusion bodies) and harsh isolation and folding conditions are required to obtain it in a soluble manner. Several folding methods, including dilution, dialysis, diafiltration, gel filtration, and immobilization onto a solid support may be employed to remove or reduce excess denaturing and reducing agents, generally allowing recombinant proteins to renature/fold (De Bernardez Clark, 1998). Purified inclusion bodies from silicatein-α were often folded by dialysis at low concentration

against refolding buffer that contains reduced and oxidized glutathione (GSH/GSSG) as oxido shuffling reagents (Natalio et al., 2010a; Müller et al., 2013c; Müller et al., 2005). However, low yield of native recombinant silicatein was obtained by dialysis due to the necessity to maintain the concentration of solubilized inclusion bodies as low as possible in order to avoid the aggregation of partially folded silicatein intermediates during refolding. Furthermore, a non-denaturing concentration of urea is occasionally used as an intermediate solvent to stabilize monomers of the folded recombinant silicatein. It has been recently shown that the pro-peptide sequence of silicatein and a 1.5 M urea concentration have an inhibitory role of the monomer self-assembly into well-defined fractals (Müller et al., 2013c). The low yield of folded silicatein as well as the high rate of its aggregation in the absence of chaotropic agents usually hampers structural studies of silicatein-α monomers. Therefore, a new folding methodology is established in this study for mature silicatein-α (i.e., without propeptide; chapter 3) to minimize its aggregation during refolding and to maximize the concentration of soluble recombinant silicatein-α required for folding and subsequent structural studies. Such a high yield of soluble recombinant silicatein-α has not only allowed conformational studies (here conducted for the first time *via* Raman spectroscopy) but is also fundamental to obtain supramolecular self-assembled silicatein filaments for future biotechnological or medical application. It is noteworthy mentioning that so far the closest conformational study of silicatein-α was obtained by resolving the crystal structure of recombinant silicatein-α/cathepsin L chimeras termed 4SER (Fairhead et al., 2008). The secondary structure components of 4SER were calculated from X-ray crystallographic structures indicating 27% α-helix and 23% β-sheet structures. This finding is also in contrast to the aforementioned predominant β-sheet structures found in the axial filaments of siliceous spicules. Actually, in the 4SER model, the hydrophobic amino acid residues on the silicatein surface that promote silicatein self-assembly in aqueous media (Murr & Morse, 2005) had not been mutated, as they might influence structural transition to a predominantly β-sheet during silicatein assembly.

1.5.2 Silicatein-α substrates and activity mechanism

Enzymes are astonishing catalysts acting on their specific substrates to form products under physiological conditions that usually suppress chemical reactivity (e. g. aqueous environment, electrolytes, pH, ambient pressure and temperature). Most synthetic catalysts are also inferior to biological catalysts in at least four other respects (Purich, 2010), as they: (i) are less efficient at physiologic temperature, low pressure, and neutral pH; (ii) are relatively unselective; (iii) rarely display sufficiently high chiral recognition, a property that greatly limits their use in preparing optically active biomolecules; and (iv) are not regulated by feedback activators and/or inhibitors. Enzyme-substrate specificity and intermediate complex formation are common features in all enzymes. In this context, silicatein belongs to those enzymes that have a broad substrate specificity, as it can act on a relatively broad range of different substrates to produce various metal(loid) oxides, which might be attributed to its relatively flexible active center and the similarity in size and charge of the electrophilic centers of the substrate molecules (André et al., 2012). Active sites can undergo major conformational changes upon substrate binding, especially when some parts of the site are located in flexible loops or at the beginning or the end of helical and sheet secondary structures. The conformational change of the enzyme active site upon exposure to different substrates is a well-established phenomenon in many enzymes, e. g. thioesterase/protease I with a catalytic triad similar to that of silicatein, except for the replacement of asparagine by aspartate (Huang et al., 2001). The enzyme silicatein, which is related to cathepsins (cysteine proteases), comprises the catalytic triad (Ser-His-Asn) in which serine (Ser) replaces cysteine (Cys) of cathepsins. The thiol and hydroxyl functional groups of Cys and Ser, respectively, are very reactive nucleophiles that are commonly found in the active site of proteases, close to histidine which act as acid/base catalysts that mediate a nucleophilic attack to form an enzyme-substrate intermediate *via* covalent bonding (Bartlett et al., 2002). Site-directed mutagenesis experiments show that the specific serine (Ser26) and histidine (His165) residues are crucially involved in the catalysis of silica polymerization with silicon alkoxides as substrate (Zhou et al., 1999). The hydroxyl containing amino acid residues (serine

cluster) close to the active site of silicatein-α are not directly involved in its catalytic activity but it was postulated that they bind to the enzymatically synthesized silica, thereby embedding silicatein within silica (Wang et al., 2012a). There are two critical parameters that have been taken into consideration for the silicatein-catalyzed reaction (Müller et al., 2013a). Firstly, low enzyme concentrations (~ 10μg/ml) were often used for the activity assays to avoid denaturation of the enzyme due to its fast oligomerization/aggregation in aqueous solution as well as to avoid the non-enzymatically silica polymerization accelerated by hydroxyl-carrying amino acid on the silicatein surface at high enzyme concentration. Secondly, the concentration of orthosilicate as natural substrate for silicatein should be maintained at less than 1-2 mM to prevent auto-polycondensation of silica at neutral pH. Furthermore, the concentration of orthosilicate in sea water, fresh water, and soil water was found to be less than 100 ppm (1mM; Belton et al., 2012). The silicatein catalytic triad can accommodate many metal(loid) alkoxide precursors, however, the precursors should be chosen carefully because most of them are very unstable and will spontaneously react with water at room temperature to form an amorphous metal(loid) oxide precipitate (André et al., 2012). Hexafluoro metal complexes including hexafluorozirconate (ZrF_6^{2-}), hexafluorostannate (SnF_6^{2-}), and barium fluorotitanate ($BaTiF_6$) were chosen as stable substrates for silicatein-α, which mediates enzymatically the formation of zirconium dioxide (ZrO_2) (Tahir et al., 2005), tin dioxide (SnO_2) (André et al., 2011b) and barium oxofluorotitanate ($BaTiOF_4$) (Brutchey et al., 2006), respectively, at ambient condition. The conversion of the abovementioned precursors is based on the nucleophilic attack of the serine residue in the silicatein active site at the metal cation, which is surrounded by six fluorine anions, resulting in hydroxyl groups that subsequently undergo condensation to form non-biological metal oxides. For the enzymatic synthesis of biosilica, several precursors have been used as substrate, including non-biological substrates such as tetraethyl orthosilicate (TEOS) (Cha et al., 1999), tetramethyl orthosilicate (TMOS) (Rai & Perry, 2012) and sodium metasilicate (Wiens et al., 2010a) as well as pre-hydrolyzed TEOS (orthosilicate) (Müller et al., 2013c) as a putative biological substrate. For silicon alkoxide hydrolysis, Hydrogen-bonding between the imidazole nitrogen of histidine and the hydroxyl of the active-site serine is assumed to

increase the nucleophilicity of the serine oxygen, stimulating its attack on the silicon atom of the silicon alkoxide substrate. Nucleophilic attack on the silicon displaces ethanol, resulting in a covalent bond between the serine and the metal cation. The resultant transitory protein-substrate intermediate is stabilized as a pentavalent silicon species *via* a donor bond from the imidazole nitrogen atom. The completion of the first alkoxide bond hydrolysis is accomplished by adding water molecule. (Cha et al., 1999). For polycondensation of orthosilicic acid molecules, as described in the alkoxide hydrolysis, the condensation process starts with nucleophilic attack by serine on the partially positive silicon forming pentavalent intermediate (Schröder et al., 2012). After water release, the dimerization of silicic acid molecules is enhanced by histidine in the active center while, serine remains covalently bounded to the silicon atom. The imidazole nitrogen of histidine acts as base and acid catalysis by accepting a proton from the silanol group (increase its nucleophilicity towards the silicon atom of the second silicic acid molecule) or by donating a proton to displace water molecule required for the formation of Si-O-Si siloxane bonds, respectively. Finally, the termination of bio-polycondensation reaction was postulated by forming highly reactive trisiloxane ring species which have higher reactivity than the silicic acid monomers and promote further condensation reaction (Schröder et al., 2012, Wang et al., 2012b). On the other hand, for the silicatein mediated synthesis of biotitania, titanium bis-(ammonium-lactato)-dihydroxide (TiBALDH) was chosen as suitable substrate on many occasions (Tahir et al., 2005, Sumerel et al., 2003, Natalio et al., 2010b). The high stability TiBALDH, as compared to Ti alkoxides, towards hydrolytic attack at neutral pH stems from its structure: TiBALDH is a chelate compound in which all six-coordinate positions of Ti are occupied (Möckel et al., 1999). The formation of anatase crystals from TiBALDH precursor in aqueous media usually accomplished by thermohydrolysis at temperature above 100°C (Möckel et at., 1999) or by base hydrolysis at pH above 9 (Kinsinger et al., 2010). The octahedral Ti cation coordination in the TiBALDH complex contains two bidentate lactato ligands in the x-y plane and two hydroxyls along the z-axis. At neutral environment, the stability of lactato ligands of TiBALDH allows condensation to occur only through the two existing hydroxyls along the z-axis resulting in rutile phase. While, at basic medium containing NaOH, hydroxide ions cleave

TiBALDH by nucleophilic addition to either the Ti cation or the lactato group, forming an ammonium lactate byproduct. The increase of the hydroxide ions concentration at pH>9 enhances the rate of TiBALDH hydrolysis, leading to condensation along x-y planes, forming anatase, as observed in previous study (Kinsinger et al., 2010). Based on the former study, the formation of anatase phase is not possible at neutral pH, as it requires cleavage of the lactato ligands bound to the titanium cation by nucleophilic attack. In this respect, serine-histidine residues in silicatein active center can mediate TiBALDH hydrolysis, expecting the growth of anatase phase. The serine-histidine catalysis mechanism on the hydrolysis of TiBALDH was suggested previously by using peptide sequences that contain two serine-histidine pairs (Zhao et al., 2012). The titanium cation in TiBALDH undergoes nucleophilic attack by the electronegative oxygen of the Ser residue, in the meanwhile, the histidine nitrogen accepts the hydrogen from the serine hydroxyl group, thus enhancing its nucleophilicity and coordinating the attack of the Ti atom. The pKa of Histidine ~6 is close to neutral thus making it the most effective candidate for general acid or base because it can either donate or accept protons. After displacing of ammonium lactate, the transitory silicatein-TiBALDH intermediate is stabilized through a donor bond from the imidazole nitrogen atom. In order to complete the hydrolysis cycle, the pair of electron on the histidine nitrogen accepts the hydrogen from water molecule and the hydroxyl group of water attacks the Ti cation leading to formation of (Ti–O) bond. By donating the hydrogen on the His back to serine, the enzyme active center is regenerated. As described above, the condensation reaction of the hydrolyzed Ti–OH groups proceed in x-y axis between the edges of TiO_6 octahedra, yielding anatase. The aforementioned silicatein catalytic activity is not limited to *in vitro* conditions: In the culture of *S. domuncula* primmorphs (aggregates of proliferating cells formed after dissociation of sponge tissue) incubation with TiBALDH led to the formation of biotitania that was found co-localized with sponge spicules (Natalio et al., 2010b).

Non-enzymatically, silicatein also reduces tetrachloroauric acid $HAuCl_4$ to gold nanoparticles, however, this reduction was attributed to tyrosine residues outside of the active site that can donate electrons required for the reduction of $AuCl_4^-$ to Au^0 (Tahir et al., 2006). In addition to the anabolic activity of silicatein as silica polymerase, silicatein

may also have catabolic and proteolytic activities, given that it is able to cleave (i) bis(p-aminophenoxy)-dimethylsilane in the function of a silica esterase (Müller et al., 2008), releasing p-aminophenol and (alkoxyl)-monosilane and (ii) the fluorescent peptide Z-Phe-Arg-MCA in the function of a serine protease, releasing an aminomethyl coumarin fluorophore (Polini et a., 2011).

1.6 Silicatein-α immobilization strategies

In the biotechnological industry, enzyme immobilization on material surfaces is beneficial in terms of catalyzing versatile chemical reactions at mild pH, temperature and pressure conditions. Enzyme immobilization is only possible on a surface that has binding sites, which are able to form chemical bonds with the protein. Therefore, often surface modifications are required to introduce functional groups, defect sites and extra reactive layers on the matrix surface, which can be accomplished by grafting, etching and coating, respectively, without actually affecting the bulk properties (Jochems et al., 2011). On the other hand, the recombinant enzymes can be genetically bioengineered to introduce polypeptide sequences (so called affinity tags) that are e.g. rich in cysteine, glutamate and arginine residues for direct affinity immobilization on different substrates in shortest time without surface modification prior to enzyme immobilization. Furthermore, a hexa-histidine tag can be used as a metal chelating anchor for indirect immobilization of the recombinant protein on substrata after functionalizing their surfaces with organic compounds bearing nitrilotriacetic acid residues that couple the enzyme to the substratum *via* metal (e.g. Ni^{2+}) complexes. By using aforementioned methodologies, either by functionalizing substrate surfaces or by bioengineering the recombinant silicatein prior to its immobilization, silicatein was immobilized previously onto numerous surfaces to catalyze various metal (loid) oxides at ambient conditions forming hybrid inorganic/inorganic and inorganic/organic materials for the development of both biotechnological and biomedical applications. Scheme 1.2 represents the previously published immobilization methodologies for recombinant silicatein on different substrates to facilitate the formation of biogenic inorganic particles (using different soluble precursors) or to promote the assembly of inorganic–organic fibers.
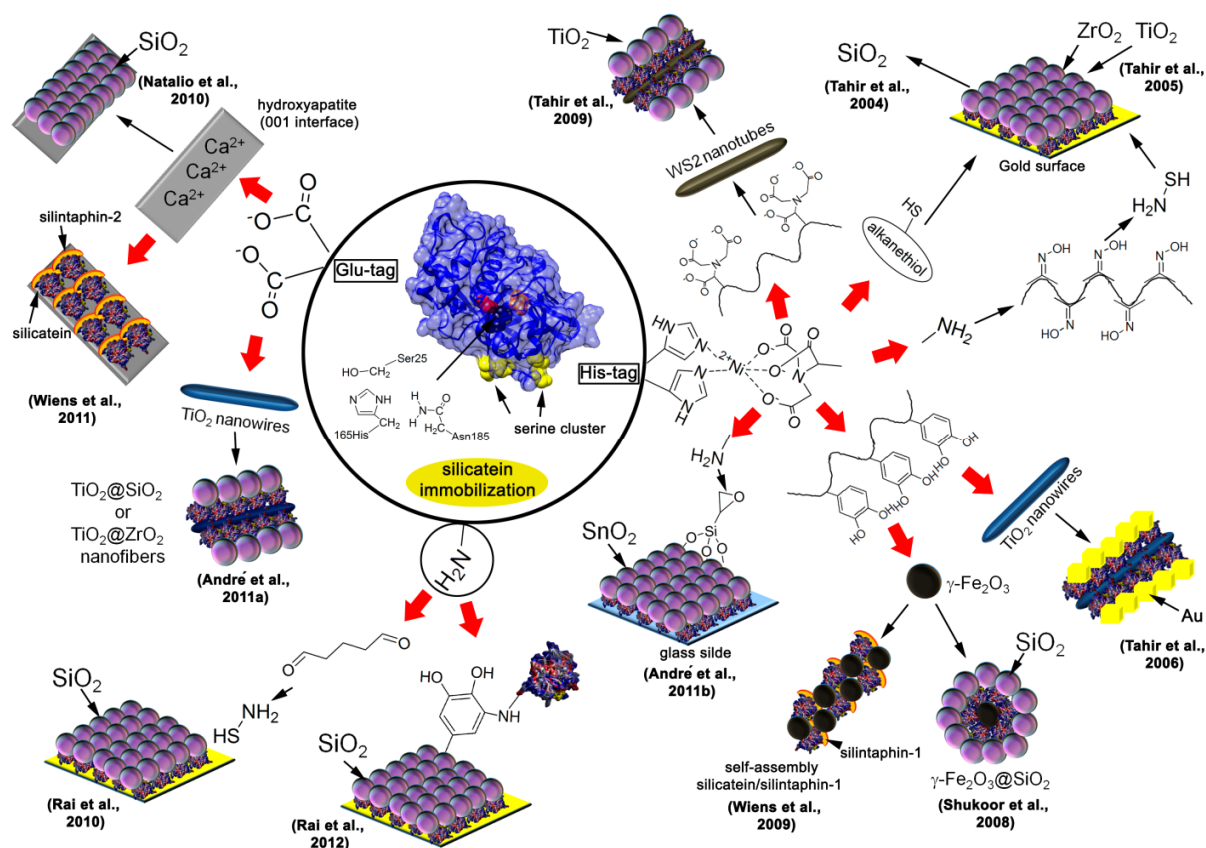
Scheme 1.2 Silicatein immobilization methodologies based on twelve previous research articles. The immobilization of silicatein on solid surfaces is based on the genetic modification of the native silicatein sequence to obtain a hybrid protein that carries one or two affinity tags, (i) a C-terminal hexa-histidine or (ii) an N-terminal octa-glutamate tag. Alternatively, amine groups of native lysine residues were used to immobilize the enzyme. The spherical balls in the scheme represent various metal(loid) oxides that synthesized enzymatically with recombinant silicatein-α such as silicon dioxide (SiO_2), titanium dioxide (TiO_2), zirconium oxide (ZrO_2), tin dioxide (SnO_2).

For indirect immobilization of recombinant His-tagged silicatein onto gold surfaces *via* stable chelator-metal complexes, the target gold surface was coated with thiol-bearing organic compounds such as N-[Nα,Nα-bis(carboxymethyl)-L-lysine]-12-mercaptododecanamide (Tahir et al., 2004) or cysteamine (Tahir et al., 2005). Thereafter, the carboxylate groups of the nitrilotriacetic acid (NTA) terminus remain free for Ni^{2+} and His-tag protein complexation. In other approaches with gold surfaces, free

amine groups of silicatein were used for covalent binding to surface aldehyde groups (Rai et al., 2010), the phenyl ring of 3,4-dihydroxyphenylalanine (DOPA), or a DOPA bearing decapeptide *via* Michael substitution reaction (Rai et al., 2012). Furthermore, the active ester polymer pentafluorophenyl acrylate (PFA) modified with NTA residues was used as an intermediate layer between His-tagged silicatein and tungsten disulfide (WS_2) nanotubes (Tahir et al., 2009). Various polymers containing DOPA and NTA groups were used on many occasions to mediate the binding to TiO_2 nanowires (Tahir et al., 2006) and maghemite (γ-Fe_2O_3) nanoparticles (Shukoor et al., 2008, Wiens et al., 2009) through bidentate coordination. In order to reduce the number of laborious reaction steps, recombinant silicatein-α was immobilized onto titania nanowires (André et al., 2011a) and hydroxyapatite (Natalio et al., 2010a, Wiens et al., 2011) with a C-terminal glutamate-tag. The carboxylate groups of this octo-glutamate tag bind efficiently to titanium oxide surfaces through different binding modes (ester-like linkage, bridging, or chelating) or to calcium rich interfaces of hydroxyapatite crystals *via* coordination. Silicatein was also immobilized on glass slides by using a silane coupling reagent terminated with silanol groups, forming siloxane bonds with the glass surface and epoxy groups that react with Nα,Nα-Bis(carboxymethyl)-L-lysine hydrate, afterwards the free tricarboxylic acid of the former compound (NTA) support the chelating efficency of His tags with Ni^{2+} (André et al., 2011b). Finally, soft lithography was used previously for patterning recombinant silicatein-α by physisorption on Si surfaces in order to catalyze the formation of patterned and insulating layers of silicon dioxide under mild conditions (Polini et al., 2011).

1.7 Silicatein analogues for biomimetic mineralization

Biomimetic mineralization analogues are designed to transfer the principles of biomineralization from Nature to the synthesis of new materials (Xu et al., 2007). The understanding of the mechanisms of both enzymatic biosilicification and self-assembly of axial filament proteins has greatly enhanced the development of biomimetic approaches. For instance, a block copolypeptide poly(L-cysteine30-b-L-lysine200) was designed previously to mimic the catalytic properties of silicatein (Cha et al., 2000). Thus, the oxidation of the cysteine sulfhydryl groups allowed the formation of hard silica

spheres and well-defined columns of amorphous silica from soluble precursors. In a different approach, another catalytically active block copolymer poly(2-vinylpyridine-b-1,2-butadiene) was synthesized, which mimiced both serine and histidine residues of the silicatein-α active site (Adamson et al., 2007). This non-peptide copolymer not only catalyzed the hydrolysis of TEOS, leading to the formation of silica, but also confirmed the critical role of serine and histidine residues for the catalytic activity of silicatein-α. In this context, the close proximity of the catalytic functional groups must be taken in consideration for successfully designing synthetic polymers as functional analogues to silicatein-α. In the natural enzyme, the active site contains an imidazole base and a hydroxyl nucleophile in the correct and optimal orientation to catalyze hydrolysis and condensation. In a further biomimetic approach, the distance between the catalytically active functional groups has been proven to be essential by using homopolymers of polyisoprene, hydroxylated polyisoprene, poly(2-vinylpyridine), and poly(vinyl alcohol) instead of poly(2-vinylpyridine-b-1,2-butadiene). No silica formation was observed in the former study, confirming that the hydrolysis of TEOS was caused by hydrogen bonding between hydroxyl and imidazole groups due to the close proximity of the two polymer blocks (Hire et al., 2013). Therefore, kinetically controlled catalytic hydrolysis and polycondensation could be achieved through development of synthetic analogs of the enzyme responsible for biosilicification.

1.8 Potential applications of silicatein and biosilica

Native and recombinant silicatein-α are able to convert a wide spectrum of metal(loid) alkoxide precursors/substrates, catalyzing the formation of various metal(loid) oxides/products. Following catalysis, silicatein remains embedded within the inorganic matrix, thereby providing specific recognition sites that promote the assembly of highly ordered structure. In addition to the versatile potential of the enzymatically formed inorganic particles (that might be explored for various biotechnological and biomedical applications), the particular advantage of immobilized silicatein is that it offers nucleation sites, which can lower the activation barrier to heterogeneous (solid-solution) nucleation.

1.8.1 Biotechnological applications

Biotechnological application of silicatein is highly dependent on the type of enzyme substrate and the resulting product. For instance, biotitania (anatase phase) synthesized by recombinant silicatein from the titania precursor; titanium bis-(ammonium-lactato)-dihydroxide is important for environmental and energy-related applications, especially for photocatalysis, solar cell devices, sensors, catalyst supports, etc. (Liu et al., 2011). On the other hand, biosilica synthesized by silicatein from the silica precursor; tetraethyl orthosilicate offers electrically insulating properties, serving as dielectric layer for microelectronics (Pagliara et al., 2012; Polini et al., 2011). Moreover, the transparent tin oxide (SnO_2) particles that were obtained by combination of silicatein with the tin precursor; Sodium hexafluorostannate on glass slides have a potential application in optoelectronics due to their high electrical conductivity and high optical transparency in the visible spectrum (André et al., 2011b). Furthermore, different multifunctional core/shell inorganic particles were synthesized by immobilizing recombinant silicatein on an inorganic core such as iron oxide particles (Shukoor et al., 2008) or titanium nanowires (André et al., 2011a). The immobilized enzyme then mediated the formation of different inorganic shells by using different substrates (Scheme 1.2). Last but not least, recombinant silicatein and silintaphin-1 were employed for the directional self-assembly of 3D structures that templated the deposition of various inorganic nanoparticles to artificial microspicules (Wiens et al., 2009).

1.8.2 Biomedical applications

In bone tissue engineering, silica-based materials including bioactive glass, bioactive silicate ceramics, polymer-silica composites, collagen-silica fibers, silica substituted hydroxyapatite, and biogenic silica have often revealed osteoconductive, osteoproductive and osteoinductive properties (Heinemann et al., 2013, Wu & Chang, 2013, Hoppe et al., 2011, Pietak et al., 2007, Arcos & Vallet-Regí, 2010, Wang et al., 2012c). Focusing on the enzymatically synthesized biosilica, several studies demonstrated that it enhances adhesion, proliferation, differentiation, and gene expression in osteoblast like cells (SaOS-2, sarcoma osteogenic non-transformed cell

line derived from primary osteosarcoma cells). It has been experimentally proven that biosilica causes an increase in hydroxyapatite deposition (Wiens et al., 2010b) as well as an increased transcription of the osteoprotegerin (OPG) gene, while no effect was detected on the expression rate of the osteoclast receptor activator for NF-$_k$B ligand (RANKL). It has been shown that encapsulation of biosilica inside alginate hydrogel increased the mineralization capacity and hydroxyapatite nodule formation by SaOS-2 cells (Müller et al., 2013b). The osteogenic effect of silica particles on osteoblast cells and bone formation is well established *in vivo* and *in vitro* (Beck et al., 2012), however, the capability of silicatein to mediate silica formation at physiological condition and its simultaneous interaction with biosilica might provide a protein layer on the particles' surface serving as ion nucleators and enhancing the mineralization capacity of the bone forming cells. It can be concluded from the different research approaches (Wang et al., 2012c) that biosilica appears to have the potential to act as promising additive or coated layer for many biomaterial scaffolds to enhance osteogenicity and bone formation.

1.9 References

Adamson D.H., Dabbs D.M., Pacheco C.R., Giotto M.V., Morse D.E. & Aksay I.A. (2007). Non-Peptide Polymeric Silicatein α Mimic for Neutral pH Catalysis in the Formation of Silica. *Macromolecules* 40, 5710-5717.

Aizenberg J., Sundar V.C., Yablon A.D., Weaver J.C. & Chen G. (2004). Biological glass fibers: correlation between optical and structural properties. *Proceedings of the National Academy of Sciences* 101, 3358-3363.

Aizenberg J., Weaver J.C., Thanawala M.S., Sundar V.C., Morse D.E. & Fratzl P. (2005). Skeleton of *Euplectella sp*.: structural hierarchy from the nanoscale to the macroscale. *Science* 309, 275-278.

André R., Tahir M.N., Link T., Jochum F.D., Kolb U., Theato P., Berger R., Wiens M., Schröder H.C., Müller W.E.G. & Tremel W. (2011 a). Chemical Mimicry: Hierarchical 1D TiO2@ ZrO2 Core−Shell Structures Reminiscent of Sponge Spicules by the Synergistic Effect of Silicatein-α and Silintaphin-1. *Langmuir 27*, 5464-5471.

André R., Tahir M.N., Natalio F. & Tremel W. (2012). Bioinspired synthesis of multifunctional inorganic and bio-organic hybrid materials. *FEBS Journal* 279, 1737-1749.

André R., Tahir M.N., Schröder H.C., Müller W.E.G. & Tremel W. (2011 b). Enzymatic synthesis and surface deposition of tin dioxide using silicatein-α. *Chemistry of Materials* 23, 5358-5365.

Arcos D. & Vallet-Regí M. (2010). Sol–gel silica-based biomaterials and bone tissue regeneration. *Acta Biomaterialia* 6, 2874-2888.

Bartlett G.J., Porter C.T., Borkakoti N. & Thornton J.M. (2002). Analysis of catalytic residues in enzyme active sites. *Journal of molecular biology* 324, 105-121.

Beck Jr G.R., Ha S.W., Camalier C.E., Yamaguchi M., Li Y., Lee J.K. & Weitzmann M.N. (2012). Bioactive silica-based nanoparticles stimulate bone-forming osteoblasts, suppress bone-resorbing osteoclasts, and enhance bone mineral density in vivo. *Nanomedicine: Nanotechnology, Biology and Medicine* 8, 793-803.

Belton D.J., Deschaume O. & Perry C.C. (2012). An overview of the fundamentals of the chemistry of silica with relevance to biosilicification and technological advances. *FEBS Journal* 279, 1710-1720.

Brutchey R.L., Yoo E.S. & Morse D.E. (2006). Biocatalytic synthesis of a nanostructured and crystalline bimetallic perovskite-like barium oxofluorotitanate at low temperature. *Journal of the American Chemical Society* 128, 10288-10294.

Cha J.N., Shimizu K., Zhou Y., Christiansen S.C., Chmelka B.F., Stucky G.D. & Morse D.E. (1999). Silicatein filaments and subunits from a marine sponge direct the polymerization of silica and silicones in vitro. *Proceedings of the National Academy of Sciences 96*, 361-365.

Cha J.N., Stucky G.D., Morse D.E. & Deming T.J. (2000). Biomimetic synthesis of ordered silica structures mediated by block copolypeptides. *Nature* 403, 289-292.

Ciriminna R., Fidalgo A., Pandarus V., Béland F., Ilharco L.M. & Pagliaro M. (2013). The Sol–Gel Route to Advanced Silica-Based Materials and Recent Applications. *Chemical Reviews* 113, 6592−6620.

Croce G., Frache A., Milanesio M., Marchese L., Causà M., Viterbo D., Barbaglia A., Bolis V., Bavestrello G., Cerrano C., Benatti U., Pozzolini M., Giovine M. & Amenitsch H. (2004). Structural characterization of siliceous spicules from marine sponges. *Biophysical journal* 86, 526-534.

De Bernardez Clark E. (1998). Refolding of recombinant proteins. *Current Opinion in Biotechnology* 9, 157-163.

Dickerson M.B., Sandhage K.H., & Naik R.R. (2008). Protein-and peptide-directed syntheses of inorganic materials. *Chemical reviews* 108, 4935-4978.

Fairhead M., Johnson K.A., Kowatz T., McMahon S.A., Carter L.G., Oke M., Liu H., Naismith J.H. and van der Walle C.F. (2008). Crystal structure and silica condensing activities of silicatein α–cathepsin L chimeras. *Chemical Communications* (15), 1765-1767.

Gower L.B. (2008). Biomimetic model systems for investigating the amorphous precursor pathway and its role in biomineralization. *Chemical reviews* 108, 4551-4627.

Grishin N.V. & Phillips M.A. (1994). The subunit interfaces of oligomeric enzymes are conserved to a similar extent to the overall protein sequences. *protein Science* 3, 2455-2458.

Gunčar G., Pungerčič G., Klemenčič I., Turk V. & Turk D. (1999). Crystal structure of MHC class II-associated p41 Ii fragment bound to cathepsin L reveals the structural basis for differentiation between cathepsins L and S. *The EMBO journal* 18, 793-803.

Heinemann S., Coradin T. & Desimone M.F. (2013). Bio-inspired silica–collagen materials: applications and perspectives in the medical field. *Biomaterials Science* 1, 688–702.

Hire C.C., Oyer A.J., Macek G.E., Bento J.L. & Adamson D.H. (2013). Directed formation of silica by a non-peptide block copolymer enzyme mimic. *Journal of Materials Chemistry B* 1, 1977–1984.

Hoppe A., Güldal N.S. & Boccaccini A.R. (2011). A review of the biological response to ionic dissolution products from bioactive glasses and glass-ceramics. *Biomaterials* 32, 2757-2774.

Huang Y.T., Liaw Y.C., Gorbatyuk V.Y. & Huang T.H. (2001). Backbone dynamics of *Escherichia coli* thioesterase/protease I: evidence of a flexible active-site environment for a serine protease. *Journal of molecular biology* 307, 1075-1090.

Jochems P., Satyawali Y., Diels L. & Dejonghe W. (2011). Enzyme immobilization on/in polymeric membranes: status, challenges and perspectives in biocatalytic membrane reactors (BMRs). *Green chemistry* 13, 1609-1623.

Khire T.S., Kundu J., Kundu S.C., & Yadavalli V.K. (2010). The fractal self-assembly of the silk protein sericin. *Soft Matter* 6, 2066-2071.

Kinsinger N.M., Wong A., Li D., Villalobos F. & Kisailus D. (2010). Nucleation and Crystal Growth of Nanocrystalline Anatase and Rutile Phase TiO$_2$ from a Water-Soluble Precursor. *Crystal Growth & Design* 10, 5254-5261.

Krasko A., Lorenz B., Batel R., Schröder H.C., Müller I.M. & Müller W.E.G. (2000). Expression of silicatein and collagen genes in the marine sponge *Suberites domuncula* is controlled by silicate and myotrophin. *European Journal of Biochemistry*, 267, 4878-4887.

LeVier R.R., Harrison M.C., Cook R.R. & Lane T.H. (1995). What is silicone?. *Plastic and reconstructive surgery* 92, 12-167.

Liu S., Yu J. & Jaroniec M. (2011). Anatase TiO$_2$ with dominant high-energy {001} facets: Synthesis, properties, and applications. *Chemistry of Materials* 23, 4085-4093.

Möckel H., Giersig M. & Willig F. (1999). Formation of uniform size anatase nanocrystals from bis (ammonium lactato) titanium dihydroxide by thermohydrolysis. *Journal of Materials Chemistry* 9, 3051-3056.

Müller W.E.G., Boreiko A., Schloßmacher U., Wang X., Tahir M.N., Tremel W., Brandt D., Kaandorp J.A. & Schröder H.C. (2007). Fractal-related assembly of the axial filament in the demosponge *Suberites domuncula*: Relevance to biomineralization and the formation of biogenic silica. *Biomaterials* 28, 4501-4511.

Müller W.E.G., Rothenberger M., Boreiko A., Tremel W., Reiber A. & Schröder H.C. (2005). Formation of siliceous spicules in the marine demosponge *Suberites domuncula*. *Cell and tissue research* 321, 285-297.

Müller W.E.G., Schröder H.C., Burghard Z., Pisignano D. & Wang X. (2013 a). Silicateins—A Novel Paradigm in Bioinorganic Chemistry: Enzymatic Synthesis of Inorganic Polymeric Silica. *Chemistry-A European Journal* 19, 5790-5804.

Müller W.E.G., Schröder H.C., Feng Q., Schloßmacher U., Link T. & Wang X. (2013 b). Development of a morphogenetically active scaffold for three-dimensional growth of bone cells: biosilica–alginate hydrogel for SaOS-2 cell cultivation. *Journal of tissue engineering and regenerative medicine* DOI: 10.1002/term.1745

Müller W.E.G., Schröder H.C., Muth S., Gietzen S., Korzhev M., Grebenjuk V.A., Wiens M., Schloßmacher U. & Wang X. (2013 c). The silicatein propeptide acts as inhibitor/modulator of self-organization during spicule axial filament formation. *FEBS Journal* 280, 1693-1708.

Müller W.E.G., Wang X., Jochum K.P. & Schröder H.C. (2013 d). Self-healing, an intrinsic property of biomineralization processes. *IUBMB life* 65, 382–396

Müller W.E.G., Wang X., Sinha B., Wiens M., Schröder H.C. & Jochum K.P. (2010). NanoSIMS: insights into the organization of the proteinaceous scaffold within hexactinellid sponge spicules. *ChemBioChem* 11, 1077-1082.

Müller, W.E.G., Schloßmacher U., Wang X., Boreiko A., Brandt D., Wolf S.E., Tremel W. & Schröder, H.C. (2008). Poly (silicate)-metabolizing silicatein in siliceous spicules and silicasomes of demosponges comprises dual enzymatic activities (silica polymerase and silica esterase). *FEBS Journal* 275, 362-370.

Murr M.M. & Morse D.E. (2005). Fractal intermediates in the self-assembly of silicatein filaments. *Proceedings of the National Academy of Sciences* 102, 11657-11662.

Murr M.M., Thakur G.S., Li Y., Tsuruta H., Mezic I. & Morse D.E. (2009). New pathway for self-assembly and emergent properties. *Nano Today* 4, 116-124.

Natalio F., Link T., Müller W.E.G., Schröder H.C., Cui F.Z., Wang X. & Wiens M. (2010 a). Bioengineering of the silica-polymerizing enzyme silicatein-α for a targeted application to hydroxyapatite. *Acta biomaterialia* 6, 3720-3728.

Natalio F., Mugnaioli E., Wiens M., Wang X., Schröder H.C., Tahir M.N., Tremel W., Kolb U. & Müller, W.E.G. (2010 b). Silicatein-mediated incorporation of titanium into spicules from the demosponge *Suberites domuncula*. *Cell and tissue research* 339, 429-436.

Pagliara S., Polini A., Camposeo A., Schröder H.C., Müller W.E.G. & Pisignano D. (2012). Electrical properties of in vitro biomineralized recombinant silicatein deposited by microfluidics. *Applied Physics Letters* 101, 193702-193702.

Patwardhan S.V., Holt S.A., Kelly S.M., Kreiner M., Perry C.C., & van der Walle C.F. (2010). Silica condensation by a silicatein α homologue involves surface-induced transition to a stable structural intermediate forming a saturated monolayer. *Biomacromolecules* 11, 3126-3135.

Perry, C.C. & Keeling-Tucker T. (2000). Biosilicification: the role of the organic matrix in structure control. *JBIC Journal of Biological Inorganic Chemistry* 5, 537-550.

Pietak A.M., Reid J.W., Stott M.J. & Sayer M. (2007). Silicon substitution in the calcium phosphate bioceramics. *Biomaterials* 28, 4023-4032.

Polini A., Pagliara S., Camposeo A., Biasco A., Schröder H.C., Müller W.E.G. & Pisignano D. (2011). Biosilica Electrically-Insulating Layers by Soft Lithography-Assisted Biomineralisation with Recombinant Silicatein. *Advanced Materials* 23, 4674-4678.

Purich, D. L. (2010). Enzyme kinetics: catalysis & control: a reference of theory and best-practice methods. *Elsevier Inc.*, p. 7.

Rai A. & Perry C.C. (2012). Mussel adhesive protein inspired coatings: a versatile method to fabricate silica films on various surfaces. *Journal of Materials Chemistry* 22, 4790-4796.

Rai A., & Perry C.C. (2010). Facile fabrication of uniform silica films with tunable physical properties using silicatein protein from sponges. *Langmuir* 26, 4152-4159.

Sapsford K.E., Algar W.R., Berti L., Gemmill K.B., Casey B.J., Oh E., Stewart M.H. & Medintz I.L. (2013). Functionalizing Nanoparticles with Biological Molecules: Developing Chemistries that Facilitate Nanotechnology. *Chemical reviews* 113, 1904-2074.

Schloßmacher U., Wiens M., Schröder H.C., Wang X., Jochum K.P. & Müller W.E.G. (2011). Silintaphin-1–interaction with silicatein during structure-guiding bio-silica formation. *FEBS Journal* 278, 1145-1155.

Schröder H.C., Brandt D., Schloßmacher U., Wang X., Tahir M.N., Tremel W., Belikov S.I. & Müller W.E.G. (2007 a). Enzymatic production of biosilica glass using enzymes from sponges: basic aspects and application in nanobiotechnology (material sciences and medicine). *Naturwissenschaften* 94, 339-359.

Schröder H.C., Natalio F., Shukoor I., Tremel W., Schloßmacher U., Wang X. & Müller W.E.G. (2007 b). Apposition of silica lamellae during growth of spicules in the demosponge *Suberites domuncula*: Biological/biochemical studies and chemical/biomimetical confirmation. *Journal of structural biology* 159, 325-334.

Schröder H.C., Wang X., Tremel W., Ushijima H. & Müller W.E.G. (2008). Biofabrication of biosilica-glass by living organisms. *Natural product reports* 25, 455-474.

Schröder H.C., Wiens M., Schloßmacher U., Brandt D. & Müller W.E.G (2012). Silicatein-mediated polycondensation of orthosilicic acid: modeling of a catalytic mechanism involving ring formation. *Silicon* 4, 33-38.

Shukoor M.I., Natalio F., Therese H.A., Tahir M.N., Ksenofontov V., Panthöfer M., Eberhard M., Theato P., Schröder H.C., Müller W.E.G. & Tremel W. (2008). Fabrication of a silica coating on magnetic γ-Fe2O3 nanoparticles by an immobilized enzyme. *Chemistry of Materials* 20, 3567-3573.

Sumerel J.L., Yang W., Kisailus D., Weaver J.C., Choi J.H. & Morse D.E. (2003). Biocatalytically templated synthesis of titanium dioxide. *Chemistry of materials* 15, 4804-4809.

Tahir M.N., Eberhardt M., Therese H.A., Kolb U., Theato P., Müller W.E.G., Schröder H.C. & Tremel W. (2006). From Single Molecules to Nanoscopically Structured Functional Materials: Au Nanocrystal Growth on TiO_2 Nanowires Controlled by Surface-Bound Silicatein. *Angewandte Chemie International Edition* 45, 4803-4809.

Tahir M.N., Natalio F., Therese H.A., Yella A., Metz N., Shah M.R., E. Mugnaioli, R. Berger, P. Theato, Schröder H.C., Müller W.E.G. & Tremel W. (2009). Enzyme-Mediated Deposition of a TiO_2 Coating onto Biofunctionalized WS2 Chalcogenide Nanotubes. *Advanced Functional Materials* 19, 285-291.

Tahir M.N., Théato P., Müller, W.E.G., Schröder H.C., Borejko A., Faiß S., Janshoff A., Huth J. & Tremel W. (2005). Formation of layered titania and zirconia catalysed by surface-bound silicatein. *Chemical communications* 44, 5533-5535.

Tahir M.N., Théato P., Müller W.E.G., Schröder H.C., Janshoff A., Zhang J., Huth J. & Tremel W. (2004). Monitoring the formation of biosilica catalysed by histidine-tagged silicatein. *Chemical communications* (024), 2848-2849.

Van der Linden E. & Venema P. (2007). Self-assembly and aggregation of proteins. *Current Opinion in Colloid & Interface Science* 12, 158-165.

Wang W. & Chau Y. (2009). Self-assembled peptide nanorods as building blocks of fractal patterns. *Soft Matter* 5, 4893-4898.

Wang X., Schloßmacher U., Wiens M., Batel R., Schröder H.C. & Müller W.E.G. (2012 a). Silicateins, silicatein interactors and cellular interplay in sponge skeletogenesis: formation of glass fiber-like spicules. *FEBS Journal* 279, 1721-1736.

Wang X., Schröder H.C., Brandt D., Wiens M., Lieberwirth I., Glasser G., U. Schloßmacher, Wang S. & Müller W.E.G. (2011). Sponge biosilica formation involves syneresis following polycondensation in vivo. *ChemBioChem* 12, 2316-2324.

Wang X., Schröder H.C., Wang K., Kaandorp J.A. & Müller W.E.G. (2012 b). Genetic, biological and structural hierarchies during sponge spicule formation: from soft sol–gels to solid 3D silica composite structures. *Soft Matter* 8, 9501-9518.

Wang X., Schröder H.C., Wiens M., Ushijima H. & Mueller W.E. (2012 c). Bio-silica and bio-polyphosphate: applications in biomedicine (bone formation). *Current Opinion in Biotechnology* 23, 570-578.

Whitesides G.M. & Grzybowski B. (2002). Self-assembly at all scales. *Science* 295, 2418-2421.

Wiens M., Bausen M., Natalio F., Link T., Schlossmacher U. & Müller W.E.G. (2009). The role of the silicatein-α interactor silintaphin-1 in biomimetic biomineralization. *Biomaterials* 30, 1648-1656.

Wiens M., Schröder H.C., Wang X., Link T., Steindorf D. & Müller W.E.G. (2011). Isolation of the silicatein-α interactor silintaphin-2 by a novel solid-phase pull-down assay. *Biochemistry* 50, 1981-1990.

Wiens M., Wang X., Natalio F., Schröder H.C., Schloßmacher U., Wang S., Korzhev M., Geurtsen W. & Müller W.E.G. (2010a). Bioinspired Fabrication of Bio-Silica-Based Bone-Substitution Materials. *Advanced Engineering Materials* 12, B438-B450.

Wiens M., Wang X., Schröder H.C., Kolb U., Schloßmacher U., Ushijima H. & Müller, W.E.G. (2010b). The role of biosilica in the osteoprotegerin/RANKL ratio in human osteoblast-like cells. *Biomaterials* 31, 7716-7725.

Witten T.T. & Sander L. M. (1983). Diffusion-limited aggregation. *Physical Review B* 27, 5686.

Wu C. & Chang J. (2013). A review of bioactive silicate ceramics. *Biomedical Materials* 8, 032001.

Xu A.W., Ma Y. & Cölfen H. (2007). Biomimetic mineralization. *Journal of Materials Chemistry* 17, 415-449.

Zhang H., Dunphy D.R., Jiang X., Meng H., Sun B., Tarn D., Xue M., Wang X., Lin S., Ji Z., Li R., Garcia F.L., Yang J., Kirk M.L., Xia T., Zink J.I., Nel A. & Brinker C.J. (2012). Processing Pathway Dependence of Amorphous Silica Nanoparticle Toxicity: Colloidal vs Pyrolytic. *Journal of the American Chemical Society* 134, 15790-15804.

Zhao C.X., Yu L. & Middelberg A.P. (2012). Design of low-charge peptide sequences for high-yield formation of titania nanoparticles. *Rsc Advances* 2, 1292-1295.

Zhao Q., Qian J., Gui Z., An Q. & Zhu M. (2010). Interfacial self-assembly of cellulose-based polyelectrolyte complexes: pattern formation of fractal "trees". *Soft Matter* 6, 1129-1137.

Zhou Y., Shimizu K., Cha J.N., Stucky G.D. & Morse D.E. (1999). Efficient catalysis of polysiloxane synthesis by silicatein α requires specific hydroxy and imidazole functionalities. *Angewandte Chemie International Edition* 38, 779-782.

Chapter 2

# Formation of micropatterned titania photocatalyst by microcontact printed silicatein on gold surfaces

2.1 Introduction

The soft lithographic method of microcontact printing (µCP) has been initially developed for patterning self-assembled monolayers (SAM) of alkanethiols onto gold substrates (Kumar & Whitesides, 1993). For this purpose, elastomeric stamps that carry the desired pattern in relief were first inked with the alkanethiol and, then, placed onto the target surface. During this direct contact, chemically stable metal-sulfur bonds were formed that facilitate the area-selective transfer of the molecular ink onto the substrate surface, according to the relief pattern of the stamps. Since then, the µCP technique has revealed an amazing versatility for patterned deposition of a variety of molecules, including silanes, DNA, lipids, and proteins (Akbulut et al., 2010; Wendeln & Ravoo 2012). Much effort has been devoted to the printing of enzymes, due to their inherent specificities concerning substrate and catalytic reactivity, both of which are explored for the design of biochemically active surfaces. Mainly three µCP based methodological approaches can be distinguished for enzyme patterning. In the first one, proteins are directly printed from stamp to substrate (Losic et al., 2002; Casero et al., 2010). Even though this direct approach is simple and fast, unspecific and weak binding through mere physisorption might affect both catalytic function (through conformational changes) as well as stability of the printed pattern (Chelmowski et al., 2007; Casero et al., 2010). In the second approach, enzymes are chemically modified to confer higher binding specificity to the substrate. Thus, enzymes were thiolated to facilitate chemisorption on bare gold (Wilhelm & Wittstock 2002; Casero et al., 2010). However, such protein derivatization is laborious and bears the risk of reduced enzymatic activity (through modification of catalytically active amino acid residues). Moreover, position and number of amine groups available for thiolation might affect proper protein conformation

and orientation during subsequent surface-immobilization of the enzyme. In the third approach, enzymes are immobilized on reactive SAM, using cross-linkers such as N-hydroxysuccinimide (NHS)/1-ethyl-3-(3-dimethylaminopropyl) carbodiimide (EDC) or glutaraldehyde (GA) (Losic et al., 2002; Wilhelm & Wittstock 2002). Similar to the abovementioned methods of protein derivatization this approach is laborious and, additionally, requires surface modification to obtain reactive SAM. Furthermore, possible side products of the cross-linking process must be removed and trace amounts often remain. Lastly, since often more than one amine group is accessible for coupling with a cross-linker, enzyme molecules will cross-link with each other, which might induce conformational distortion and reduce catalytic activity (Wilhelm & Wittstock, 2002; Luo et al., 2007). With the bioengineering of catalytically active recombinant silicatein, low energy catalytic pathways have become available for the synthesis of materials with tuned properties and novel property combinations (Müller et al., 2009; Natalio et al., 2010; Wiens et al., 2010 a; Wiens et al., 2010 b). Silicatein is the only known natural biomineralizing enzyme and has been originally isolated of siliceous sponges (Shimizu et al., 1998; Müller et al., 2008). Due to a certain elasticity and adaptability of the active site in its substrate scope, silicatein has the ability to catalyze and template the polycondensation of various substrates to metal(loid) oxides under near-physiological conditions, including silica, titania, gallium oxohydroxide, and barium titanate (Sumerel et al., 2009; Kisailus et al., 2005; Tahir et al., 2005; Tahir et al., 2006; Brutchey & Morse, 2008). Moreover, recombinant silicatein was immobilized via GA on Au surfaces functionalized with aminothiols (Rai & Perry, 2010). Upon exposure to its substrate tetramethyl orthosilicate, silicatein mediated synthesis of a uniform silica coating. Finally, in a first approach to print silicatein on bare Si surfaces, the recombinant enzyme was immobilized through µCP-mediated physisorption. Subsequent incubation with its substrate tetraethyl orthosilicate elicited corresponding silica patterns (Polini et al., 2011).

In this chapter, we attempted a straightforward one-step µCP approach for micropatterning of silicatein on Au surfaces without prior surface modification, while concurrently preserving the catalytic activity of the enzyme. Based on the activity of the

immobilized enzyme, we generated corresponding micropatterned and photocatalytically active TiO_2 thin films, using the silicatein alkoxide-like substrate titanium bis(ammonium lactato)dihydroxide (TiBALDH) (Scheme 6.1).
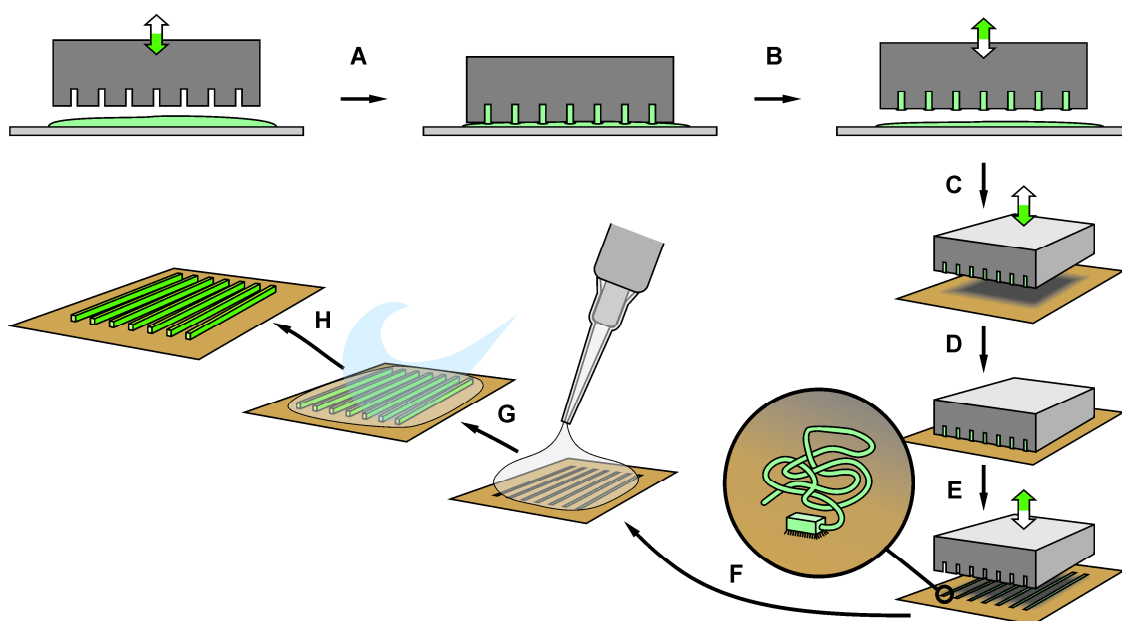
Scheme 2.1 μCP of silicatein onto Au surfaces and subsequent silicatein-mediated synthesis of titania micropatterns. (A, B) The PDMS replica is wetted with a solution of Cys-tagged silicatein (green). (C-E) The loaded replica is placed for 10 s in conformal contact with Au surface. (F) The enzyme is area-selectively anchored *via* the Cys-tag's thiol groups, according to the relief pattern of the replica (inset; the affinity tag is depicted as box). (G, H) The microcontact printed surface is covered by precursor solution (TiBALDH), resulting in the formation of titania, according to the printed pattern of silicatein

2.2 Experimental section

2.2.1 Preparation of recombinant Cys-tagged silicatein-α

The forward primer 5'-TGT TGC TGT TGC TGT TGC TGT TGC CCT GAA GCT GTA GAC TGG-3' (8x Cys residues) and the reverse primer 5'-TAG GGT GGG ATA AGA TGC ATC GGT-3' were used to amplify the open reading frame of *Suberites domuncula* mature silicatein-α ($aa_{115-330}$) from a cDNA template (NCBI accession number AJ272013) by polymerase chain reaction (PCR). PCR was carried out at an initial

denaturation for 5 min at 95°C, followed by 32 amplification cycles (95°C for 30 s, 56°C for 30 s, and 72°C for 60 s) and a final extension step at 72°C for 10 min. The resulting amplicons were T/A-ligated into the bacterial expression vector pTrcHis2-TOPO TA (Invitrogen, Karlsruhe, Germany), in frame with vector sequences encoding a C-terminal 6x His-tag (Scheme 6.2). Open reading frames were confirmed, using an automatic DNA sequenator (Li-Cor 4300). Following transformation of TOP10 Escherichia coli cells (Invitrogen) with these constructs, recombinant protein expression was induced with 1 mM isopropyl β-D-1-thiogalactopyranoside (IPTG) for 24 h. Subsequently, proteins were extracted and purified by nickel-nitrilotriacetic acid (Ni^{2+}-NTA) metal-affinity chromatography. (QIAexpress Kit; Qiagen, Hilden, Germany) according to (Wiens et al, 2010 c).

$$H_3N - \boxed{M\text{-}A\text{-}L\text{-}(C)_8\text{-}} \boxed{\text{mature silicatein}} - \boxed{(H)_6} - COOH$$

Scheme 2.2 Illustration of recombinant Cys-tagged silicatein-α used for microcontact printing. The amino acid residues of the C-terminal Cys-tag and the N-terminal His-tag (for Au-binding and nickel-nitrilotriacetic acid metal-affinity chromatography purification, respectively) are indicated. Drawn not to scale.

2.2.2 Cys-tagged silicatein-α identification by gel electrophoresis and immunoblotting

Protein expression was assessed through sodium dodecyl sulfate polyacrylamide gel electrophoresis (SDS-PAGE), using Novex protein marker as standard (Invitrogen). After blotting on polyvinylidene fluoride membranes (PVDF; Millipore, Billerica, MA), recombinant silicatein was immunodetected colorimetrically following consecutive incubations with anti-histidine primary antibodies (anti-His; 1:3,000 dilution, 1h; Invitrogen), alkaline phosphatase (AP)-conjugated species-specific secondary antibodies (1:10,000 dilution, 1h; Dianova, Hamburg, Germany), and 4-nitro blue tetrazolium chloride (NBT)/5-bromo-4-chloro-3-indolyl phosphate (BCIP) (Invitrogen).

Protein sizes were determined with the Precision protein marker (Bio-Rad, München, Germany).

2.2.3 Microcontact printing of silicatein-α on gold substrates

For µCP of patterned silicatein on Au, PDMS stamps (AMO GmbH, Aachen, Germany) were cleaned with 2-propanol and, then, inked with the recombinant and refolded protein by dipping into a solution of 5 µg silicatein in 250 µL TBS for 1 min at room temperature (RT). Subsequently, the stamps were dried by removing excess solution with a stream of air before they were placed in conformal contact with the bare gold substrate (Au(111)) for 10 s. Finally, the printed surface was extensively washed with TBS.

2.2.4 immunodetection of printed silicatein

The Au surfaces were incubated for 90 min (RT) with silicatein specific primary antibodies (diluted 1:1,000 in 15% blocking solution [Roche Applied Science, Mannheim, Germany]), (Wiens et al., 2009) followed by incubation with Cy3-labeled species specific secondary antibodies (90 min, RT) (Dianova). For visualization, the samples were inspected by confocal laser scanning microscopy (LSM; Carl Zeiss GmbH, Göttingen, Germany), using the 543 nm line of the helium/neon laser.

2.2.5 Synthesis and analysis of TiO$_2$ micropatterns

To obtain corresponding TiO$_2$ micropatterns, the printed gold surfaces were incubated in an aqueous solution of 250 µM titanium bis(ammonium lactato)-dihydroxide (TiBALDH; Sigma-Aldrich) for 2 h (RT). Afterwards, the surfaces were washed with water and ethanol to remove unreacted precursor and dried for 4 h at 60°C. The samples thus obtained were carefully washed, air-dried, and analyzed via scanning electron microscopy (LEO Gemini 1530; Zeiss, Oberkochen; Germany) as well as microRaman spectroscopy (532 nm excitation line; Bruker Senterra Optics; Ettlingen, Germany).

2.2.6 Photocatalytic activity of the micropatterned TiO$_2$ on gold substrates

The photocatalytic activity of the TiO$_2$ micropattern was tested spectrophotometrically via degradation of methylene blue (MB) as model reaction. Thus, the patterned gold surfaces were placed within quartz-glass vessels and, then, covered with an aqueous solution of MB (1 x 10^{-5} M). Subsequently, the photoreaction vessels were positioned in a closed cabinet and UV irradiated (366 nm) at a distance of 20 cm by a 50 W high-pressure mercury lamp. During irradiation, the solution was agitated for up to 1 h. At given time intervals, the absorption was measured at 660 nm with a SmartSpec spectrophotometer (Bio-Rad) and compared to that of the controls (i.e., as-prepared MB solution, Cys-tagged silicatein-printed gold surfaces without titania micropatterns, pristine gold substrate that had been pre-incubated with TiBALDH). Furthermore, photodegradation of MB was analyzed using a gold substrate with printed silicatein and micropatterned TiO$_2$ that had been calcined (500°C, 3h; Carbolite chamber furnace RHF 1500).

2.3 Results and discussion

Our approach is based on the bioengineering of silicatein to introduce an N-terminal sequence rich in cysteine residues (Cys-tag) that confers binding affinity to Au. Since the primary silicatein translation product undergoes post-translational modification *in vivo* (i.e., cleavage of a propeptide) and, furthermore, computational modeling of the silicatein 3D structure suggests that the propeptide blocks access to the catalytic site, (Schröder et al., 2007) mature silicatein was expressed in a recombinant way. For this purpose, the open reading frame of *Suberites domuncula* mature silicatein-α (aa$_{115-330}$) was amplified by polymerase chain reaction (PCR) from a cDNA template (NCBI accession number AJ272013), using a forward primer that encodes the N-terminal Cys-tag (NH$_2$-MALC8-COOH) (Scheme 6.2). Alternatively, a cDNA template without additional Cys-tag sequence was amplified to generate recombinant mature silicatein-α for control experiments (wild type silicatein; silicatein$_{WT}$) (Natalio et al., 2010). Following expression in a prokaryotic system as fusion with a 6x His-tag, the recombinant proteins were purified via nickel-nitrilotriacetic acid (Ni^{2+}-NTA) metal-affinity chromatography and

detected through sodium dodecyl sulfate polyacrylamide gel electrophoresis (SDS-PAGE) at the expected size (Fig. 2.1A). Furthermore, after blotting on polyvinylidene fluoride membranes (PVDF), recombinant silicatein was immunodetected colorimetrically following consecutive incubations with anti-histidine primary antibodies, alkaline phosphatase (AP)-conjugated species-specific secondary antibodies, and 4-nitro blue tetrazolium chloride/5-bromo-4-chloro-3-indolyl phosphate. The immunodetected protein bands confirmed the integrity of both recombinant silicatein varieties (Fig. 2.1B).
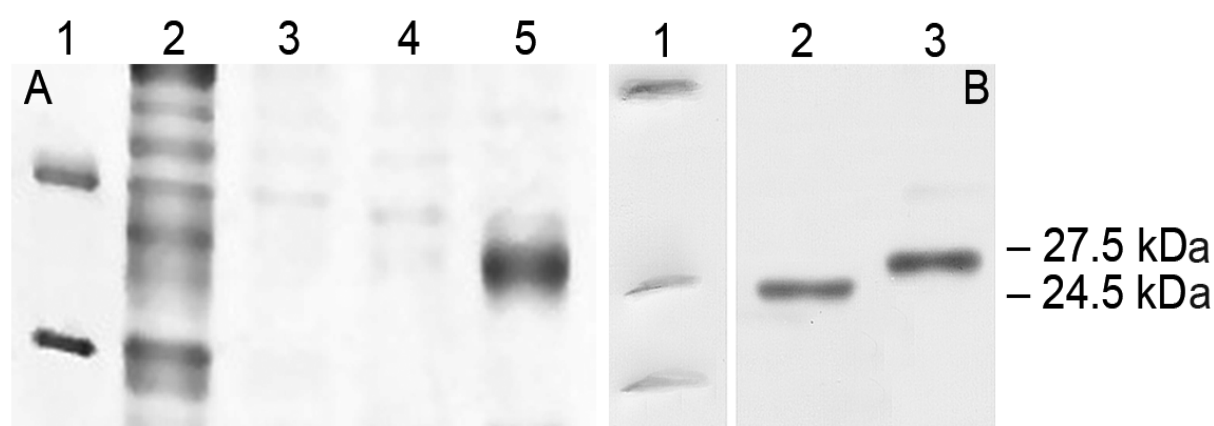

Fig. 2.1 Expression and purification of recombinant silicatein. After electrophoretic size-separation (SDS-PAGE) and transfer on Western blots, recombinant Cys-tagged silicatein (and silicatein$_{wt}$ for comparison) was detected colorimetrically via anti-histidine antibodies and AP-conjugated secondary antibodies at the expected size of ca. 27.5 kDa (24.5 kDa). (A) SDS-PAGE: 1) protein marker; 2) crude extract of IPTG-induced, silicatein-expressing *E. coli* strain; 3) flow-through during Ni^{2+}-NTA affinity chromatography purification; 4) wash fraction; 5) elution of recombinant Cys-tagged silicatein from Ni^{2+}-NTA matrix. (B) Western blot: 1) protein marker; 2) silicatein$_{wt}$; 3) Cys-tagged silicatein.

For µCP of patterned silicatein on Au, polydimethoxysilane (PDMS) stamps were inked with the recombinant and refolded protein (5 µg silicatein in 250 µL TBS for 1 min). Subsequently, the stamps were placed for 10 s in conformal contact with the bare gold substrate (Au(111)). After extensive washing, printed silicatein was immunodetected with a combination of specific primary antibodies, Cy3-labeled species-specific secondary antibodies, and confocal laser scanning microscopy (LSM), using the 543 nm line of the helium/neon laser. Fig. 2.2A shows not only that the relief pattern of the

stamp was transferred onto the substrate with high fidelity but also that the printed pattern had remained stable during the following stringent washing. As control, recombinant silicatein$_{WT}$ had been printed similarly in a parallel approach. The resulting weak fluorescence signals upon immunodetection clearly demonstrate that the binding of this non-Cys-tagged protein was only weak and unspecific (Fig. 2.2B).
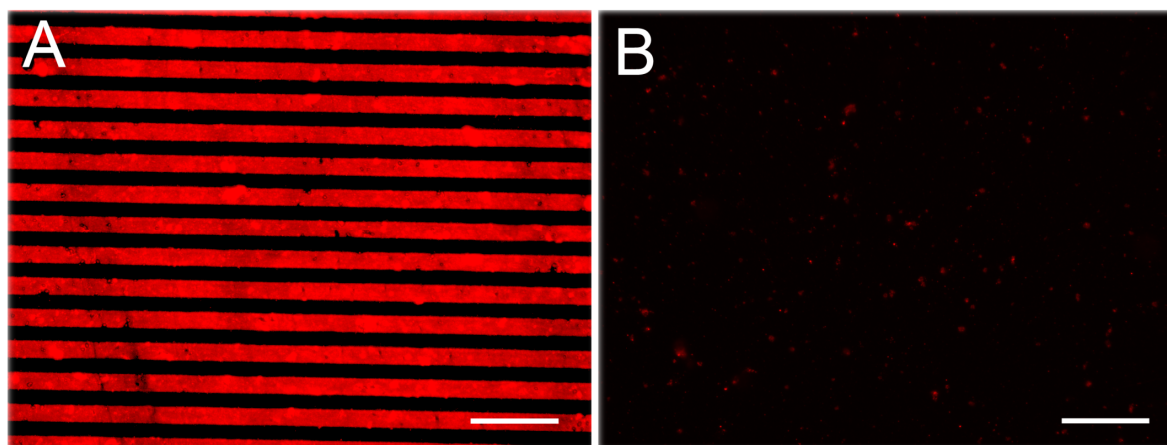

Fig. 2.2 Fluorescence micrographs of silicatein printed onto Au surfaces. Silicatein was immunodetected with a combination of specific primary antibodies, Cy3-labeled secondary antibodies, and subsequent LSM. (A) Cys-tagged silicatein. (B) Silicatein$_{wt}$. Bars, 40 µm.

To obtain TiO$_2$ micropatterns, the silicatein-printed Au surfaces were incubated in an aqueous solution of 250 µM TiBALDH (2 h, room temperature). Following extensive washing to remove unreacted precursor, the presence of silicatein-synthesized micropatterned TiO$_2$ was confirmed by scanning electron microscopy (SEM) and microRaman spectroscopy (µRS). The SEM micrograph revealed the formation of micropatterns according to the printed pattern of silicatein (Fig. 2.3A; printed line width of ca. 7 µm, separated by non-printed gaps of 6 µm). In a comparable approach, silicatein immobilized on polymeric SAM catalyzed the formation of coatings of TiO$_2$ nanoparticles with diameters of 50–60 nm (Tahir et al., 2005). Complementary (µRS) showed the four characteristic peaks at 152, 396, 524, and 634 cm^{-1} that are usually associated with the anatase phase and differ from the broad background common for amorphous titania (Fig. 2.3B) (Busca et al., 1994). Additional broadening of the peaks,

however, indicates mixed amorphous and anatase phases (Kharlampieva et al., 2008; Wang et al., 2008).
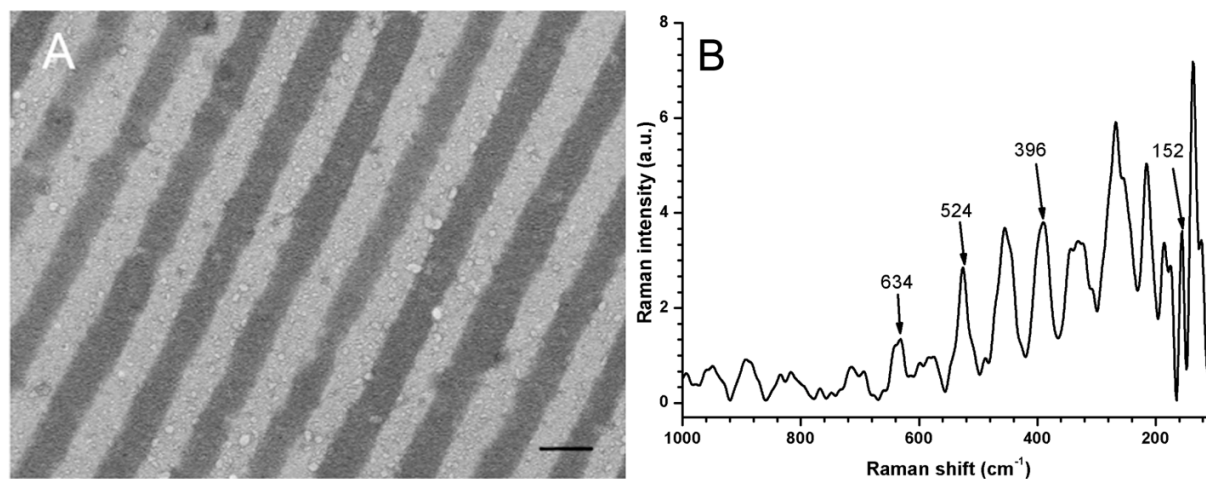

Fig. 2.3 Silicatein-microcontact printed Au substrate with micropatterned TiO_2. (A) Scanning electron micrograph. Bar, 10 µm. (B) Normalized Raman spectrum of silicatein-microcontact printed and micropatterned Au substrate. Arrows indicate the peaks characteristic for TiO_2.

The photocatalytic activity of the silicatein-synthesized TiO_2 micropattern was tested via degradation of methylene blue (MB) as model reaction: during photocatalysis, the dye undergoes decomposition that in turn causes a change in color, which can be quantified spectrophotometrically (Chen et al., 2007). Accordingly, the absorption (at 660 nm) was measured of aqueous MB solutions that covered the samples for the indicated time of UV irradiation. During the experiment, the color of the solution decreased gradually from an initial blue to nearly transparent in the presence of the titania catalyst, clearly showing the decomposition of MB as a function of irradiation time. Thus, the first-order degradation rate constant K of MB degradation was calculated according to $-[\ln(C/C_0] = Kt$, where C/C_0 is the normalized concentration of the MB solution and proportional to the normalized absorbance (Chang et al., 2004). Fig. 2.4 shows that the degradation rate constant is 0.97 % min^{-1} for the MB solution, 1.15 % min^{-1} for the Cys-tagged silicatein-printed Au surface (possibly caused by mechanisms that involve functional groups arranged at the outer surface of the enzyme and not the active site) (Tahir et al., 2006). 1.50 % min^{-1} for the pristine Au surface that had been pre-incubated with the titania precursor, and 2.11 % min^{-1} for the Au surface micropatterned with Cys-tagged

silicatein and titania. In a previous approach, where TiO_2 thin films with anatase phase on pretreated F-doping SnO_2 surfaces were obtained non-catalytically through µCP of a titania precursor and subsequent thermal oxidation, a photodegradation rate of MB of 0.96 - 1.747 % min^{-1} was observed (Chen et al., 2007).
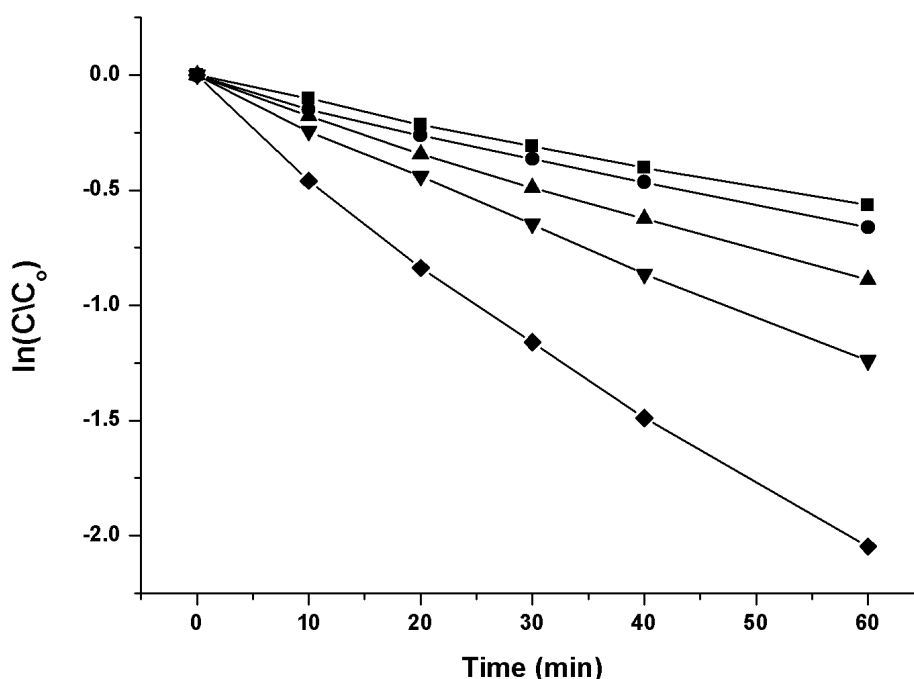

Fig. 2.4 Time-resolved photocatalytic degradation of MB upon UV irradiation. (■) MB solution. (●) Au surface printed with Cys-tagged silicatein. (▲) Au surface pre-incubated with TiBALDH. (▼) Au surface patterned with Cys-tagged silicatein and titania catalyst. (♦) Au surface patterned with Cys-tagged silicatein and titania catalyst, calcined at 500°C. C/C_0 is the normalized concentration of the MB solution.

Catalyst morphology and crystal composition have been shown to greatly influence the catalytic performance. Hence, anatase is more photocatalytically active than the rutile phase, whereas amorphous TiO_2 has negligible activity (Ohtani et al., 1997). However, TiO_2 produced by silicatein-mediated catalysis is composed of both anatase and amorphous TiO_2 (Sumerel et al., 2003, Tahir et al., 2005). Therefore, to enhance the catalytic performance of silicatein-synthesized micropatterned TiO_2 (i.e., the photodegradation of MB), phase transformation from amorphous to anatase phase was thermally induced (3 h, 500°C). Subsequent photocatalytic experiments revealed a

considerably increased degradation of MB, as compared to the uncalcined samples, with a rate constant of MB photodegradation of 3.61 % min^{-1}.

In conclusion, μCP of Cys-tagged silicatein provides access to the enzymatically controlled synthesis of micropatterned surfaces via a simple and fast route under mild conditions. The inherent photocatalytic and semiconducting properties of the resulting TiO_2 micropatterns might be explored for fabricating surface-tailored microdevices with potential application in microelectronics, photovoltaics, or as biomedical implants (Gao et al., 2004; Sahlin et al., 2006).

2.4 References

Akbulut O., Yu A.A. & Stellacci F. (2010). Fabrication of biomolecular devices via supramolecular contact-based approaches. *Chemical Society Reviews* 39, 30-37.

Brutchey R.L. & Morse D.E. (2008). Silicatein and the translation of its molecular mechanism of biosilicification into low temperature nanomaterial synthesis. *Chemical reviews* 108, 4915-4934.

Busca G., Ramis G., Amores J.M.G., Escribano V.S. & Piaggio P. (1994). FT Raman and FTIR studies of titanias and metatitanate powders. *Journal of the Chemical Society, Faraday Transactions* 90, 3181-3190.

Casero E., Petit-Domínguez M.D., Parra-Alfambra A.M., Gismera M.J., Pariente F., Lorenzo E. & Vázquez L. (2010). One-step covalent microcontact printing approach to produce patterns of lactate oxidase. *Physical Chemistry Chemical Physics* 12, 2830-2837.

Chang H., Su C., Lo C.H., Chen L.C., Tsung T.T., & Jwo C.S. (2004). Photodecomposition and surface adsorption of methylene blue on TiO_2 nanofluid prepared by ASNSS. *Materials transactions* 45, 3334-3337.

Chelmowski R., Prekelt A., Grunwald C. & Wöll C. (2007). A case study on biological activity in a surface-bound multicomponent system: The biotin-streptavidin-peroxidase system. *The Journal of Physical Chemistry A* 111, 12295-12303.

Chen D., Gao Y., Wang G., Zhang H., Lu W., & Li J. (2007). Surface tailoring for controlled photoelectrochemical properties: effect of patterned TiO_2 microarrays. *The Journal of Physical Chemistry C* 111, 13163-13169.

Gao Y., Masuda Y., & Koumoto K. (2004). Light-excited superhydrophilicity of amorphous TiO_2 thin films deposited in an aqueous peroxotitanate solution. *Langmuir* 20, 3188-3194.

Kharlampieva E., Tsukruk T., Slocik J.M., Ko H., Poulsen N., Naik R.R., Kröger N. & Tsukruk V.V. (2008). Bioenabled Surface-Mediated Growth of Titania Nanoparticles. *Advanced Materials* 20, 3274-3279.

Kisailus D., Choi J.H., Weaver J.C., Yang W. & Morse D.E. (2005). Enzymatic synthesis and nanostructural control of gallium oxide at low temperature. *Advanced Materials* 17, 314-318.

Kumar A. & Whitesides G. M. (1993). Features of gold having micrometer to centimeter dimensions can be formed through a combination of stamping with an elastomeric stamp and an alkanethiol ''ink'' followed by chemical etching. *Applied Physics Letters* 63, 2002-2004.

Losic D., Shapter J.G. & Gooding J.J. (2002). Scanning tunneling microscopy studies of glucose oxidase on gold surfaces. *Langmuir* 18, 5422-5428.

Luo H.Q., Shiku H., Kumagai A., Takahashi Y., Yasukawa T. & Matsue T. (2007). Microcontact printed diaphorase monolayer on glass characterized by atomic force microscopy and scanning electrochemical microscopy. *Electrochemistry Communications* 9, 2703-2708.

Müller W.E.G., Wang X., Cui F. Z., Jochum K. P., Tremel W., Bill J., Schröder H.C., Natalio F., Schloßmacher U. & Wiens M. (2009). Sponge spicules as blueprints for the biofabrication of inorganic–organic composites and biomaterials. *Applied microbiology and biotechnology* 83, 397-413.

Müller W.E.G., Wang X., Kropf K., Boreiko A., Schloßmacher U., Brandt D., Schröder H.C. & Wiens M. (2008). Silicatein expression in the hexactinellid Crateromorpha meyeri: the lead marker gene restricted to siliceous sponges. *Cell and tissue research* 333, 339-351.

Natalio F., Link T., Müller W.E.G., Schröder H.C., Cui F.Z., Wang X. & Wiens M. (2010). Bioengineering of the silica-polymerizing enzyme silicatein-α for a targeted application to hydroxyapatite. *Acta biomaterialia* 6, 3720-3728.

Ohtani B., Ogawa Y., & Nishimoto S.I. (1997). Photocatalytic activity of amorphous-anatase mixture of titanium (IV) oxide particles suspended in aqueous solutions. *The Journal of Physical Chemistry B* 101, 3746-3752.

Polini A., Pagliara S., Camposeo A., Biasco A., Schröder H.C., Müller W.E.G. & Pisignano D. (2011). Biosilica Electrically-Insulating Layers by Soft Lithography-Assisted Biomineralisation with Recombinant Silicatein. *Advanced Materials* 23, 4674-4678.

Rai A., & Perry C.C. (2009). Facile fabrication of uniform silica films with tunable physical properties using silicatein protein from sponges. *Langmuir* 26, 4152-4159.

Sahlin H., Contreras R., Gaskill D.F., Bjursten L.M., & Frangos J.A. (2006). Anti-inflammatory properties of micropatterned titanium coatings. *Journal of Biomedical Materials Research Part A* 77, 43-49.

Schröder H.C., Brandt D., Schloßmacher U., Wang X., Tahir M.N., Tremel W., Belikov S.I. & Müller W.E.G. (2007). Enzymatic production of biosilica glass using enzymes from sponges: basic aspects and application in nanobiotechnology (material sciences and medicine). *Naturwissenschaften* 94, 339-359.

Shimizu K., Cha J., Stucky G.D. & Morse D.E. (1998). Silicatein α: cathepsin L-like protein in sponge biosilica. *Proceedings of the National Academy of Sciences* 95, 6234-6238.

Sumerel J.L., Yang W., Kisailus D., Weaver J.C., Choi J.H. & Morse D.E. (2003). Biocatalytically templated synthesis of titanium dioxide. *Chemistry of materials* 15, 4804-4809.

Tahir M.N., Eberhardt M., Theato P., Faiß S., Janshoff A., Gorelik T., Janshoff A., Gorelik T., Kolb U. & Tremel W. (2006). Reactive polymers: a versatile toolbox for the immobilization of functional molecules on TiO_2 nanoparticles. *Angewandte Chemie International Edition* 45, 908-912.

Tahir M.N., Théato P., Müller, W.E.G., Schröder H.C., Borejko A., Faiß S., Janshoff A., Huth J. & Tremel W. (2005). Formation of layered titania and zirconia catalysed by surface-bound silicatein. *Chemical communications* 44, 5533-5535.

Wang J., & Lin Z. (2008). Freestanding TiO_2 nanotube arrays with ultrahigh aspect ratio via electrochemical anodization. *Chemistry of Materials* 20, 1257-1261.

Wendeln C. & Ravoo B. J. (2012). Surface patterning by microcontact chemistry. *Langmuir* 28, 5527-5538.

Wiens M., Bausen M., Natalio F., Link T., Schlossmacher U. & Müller W.E.G. (2009). The role of the silicatein-α interactor silintaphin-1 in biomimetic biomineralization. *Biomaterials* 30, 1648-1656.

Wiens M., Wang X., Natalio F., Schröder H.C., Schloßmacher U., Wang S., Korzhev M., Geurtsen W. & Müller, W.E.G. (2010a). Bioinspired Fabrication of Bio-Silica-Based Bone-Substitution Materials. *Advanced Engineering Materials* 12, B438-B450.

Wiens M., Wang X., Schröder H.C., Kolb U., Schloßmacher U., Ushijima H. & Müller, W.E.G. (2010b). The role of biosilica in the osteoprotegerin/RANKL ratio in human osteoblast-like cells. *Biomaterials* 31, 7716-7725.

Wiens M., Wang X., Unger A., Schröder H.C., Grebenjuk V.A., Pisignano D., Jochum K.P. & Müller W.E.G. (2010c). Flashing light signaling circuit in sponges: Endogenous light generation after tissue ablation in Suberites domuncula. *Journal of cellular biochemistry* 111, 1377-1389.

Wilhelm T. & Wittstock G. (2002). Generation of periodic enzyme patterns by soft lithography and activity imaging by scanning electrochemical microscopy. *Langmuir* 18, 9485-9493.

Chapter 3

Bioinspired self-assembly of tyrosinase-modified silicatein and fluorescent core-shell silica spheres

3.1 Introduction

Conventional methodologies mostly bar the fabrication of multifunctional silica-based materials that have an extended range of properties. Consequently, there is considerable interest in synthetic approaches that translate the fundamental mechanisms of poriferan and diatom biosilicification to the biomimetic synthesis of such advanced materials at ambient conditions. In Porifera (sponges), silica formation is initiated by the intracellular self-assembly of axial filaments that predominantly consist of the enzyme silicatein. Silicatein catalyzes the polymerization of amorphous silica nanospheres from monomeric precursors and, subsequently, templates their deposition via ionic and hydrogen bonding (Brutchey & Morse, 2008; Schröder et al., 2012). The resulting siliceous skeletal elements (spicules) have remarkable optical and mechanical properties (Aizenberg et al., 2004). Whereas, the fabrication of artificial siliceous sponge spicules has not been accomplished so far, frustule-like siliceous microstructures were obtained by using multiphoton lithography: In an elaborate procedure, protein hydrogel scaffolds were first prepared to template the deposition of silica nanoparticles under acidic conditions and, then, removed by calcinations (Khripin et al., 2011). Silicatein monomers self-assemble to filaments via oligomers and fractally patterned aggregates (Murr & Morse 2005; Müller et al., 2007). This spontaneous organization is mainly mediated by hydrophobic interactions. Secondary weaker interactions likely contribute to the subsequent condensation and organization of fractals to filamentous structures. Furthermore, this process is assisted by the scaffold protein silintaphin-1, which co-localizes in axial filaments (Wiens et al., 2009). The resulting filament acts as templates for silica nanospheres deposition. In previous biomimetic attempts to reconstruct the filament formation in vitro self-assembly of silicatein-α did not advance beyond the stage

of fractals (Schloßmacher et al., 2011). However, combined with inherent molecular recognition properties present at the silicatein surface, this self-assembly has a considerable potential for the controlled synthesis and pattern formation of inorganic-organic composites at the molecular level. Indeed, silicatein-α has been shown to guide the deposition of SiO_2 or TiO_2 nanoparticles to spicule-like structures (Schloßmacher et al., 2011; Müller et al., 2009; Tahir et al., 2005). However, the true challenge is to translate these processes from the nano- to the mesoscale. *In vivo*, the assembly to such structures is under cellular control and occurs in specialized compartments. In contrast, *in vitro,* the application of recombinant silicatein-α allows the formation of only microscale assemblies. This difference in dimension is likely caused by biochemical or physical factors that are unknown so far. Hence, since *in vitro,* the number of molecular tools available is limited, bioinspired strategies are called for. Thus, His-tagged recombinant silicatein had been tethered via Ni-NTA to an acrylate-based backbone as template for the deposition of silica to nanofibers (Tahir et al., 2009). In a different approach, Au was surface-functionalized with a DOPA (3, 4-dihydroxyphenylalanine)-bearing peptide, whose reactivity towards amine and thiol groups was used to covalently bind silicatein onto Au as surface coating (Rai & Perry 2012). Lastly, recombinant silicatein was transferred onto Si surfaces through a combination of soft-lithography (using an elastomeric mold) and pressure-driven microfluidics, which yielded siliceous microstructures (Polini et al., 2012).

In this chapter, we describe two proof-of-concept approaches for the straightforward preparation of self-assembled mesoscale fibers, consisting of silicatein and fluorescent core-shell silica spheres. These mesofibers were prepared under mild conditions *via* a simple and fast route that does not require laborious chemical protein cross-linking and protein immobilization. Both approaches have been inspired by the intermolecular cross-linking of mussel foot proteins (Mfps) and their adhesive properties: Mfps carry DOPA/DOPAquinone through post-translational modification of tyrosine residues. Tyrosinase catalyzes both the oxidation of monophenol (e.g., tyrosine) to o-diphenol (DOPA) and the oxidation of o-diphenol to o-quinone (DOPAquinone). DOPA facilitates adhesion to a variety of substrates (SiO_2, TiO_2, hydroxyapatite, etc.) via hydrogen- or

coordination bonding (Lee et al., 2006; Lee et al., 2007; Wei et al., 2013; Heck et al., 2013). On the other hand, the very reactive DOPAquinone can undergo non-enzymatic reactions with various nucleophiles leading to the formation of cross-linked proteins. In contrast to the non-specific chemical cross-linking of proteins, the limited availability of tyrosine side chains on the surface of silicatein as substrates for tyrosinase (Heck et al., 2013) (see scheme 3.1) prevents unwanted protein gelation but accelerates protein aggregation as compared to the oligomerization of silicatein monomers (Murr & Morse 2005).
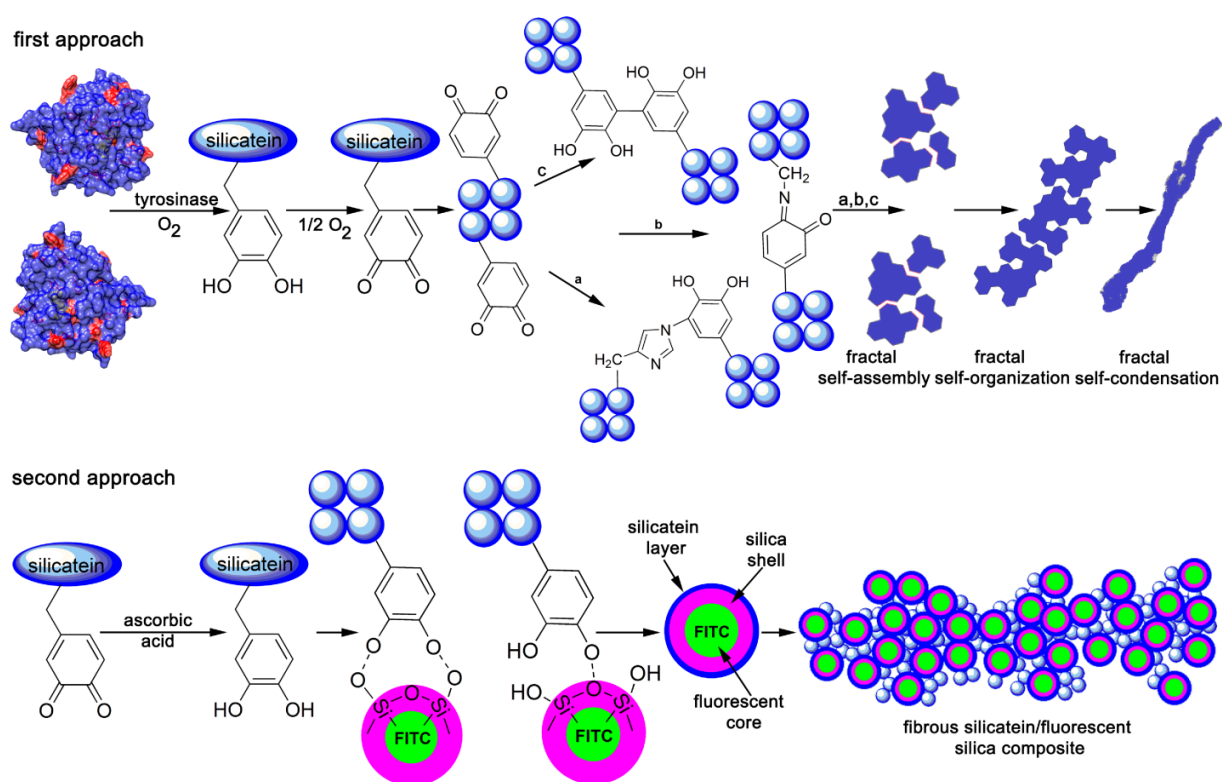
Scheme 3.1 Proposed cross-linking and immobilization mechanisms, (1st approach) the assembly of tyrosinase-modified silicatein to filamentous templates for the deposition of fluorescent core-shell silica particles and (2nd approach) the assembly of tyrosinase-modified silicatein and silicatein-coated fluorescent core-shell silica particles to mesofibers. For further details in the proposed mechanisms of cross-linking and immobilization see text.

3.2 Experimental section

3.2.1 Chemicals

All chemicals were purchased from Sigma-Aldrich (Taufkirchen, Germany) unless stated otherwise. Tetraethyl orthosilicate (TEOS, 131903), fluorescein isothiocyanate isomer I (FITC, F4274), (3-aminopropyl)triethoxysilane (APTS, 440140), ammonium hydroxide solution (AHS, 221228), L-glutathione reduced (GSH, G4251), glutathione oxidized (GSSG, 150568), mushroom tyrosinase (T3824), and L-arginine (3144.2, Carl Roth GmbH; Karlsruhe, Germany).

3.2.2 Recombinant silicatein-α expression and folding

Mature *S. domuncula* silicatein-α was expressed in E. coli and purified via Ni^{2+}-NTA affinity chromatography as described previously (Müller et al., 2013). Then, 0.8 mg/ml of denatured protein (eluted in 6 M urea, 50 mM KH_2PO_4 [pH 8.0], 250 mM imidazole, 300 mM KCl) were diluted 3-fold in refolding buffer (50 mM Tris-HCl [pH 8.5], 0.5 M L-arginine, 9 mM GSH, 1 mM GSSG, 0.3 M NaCl, 1 mM KCl). The refolding buffer was delivered over one hour with a flow rate of 0.2 ml/min at 4 °C. To restore the initial volume, the sample was concentrated with an Amicon Ultra centrifugal filter with a 10 kDa cut-off (Merck Millipore; Darmstadt, Germany). The whole procedure was repeated four more times to dilute the urea concentration to about 70 mM. Subsequently, the protein was dialyzed against 50 mM Tris-HCl (pH 7.5, overnight). No aggregation was observed after dialysis. Finally, silicatein was concentrated and then lyophilized at −75°C for 24 h.

Secondary structures were assessed by Micro-Raman spectroscopy (532 nm excitation line; Bruker Senterra Optics; Ettlingen, Germany). For this purpose, 20 mg lyophilized silicatein-α were placed on CaF_2 disks (Korth Kristalle GmbH; Kiel, Germany) and analyzed. Additionally, 20 mg lyophilized silicatein-α were dissolved in 1 ml Tris-HCl (50 mM, pH 7.4). Immediately after solubilization, soluble silicatein monomers were analyzed by passing the laser beam through the focusing system. Subsequently, after 1 hour of incubation, the observable silicatein assemblies were also analyzed. At least

three spectra were collected for all samples with a resolution of 9 cm^{-1} in the range of 75 - 4,100 cm^{-1}. The number and location of bands of the secondary structure components resolved by Fourier self-deconvolution (FSD) were verified by the peak fit I residue method using PeakFit (version 4.12, Seasolve Software; San Jose, CA) for the original amide I spectra. The peaks were assumed to be Gaussian/Lorentzian with a linear baseline. The height and width of each peak was manually adjusted to provide a reasonable starting point for the curve fitting program. The coefficient of determination (r^2) was > 0.999 for all spectra.

3.2.3 Preparation of fluorescent core-shell silica spheres

Colloidal fluorescent core-shell silica spheres were prepared in a modified Stöber synthesis (Blaaderen & Vrij 1992). For this purpose, FITC was covalently conjugated to the amine group of APTS via its isothiocyanate group and condensed to form a dye-rich core. Subsequently, TEOS was added to form a dense silica network around the fluorescent core, providing shielding from solvent interactions. In short, 53 mM of APTS were reacted with 30 mM FITC in anhydrous ethanol for 12 h with gentle shaking. Subsequently, the conjugated dye was condensed with 16 mM TEOS in ethanol/AHS (10:1) to form the silica-dye core. The reaction was allowed to continue for 24 hours with slow stirring. Following two washing steps in ethanol/AHS (10:1), the spheres were diluted 20-fold in ethanol/AHS and incubated with 103 mM TEOS to obtain the silica shell. Ultimately, particles were inspected by fluorescence microscopy (AMG EVOSfl).

3.2.4. Preparation of self-assembled silicatein/fluorescent silica core-shell mesofibers

To enhance the self-assembly of recombinant silicatein-α and fluorescent silica core-shell spheres to mesoscale filaments two alternative approaches were explored. Both approaches were based on the tyrosinase-mediated conversion of tyrosine residues of silicatein to DOPA/DOPAquinone residues. In pilot experiments, a range of silicatein/tyrosinase weight ratios had been assessed, from 200:1 to 10:1, with 50:1 being most effective for fiber formation and subsequent visualization of the fibrous composites. Consequently, in the first approach, 2.5 mg lyophilized silicatein were dissolved in 1 ml 0.1 M phosphate-buffered saline (PBS; pH 6.5, according to the

manufacturer's specification of tyrosinase) and filtered through a low protein binding membrane filter (0.22 µm). Then, 50 µg/ml mushroom tyrosinase were added. The reaction was incubated overnight with moderate shaking (already after 30 min of incubation small cross-linked aggregates were observed, turning the solution turbid). Subsequently, 50 µg/ml of fluorescent core-shell silica particles were added to 1.6 µg filaments for 2 h at room temperature with slow shaking. After washing three times with aqua dest., the decoration of the filaments with the fluorescent particles was monitored by using an EVOS fluorescence microscope.

In the second approach, again 2.5 mg lyophilized silicatein were dissolved in 1 ml of 0.1 M PBS (pH 6.5). By adding 50 µg/ml fluorescent silica core-shell particles, silicatein oligomers and fractals were surface-immobilized due to the templating activity of silicatein (Müller et al., 2008; Tahir et al., 2009; Wiens et al., 2013). After 2 h of incubation with slow, tilted stirring, 50 µg/ml tyrosinase and 25 mM ascorbic acid were added for up to 18 h. The samples were analyzed by Fourier transform infrared spectroscopy with attenuated total reflection (FTIR-ATR; Varian 660 spectrometer with Golden Gate ATR accessory). For this purpose, the silicatein/silica self-assemblies were washed extensively with deionized water and, then, lyophilized for 2 days. Spectra were collected by averaging 64 scans with a resolution of 4 cm^{-1}. Finally, the samples were characterized by 3D laser scanning microscopy (Keyence VK-9700) and, following gold-sputtering, by field-emission environmental scanning electron microscopy coupled to energy-dispersive X-ray spectroscopy (Philips XL30), with an accelerating voltage of 20 kV.

3.3 Results and discussion

For both approaches represented in this chapter, high concentrations of folded recombinant silicatein were required. However, when expressed in *E. coli* silicatein-α mainly accumulates in inclusion bodies that have to be solubilized by using denaturants. Then, to induce correct folding, the protein solution is generally dialyzed against large volumes of refolding buffer, containing L-arginine and the glutathione oxido shuffling system (Natalio et al., 2010). To avoid aggregation during this prolonged exposure to

gradually decreasing concentrations of the denaturant, initial low protein concentrations must be employed. Thus, ultimately only a low yield of folded silicatein can be obtained. Accordingly, to obtain the high protein concentration required for the fabrication of mesoscale structures, a reverse dilution method for silicatein folding has been established, yielding so far unmatched concentrations of up to 20 mg/ml folded protein. Protein folding was assessed by Micro-Raman spectroscopy (MRS), focusing on the amide I band, which is most sensitive to conformational changes of the protein and has the highest intensity of all amide bands. Fig. 3.1 shows the distribution of secondary structures obtained by Fourier self-deconvolution (FSD) and curve fitting. Thus, lyophilized silicatein (Fig. 3.1A) revealed a predominance of well-resolved β-sheet structural elements, in particular at 1630, 1668, and 1677 cm^{-1} (overall ca. 48 %), whereas α-helical structures at 1650 cm^{-1} were less present (12 %). Upon dissolution of silicatein, this value increased to 26 % (Fig. 3.1B). This significant solubilization-induced structural rearrangement correlated with the disappearance of a band at 1658 cm^{-1} of the solid silicatein spectrum. This band might have originated from both helical and sheet residues of the dehydrated protein. Such a reversible transformation of β-sheets to α-helical structures after solubilization has been previously described for various proteins (Griebenow & Klibanov, 1995). After one hour in aqueous solution the spectrum revealed a drop in the α-helix content (e.g., at 1652 cm^{-1}, 12 %) and an increased content of β-sheets structures (e.g., at 1662 cm^{-1}, 23 %) (Fig. 3.1C). This increase of β-sheet structures and the corresponding decrease in α-helical confirmations has been previously correlated with the occurrence of ordered aggregates during protofilament formation of proteins (Apetri et al., 2006). Concurrently, the prevalence of β-sheet conformations has been observed in native silicatein of axial filaments (Croce et al., 2004; Patwardhan et al., 2010). This was also corroborated by the bands at 1620 and 1635 cm^{-1} that can be assigned to extended β-sheet structures as well as the appearance of a band at 1696 cm^{-1} that suggests the formation of intermolecular β-sheets due to the assembly of silicatein to filaments (Pallarès et al., 2004).
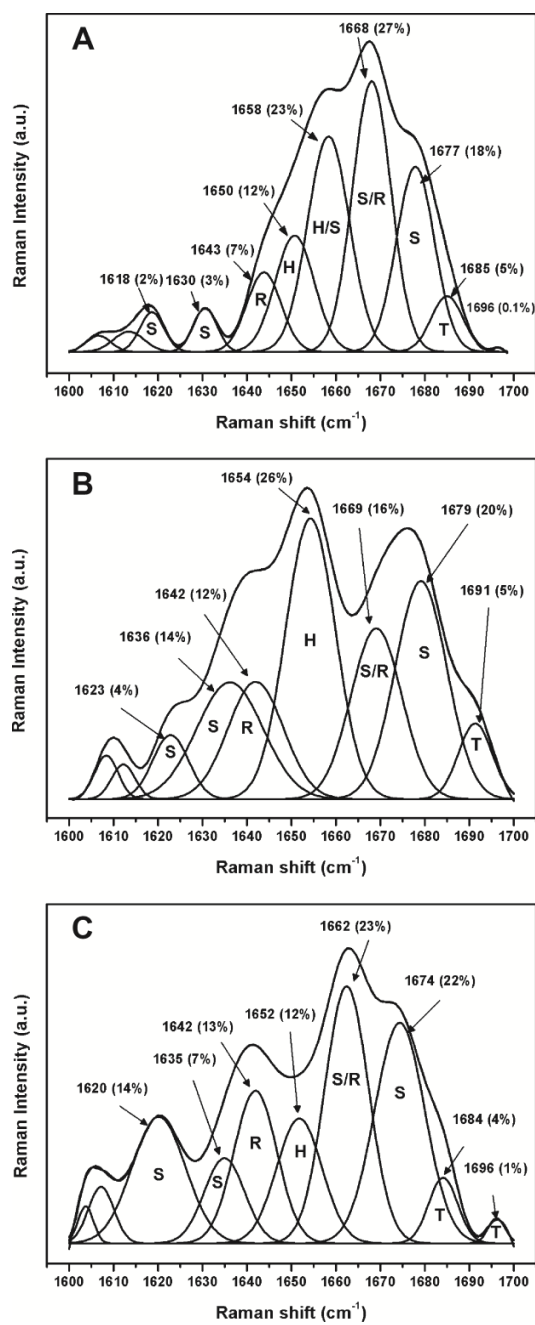
Fig. 3.1 Raman spectrum and curve fitting analysis of lyophilized recombinant silicatein (A), dissolved recombinant silicatein at zero time (B), and after 30 min (C). The area of the individual bands has been used to calculate the secondary structure content (H, helix; S, sheet; T, turn; R, random coil).

Self-assembly of recombinant silicatein *in vitro* is suspended at the fractal stage based on a previous investigation (Müller et al., 2013). To facilitate the biomimetic condensation and organization of these nanosized fractal building blocks to filamentous structures, a high concentration of silicatein (i.e., 2.5 mg lyophilized protein dissolved in 1 ml phosphate-buffered saline [PBS]) was treated with tyrosinase for up to 18 h. During this time and at slightly acidic pH (6.5), solvent-accessible tyrosine residues (Murr & Morse, 2005) were enzymatically modified to reactive DOPAquinone residues, which mediate non-enzymatic intermolecular cross-linking (including C–C, C–N, and C=N bonds) (Chen et al., 2001; Haemers et al., 2003). The accessibility on the silicatein surface of tyrosine residues (in red; Scheme 3.1) to the solvent was verified by using homology modelling, based on the cathepsin l crystal structure (Murr & Morse, 2005). Tyrosinase acts with high specificity on the surface tyrosyl side chains of silicatein monomers and oligomers to generate 3, 4-dihydroxyphenylalanine (DOPA) that, then, undergoes spontaneous oxidation in the presence of oxygen to reactive DOPAquinone. A slightly acidic environment (pH 6.5) was used in this study to slow down the oxidation rate of DOPA to DOPAquinone residues in order to enhance the degree of cross-linking, as has been proposed before (Haemers et al., 2003). In an acidic environment, aryl-alkylamine addition (Michael-type addition) reactions are unlikely to occur due to the high pKa value of lysine residues. However, the C-terminal histidine tag of the recombinant silicatein might contribute to direct coupling to DOPAquinone residues (scheme 3.1, first approach; a). Furthermore, Schiff base substitution between lysine and DOPAquinone residues might occur (scheme 3.1, first approach; b). Both mechanisms were suggested for the coupling of protein to chitosan by using tyrosinase (Chen et al., 2001). However, covalent aryl-aryl or aryl-ether bonds due to aryloxy or semiquinone free radical coupling (scheme 3.1, first approach; c) are most likely to occur and have been described for the cross-linking of DOPA-bearing mussel adhesive proteins (Haemers et al., 2003). After formation of microscale aggregates due to the aforementioned cross-linking mechanisms, the hydrophobic clusters on the aggregate surfaces shield themselves in the aqueous environment and can assemble into larger fractal-like patterns, which subsequently organize and condense into filamentous structures (Murr et al., 2009; Chandler 2005).
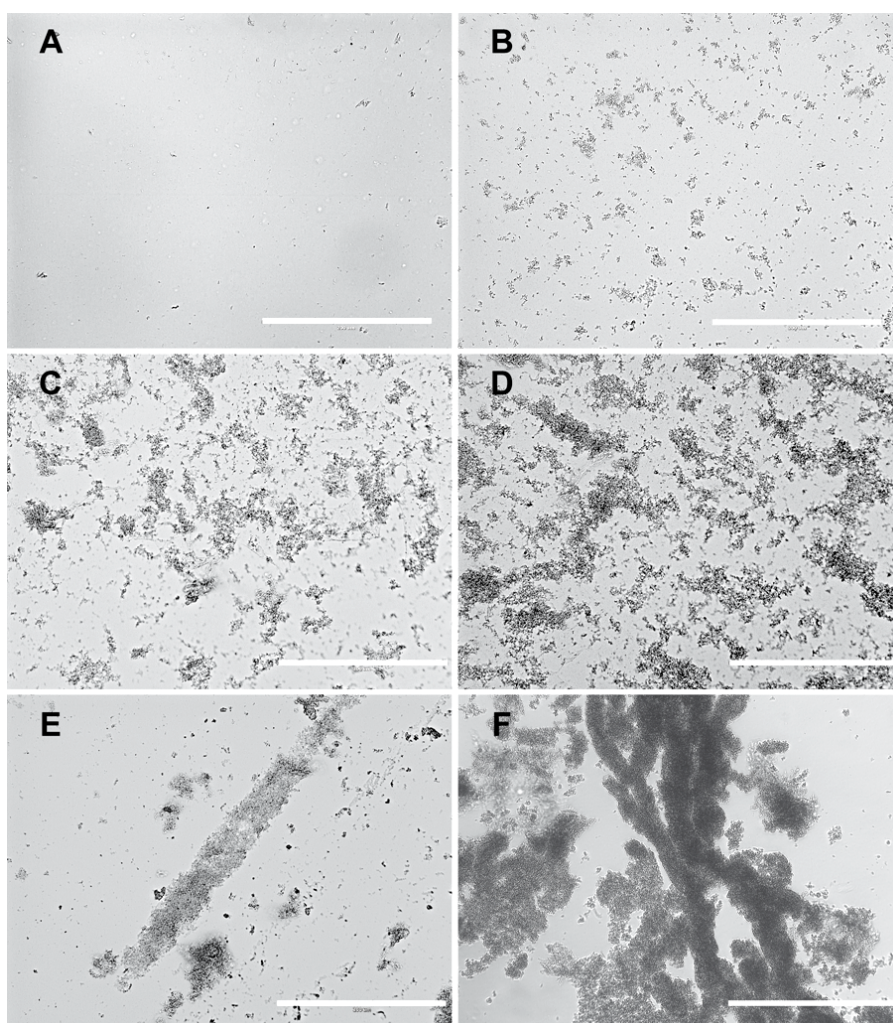
Fig. 3.2 Time-resolved self-assembly pathway of tyrosinase-modified recombinant silicatein aggregates to mesofilaments observed in their aqueous medium. Optical micrographs of silicatein that had remained untreated (A; control) or had been treated with tyrosinase for 5 min (B), 1 h (C), 3 h (D), 6 h (E), and 18 h (F). Bars, 200 µm (A-E), 400 µm (F).

Fig. 3.2 depicts the time-dependent aggregation of recombinant silicatein upon tyrosinase treatment, from fractal-like structures to mesoscale filaments after 18 h of incubation (B-F). In the control, recombinant silicatein had remained untreated during this time and showed no filament formation, with only few and small aggregates (A). This process of filament formation indicates a directional assembly, which is not solely based on tyrosinase-mediated cross-linking but might be driven by hydrophobic

interactions between fractally patterned aggregates, similar to those observed during axial filament formation *in vivo* (Murr & Morse, 2005; Müller et al., 2007). Moreover, these observations are consistent with both the different stages of silicatein fractal formation and the geometrical arrangement of the fractals to self-condensed filaments, proposed by computational modeling (Murr et al., 2009). Subsequently, the filaments were incubated with colloidal fluorescent core-shell silica spheres that had been prepared in a modified Stöber synthesis (Van Blaaderen & Vrij, 1992). The fluorophore was used in this study to monitor the assembly of the silica spheres; it was entrapped in the core to avoid interference of the protein-binding to the silanol-rich shell. The core-shell spheres, then, were incubated for 2 h with the mesoscale filaments with slow shaking. The resulting decoration of the filamentous templates with the fluorescent particles was monitored by using scanning electron microscopy (SEM), energy-dispersive X-ray spectroscopy (EDX), and fluorescence microscopy (FM) (Fig. 3.3). The SE micrograph in Fig. 3.3A represents the control and shows the relatively smooth surface of filaments that had remained untreated (i.e., without fluorescent core-shell silica spheres). Corresponding EDX revealed the spectral pattern characteristic of proteins (B); no fluorescence could be detected via FM (C). In contrast, upon exposure to the fluorescent silica particles, the filaments assisted their deposition, eliciting a rough surface. Furthermore, immobilization of the particles was substantiated by both EDX and FM that confirmed the presence of Si (E) and fluorescent particles (F) respectively. Interaction of silicatein with silica has been previously proposed to occur via hydrogen bonding in particular between the hydroxyl groups of a cluster of serine residues and surface silanol groups (Tahir et al., 2009; Wiens et al., 2013). The irregular spacing of these functional groups at geometrically distinct areas of the templating protein surface might be responsible for the inhomogeneous distribution of the silica spheres observed in this approach.
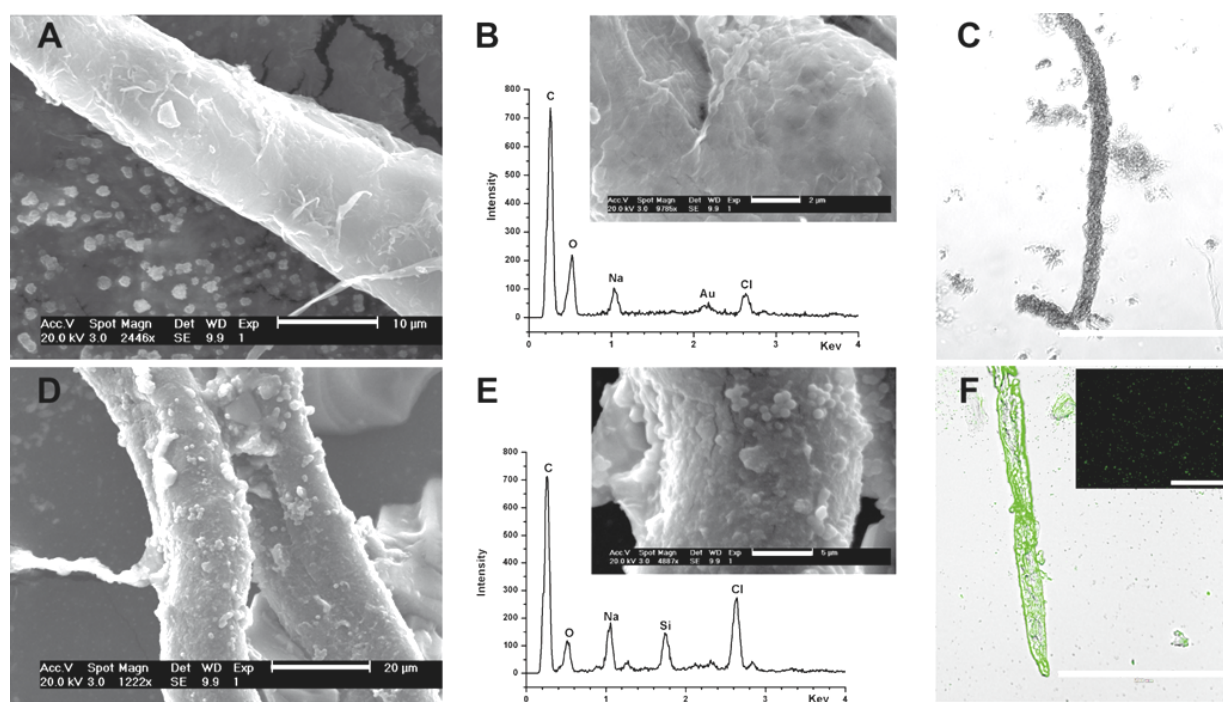
Fig. 3.3 Filaments of tyrosinase-modified silicatein as template for the deposition of fluorescent core-shell silica particles. Upper panels, control (i.e., filaments without silica spheres). SEM (A), EDX (B; inset, area of analysis), and FM (C). Lower panels, filaments with silica spheres. SEM (D), EDX (E; inset, area of analysis), and FM (F; inset, micrograph of the monodisperse fluorescent core-shell silica particles employed). Bars, 10 (A), 2 (B), 200 (C, F, inset), 20 (D), 5 μm (E).

In the second approach (scheme 3.1), a significant part of DOPAquinone residues was converted to DOPA in the presence of ascorbic acid as reductant to facilitate subsequent interfacial interactions with both silanol groups and oxygen of the siloxane groups of the silica surface (Mian et al., 2010). The immobilized protein layer increases in thickness by further protein cross-linking according to the first approach (Marumo & Waite, 1986). Patches of hydrophobic amino acid residues contribute to the mesoscale assembly and stabilization of the composite in a directional manner due to their specific location on the aggregate surface (Murr et al., 2009).
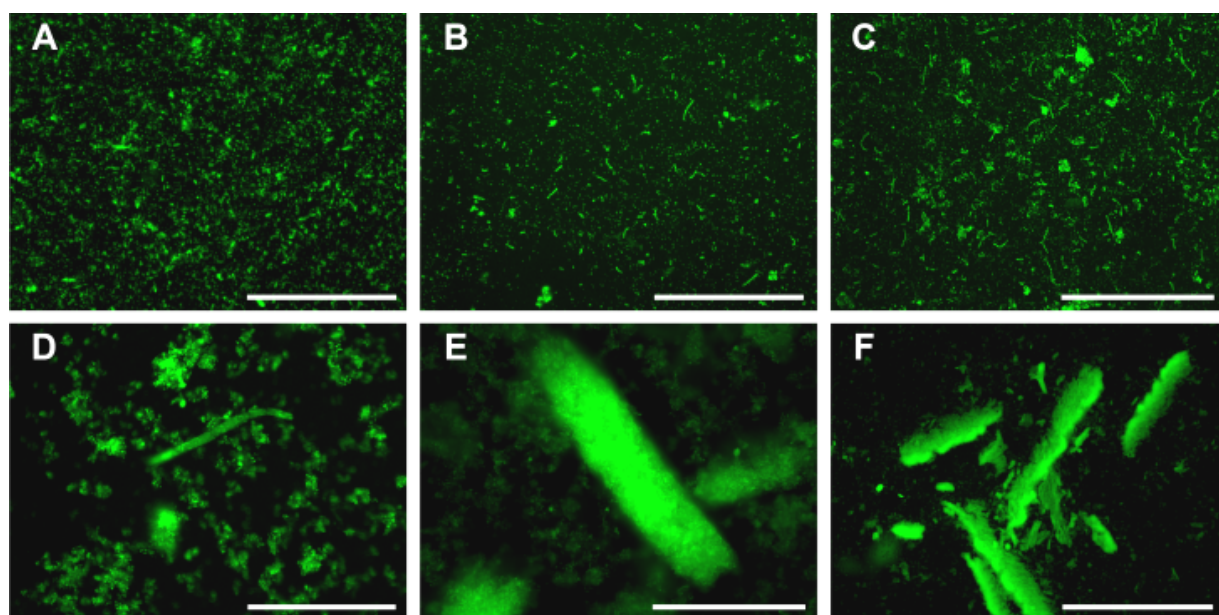
Fig. 3.4 Time-resolved fluorescence microscopy of the self-assembly of silicatein-coated silica core-shell particles upon incubation with tyrosinase. Silicatein-coated particles before tyrosinase treatment (A) and after treatment for 2 (C), 4 (D), 6 (E), and 18 h (F). During the same time (18 h) without tyrosinase treatment only microscale fibrous arrays of silicatein-coated particles were observed (B). Bars, 200 μm (A-E), 2000 μm (F).

To enhance the mutual interaction, in the second approach the fluorescent silica particles were preincubated for 2 h with recombinant silicatein with slow, tilted shaking before addition of tyrosinase and ascorbic acid (Marumo & Waite, 1986). The latter one was used as reductant to convert a significant part of the quinone to DOPA residues. DOPA is able to bind to various metal(loid) oxides (including SiO_2, TiO_2) through coordination, bidentate chelating and bridging, and hydrogen bonding (Mian et al., 2010; Ye et al., 2011; Yu et al., 2011). Thus, immobilization of silicatein oligomers and fractals, which had already occurred via the serine cluster, was enhanced through adhesive interaction between DOPA residues and silica. Concurrently, condensation and self-organization to fibrous silicatein/fluorescent silica composites was promoted, most probably through hydrophobic interactions between both the immobilized and the solute silicatein assemblies.
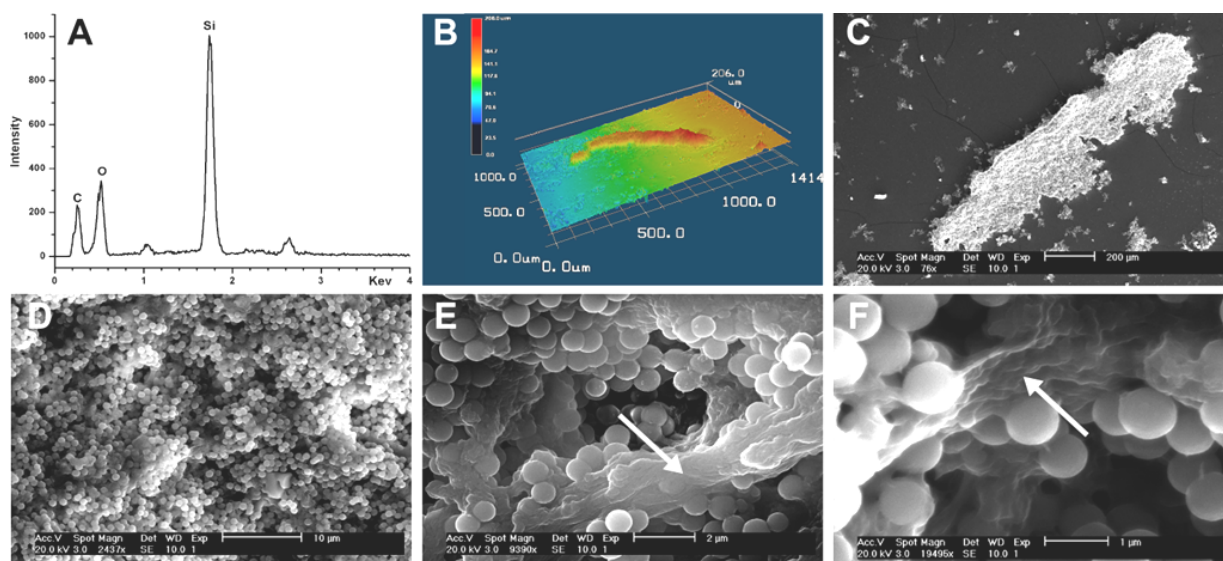
Fig. 3.5 Self-assembled silicatein-coated silica core-shell particles after 18 h of tyrosinase treatment. EDX (A), 3D-LSM (B), SEM (C-F). Note the fibrous protein matrix with embedded silica particles (arrows). Bars, 200 (C), 10 (D), 2 (E), and 1 (F) μm.

The fluorescence micrographs of Fig. 3.4 show the silicatein-coated silica particles before addition of tyrosinase (A) and their time-dependent assembly after addition of tyrosinase (C-F), resulting in fibrous fluorescent composites with sizes of up to several millimeters. After the same time without tyrosinase treatment, only few microscale fibrous arrays were observed (B). Moreover, EDX of the fibers (after 18 h of tyrosinase treatment) confirmed the presence of both silica and immobilized silicatein (Fig. 3.5A), whereas 3D laser scanning microscopy (LSM) revealed an average thickness of the fibers of 100 ± 20 μm (B). Concurrent SEM shows the distribution of the particles embedded within the protein matrix (C-F). The higher magnifications (E, F) depict the results of both interfacial interactions as well as directionally-controlled assembly. A comparison of the mesofibers obtained reveals differences in both dimension and morphology, which are a result of the two different methodological strategies: In the first approach, the morphology and size (length and width, up to 800 and 50 μm respectively) of the mesofibers is determined uniquely by the filamentous protein template and the availability of functional groups that are required for the immobilization

of silica spheres on the template surface. However, in the second approach the silicatein-coated silica spheres were integrated and well-distributed within the protein matrix during fiber formation. This fact resulted in mesofibers that do not carry a central protein filament. Thus, they appear more uneven in morphology than in the first approach, though larger in dimension (length and width, up to 2.0 mm and 300 µm respectively), which is also caused by the size of the embedded silica spheres (diameter, 600-800 nm).
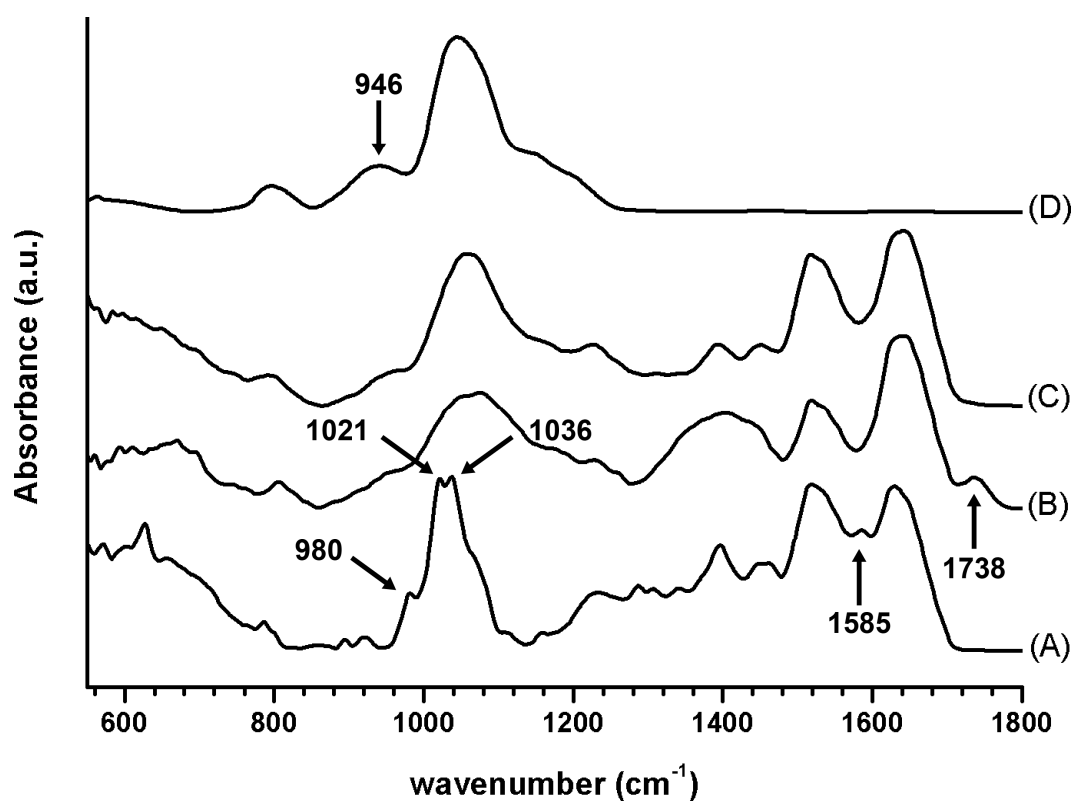

Fig. 3.6 FTIR-ATR of (A) lyophilized recombinant silicatein, (B) filaments of tyrosinase-modified silicatein, (C) fibrous silicatein/silica self-assemblies, and (D) pristine core-shell silica spheres.

Finally, Fourier transform infrared spectroscopy with attenuated total reflection (FTIR-ATR) was used to analyze cross-linking and interfacial interactions (Fig. 3.6). Thus, following tyrosinase treatment, the bands observed in the spectrum of lyophilized silicatein (A) at 980, 1021, and 1036 cm^{-1}, corresponding to the –CH$_2$–OH group of serine residues (Barth, 2000), broadened and shifted to 990-1150 cm^{-1} (B), probably caused by intermolecular hydrogen bonding during filament formation. Furthermore, the tyrosinase-mediated conversion of tyrosine residues was reflected by the disappearance of a peak at 1585 cm^{-1} in (A), which can be assigned to tyrosine side chains (Barth, 2000). At the same time the appearance of a peak at 1738 cm^{-1} in (B) indicates the formation of the diketone group of DOPAquinone (Kermasha & Tse, 2000). Upon incubation with silica under reducing conditions the intensity of this band decreases considerably (C), due to the conversion to DOPA residues (Baty et al., 1996). Concurrently, the Si–OH stretching band that can be observed in the spectrum of pristine core-shell silica spheres at 946 cm^{-1} (D) was markedly decreased in (C), probably caused by hydrogen bonding between the silanol groups and DOPA residues. Such strong bonds have been proposed to facilitate the adhesive interaction between silica and DOPA residues (Mian et al., 2010).

In conclusion, inspired by the remarkable optical and mechanical properties of natural siliceous sponge spicules, two molecular approaches have been developed that provide a facile means for preparing self-assembled fluorescent silicatein-silica hybrid mesofibers via enzymatic modification. These hybrid fibers might provide a source of inspiration for the fabrication of optical fibers at near-physiological conditions. Concurrently, the inorganic-organic composite qualifies as a versatile platform: By replacing the fluorescent core-shell building blocks employed here with e.g., silica-coated magnetic particles new functionalities can be introduced, thus allowing the fabrication of tailored hybrid materials for various applications. It should be noted that in the present approach silanol functionalities are required on the particle surface to facilitate interaction with the enzymatically modified DOPA residues of silicatein. In other studies, however, silicatein has been bioengineered to carry affinity sequences that facilitate binding to an array of materials including Au, TiO$_2$, and hydroxyapatite (Wiens

et al., 2012; André et al., 2011; Natalio et al., 2010). Hence, combination of the bioengineered and affinity-tagged silicatein with such core-shell entities considerably broadens the range of possible mesofibrous hybrids that could be used for fabrication of microdevices with potential application in the field of microelectronics, photovoltaics, or photocatalysts.

3.4 References

Aizenberg J., Sundar V.C., Yablon A.D., Weaver J.C. & Chen G. (2004). Biological glass fibers: correlation between optical and structural properties. *Proceedings of the National Academy of Sciences* 101, 3358-3363.

André R., Tahir M.N., Link T., Jochum F.D., Kolb U., Theato P., Berger R., Wiens M., Schröder H.C., Müller W.E.G. & Tremel W. (2011). Chemical Mimicry: Hierarchical 1D TiO2@ZrO2 Core−Shell Structures Reminiscent of Sponge Spicules by the Synergistic Effect of Silicatein-α and Silintaphin-1. *Langmuir 27*, 5464-5471.

Apetri M.M., Maiti N.C., Zagorski M.G., Carey P.R. & Anderson V.E. (2006). Secondary structure of α-synuclein oligomers: characterization by Raman and atomic force microscopy. *Journal of molecular biology* 355, 63-71.

Barth A. (2000). The infrared absorption of amino acid side chains. *Progress in biophysics and molecular biology* 74, 141-173.

Baty A.M., Suci P.A., Tyler B.J. & Geesey G.G. (1996). Investigation of mussel adhesive protein adsorption on polystyrene and poly (octadecyl methacrylate) using angle dependent XPS, ATR-FTIR, and AFM. *Journal of colloid and interface science* 177, 307-315.

Brutchey R.L. & Morse D.E. (2008). Silicatein and the translation of its molecular mechanism of biosilicification into low temperature nanomaterial synthesis. *Chemical reviews* 108, 4915-4934.

Chandler D. (2005). Interfaces and the driving force of hydrophobic assembly. *Nature* 437, 640-647.

Chen T., Vazquez-Duhalt R., Wu C.F., Bentley W.E. & Payne G.F. (2001). Combinatorial screening for enzyme-mediated coupling. Tyrosinase-catalyzed coupling to create protein-chitosan conjugates. *Biomacromolecules* 2, 456-462.

Croce G., Frache A., Milanesio M., Marchese L., Causà M., Viterbo D., Barbaglia A., Bolis V., Bavestrello G., Cerrano C., Benatti U., Pozzolini M., Giovine M. & Amenitsch H. (2004). Structural characterization of siliceous spicules from marine sponges. *Biophysical journal* 86, 526-534.

Griebenow K. & Klibanov A.M. (1995). Lyophilization-induced reversible changes in the secondary structure of proteins. *Proceedings of the National Academy of Sciences* 92, 10969-10976.

Haemers S., Koper G.J. & Frens G. (2003). Effect of oxidation rate on cross-linking of mussel adhesive proteins. *Biomacromolecules* 4, 632-640.

Heck T., Faccio G., Richter M. & Thöny-Meyer L. (2013). Enzyme-catalyzed protein crosslinking. *Applied microbiology and biotechnology* 97, 461-475.

Kermasha S. & Tse M. (2000). Biocatalysis of tyrosinase in chloroform medium, using selected phenolic substrates. *Journal of Chemical Technology and Biotechnology* 75, 475-483.

Khripin C.Y., Pristinski D., Dunphy D.R., Brinker C.J. & Kaehr B. (2011). Protein-directed assembly of arbitrary three-dimensional nanoporous silica architectures. *ACS nano* 5, 1401-1409.

Lee H., Dellatore S.M., Miller W.M. & Messersmith P.B. (2007). Mussel-inspired surface chemistry for multifunctional coatings. *Science* 318, 426-430.

Lee H., Scherer N.F. & Messersmith P.B. (2006). Single-molecule mechanics of mussel adhesion. *Proceedings of the National Academy of Sciences* 103, 12999-13003.

Marumo K. & Waite J.H. (1986). Optimization of hydroxylation of tyrosine and tyrosine-containing peptides by mushroom tyrosinase. *Biochimica et Biophysica Acta* 872, 98-103.

Mian S.A., Saha L.C., Jang J., Wang L., Gao X. & Nagase S. (2010). Density Functional Theory Study of Catechol Adhesion on Silica Surfaces. *The Journal of Physical Chemistry C* 114, 20793-20800.

Müller W.E.G., Boreiko A., Schloßmacher U., Wang X., Tahir M.N., Tremel W., Brandt D., Kaandorp J.A. & Schröder H.C. (2007). Fractal-related assembly of the axial filament in the demosponge *Suberites domuncula*: Relevance to biomineralization and the formation of biogenic silica. *Biomaterials* 28, 4501-4511.

Müller W.E.G., Schröder H.C., Muth S., Gietzen S., Korzhev M., Grebenjuk V.A., Wiens M., Schloßmacher U. & Wang X. (2013). The silicatein propeptide acts as

inhibitor/modulator of self-organization during spicule axial filament formation. *FEBS Journal* 280, 1693-1708.

Müller W.E.G., Wang X., Cui F. Z., Jochum K. P., Tremel W., Bill J., Schröder H.C., Natalio F., Schloßmacher U. & Wiens M. (2009). Sponge spicules as blueprints for the biofabrication of inorganic–organic composites and biomaterials. *Applied microbiology and biotechnology* 83, 397-413.

Müller W.E.G., Jochum K.P., Stoll B. & Wang X. (2008). Formation of giant spicule from quartz glass by the deep sea sponge Monorhaphis. *Chemistry of Materials* 20, 4703-4711.

Murr M.M. & Morse D.E. (2005). Fractal intermediates in the self-assembly of silicatein filaments. *Proceedings of the National Academy of Sciences* 102, 11657-11662.

Murr M.M., Thakur G.S., Li Y., Tsuruta H., Mezic I. & Morse D.E. (2009). New pathway for self-assembly and emergent properties. *Nano Today* 4, 116-124.

Natalio F., Link T., Müller W.E.G., Schröder H.C., Cui F.Z., Wang X. & Wiens M. (2010). Bioengineering of the silica-polymerizing enzyme silicatein-α for a targeted application to hydroxyapatite. *Acta biomaterialia* 6, 3720-3728.

Pallarès I., Vendrell J., Avilés F.X. & Ventura S. (2004). Amyloid fibril formation by a partially structured intermediate state of α-chymotrypsin. *Journal of molecular biology* 342, 321-331.

Patwardhan S.V., Holt S.A., Kelly S.M., Kreiner M., Perry C.C. & van der Walle C.F. (2010). Silica condensation by a silicatein α homologue involves surface-induced transition to a stable structural intermediate forming a saturated monolayer. *Biomacromolecules* 11, 3126-3135.

Polini A., Pagliara S., Camposeo A., Cingolani R., Wang X., Schröder H.C., Müller W.E.G. & Pisignano D. (2012). Optical properties of in-vitro biomineralised silica. *Scientific reports* 2, 607-612.

Rai A. & Perry C.C. (2012). Mussel adhesive protein inspired coatings: a versatile method to fabricate silica films on various surfaces. *Journal of Materials Chemistry* 22, 4790-4796.

Schloßmacher U., Wiens M., Schröder H.C., Wang X., Jochum K.P. & Müller W.E.G. (2011). Silintaphin-1–interaction with silicatein during structure-guiding bio-silica formation. *FEBS Journal* 278, 1145-1155.

Schröder H.C., Wiens M., Schloßmacher U., Brandt D. & Müller W.E.G. (2012). Silicatein-mediated polycondensation of orthosilicic acid: modeling of a catalytic mechanism involving ring formation. *Silicon* 4, 33-38.

Tahir M.N., Natalio F., Berger R., Barz M., Theato P., Schröder H.C., Müller W.E.G. & Tremel W. (2009). Growth of fibrous aggregates of silica nanoparticles: Fibre growth by mimicking the biogenic silica patterning processes. *Soft Matter* 5, 3657-3662.

Tahir M.N., Théato P., Müller, W.E.G., Schröder H.C., Borejko A., Faiß S., Janshoff A., Huth J. & Tremel W. (2005). Formation of layered titania and zirconia catalysed by surface-bound silicatein. *Chemical communications* 44, 5533-5535.

Van Blaaderen A. & Vrij A. (1992). Synthesis and characterization of colloidal dispersions of fluorescent, monodisperse silica spheres. *Langmuir* 8, 2921-2931.

Wei W., Yu J., Broomell C., Israelachvili J.N. & Waite J.H. (2012). Hydrophobic enhancement of dopa-mediated adhesion in a mussel foot protein. *Journal of the American Chemical Society* 135, 377-383.

Wiens M., Bausen M., Natalio F., Link T., Schlossmacher U. & Müller W.E.G. (2009). The role of the silicatein-α interactor silintaphin-1 in biomimetic biomineralization. Biomaterials 30, 1648-1656.

Wiens M., Link T., Elkhooly T.A., Isbert S. & Müller W.E.G. (2012). Formation of a micropatterned titania photocatalyst by microcontact printed silicatein on gold surfaces. *Chemical Communications* 48, 11331-11333.

Wiens M., Niem T., Elkhooly T.A., Steffen R., Neumann S., Schloßmacher U. & Müller W.E.G. (2013). Osteogenic potential of a biosilica-coated P (UDMA-co-MPS) copolymer. *J. Mater. Chem. B.* 1, 3339-3343.

Ye Q., Zhou F. & Liu W. (2011). Bioinspired catecholic chemistry for surface modification. *Chemical Society Reviews* 40, 4244-4258.

Yu J., Wei W., Danner E., Ashley R.K., Israelachvili J.N. & Waite J.H. (2011). Mussel protein adhesion depends on interprotein thiol-mediated redox modulation. *Nature chemical biology* 7, 588-590.

Chapter 4

Osteogenic potential of a biosilica-coated P(UDMA-*co*-MPS) copolymer

4.1 Introduction

Many bone defects that are caused by a variety of factors can be treated by implantation of bone substitutes. Autologous grafts from various donor sites are the gold standard for bone repair and substitution in clinical medicine, since they possess bioactive, osteoinductive, and osteoconductive potential. However, implantation of autologous bone is hampered by its limited availability and the risk of pain and morbidity of the donor. Hence, in search for alternative bone replacements, synthetic materials have been increasingly attracting attention, including hydroxyapatite (HA), β-tricalcium phosphate, calcium carbonate, and bioactive glass (LeGeros, 2008; Oudadesse et al., 2007; Hench, 2006; Arcos & Vallet-Regí 2010). Ideally, such materials stimulate the formation of HA-like surface layers, which facilitate direct bonding with living bone (Will et al., 2012). Acrylics such as polyurethane dimethacrylate (PUDMA) and polymethylmethacrylate (PMMA) are widely applied e. g., as (i) bone cement for fixation of medical implants with living bone, (ii) injectable cement for bone augmentation and reconstruction in orthopedics, or (iii) filler, dental adhesive, and fiber-reinforced composite for root pins in dentistry (Kenny & Buggy, 2003; Jaeblon, 2010; Deb et al., 2005; Van Landuyt et al., 2007; Lewis, 2011). However, these polymers generally lack bioactivity and osteoconductivity. Therefore, PMMA has been modified with methacryloxypropyltrimethoxysilane (MPS) whose surface silanol groups trigger HA nucleation in contact with body fluid (Tsukeoka et al., 2006; Sugino et al., 2008; Kanie et al., 2004). With the discovery of the enzyme silicatein a versatile molecular tool has become available to harness biosilicification. Silicatein is related to cathepsin proteases and catalyzes the polymerization of silicate to amorphous, hydrated silica (biogenous silica; biosilica) (Cha et al., 1999). In a recently developed model, silicatein mediates

(*via* its catalytic triad Ser25, His165, Asn185) the synthesis of reactive, cyclic silicic acid species from very low concentrations of the monomeric precursor (Schröder et al., 2012). Due to its unique structural and molecular features as well as its enzymatic synthesis at near-physiological conditions, biosilica has the extraordinary properties of advanced materials, exceeding current human engineering capabilities (Müller et al., 2009). Most noteworthy and similar in effect to bioactive glass, biosilica has been shown to stimulate proliferation and activity of human osteoblast-like cells (SaOS-2; a non-transformed cell line derived from primary osteosarcoma cells), resulting in an increased formation of HA. This osteogenic effect has been attributed to the enhanced expression of BMP-2 and OPG (Wiens et al., 2010b; Wiens et al., 2010c). In addition, biosilica has been shown to alter the expression of genes that are crucial for amelogenesis (Müller et al., 2007). A first prototypic bioactive implant material that comprised the enzyme silicatein and its silicate substrate has been tested *in vivo* (Wiens et al., 2010a). Since then, the spectrum of possible biomedical (and biotechnological) applications of silicatein has been extended through bioengineering of the enzyme to fabricate hybrid proteins with tags that confer binding affinity to various substrates (André et al., 2011; Wiens et al., 2012). Upon immobilization, tagged silicatein was shown to catalyze the synthesis of biosilica coatings e. g., on synthetic and dental HA (Natalio et al., 2010).

In this chapter, silicatein is immobilized on silanized surface consists of P(UDMA-*co*-MPS) copolymer and the subsequent formation of biosilica by using the catalytic activity of silicatein. The silanol-bearing acrylate copolymer might consider as a suitable substrate for silicatein because of its reported templating ability for the amorphous form of silicon dioxide *via* hexaserine clusters on silicatein surface. The chemical structure of the copolymer and the proposed immobilization mechanism of silicatein are illustrated in scheme 4.1
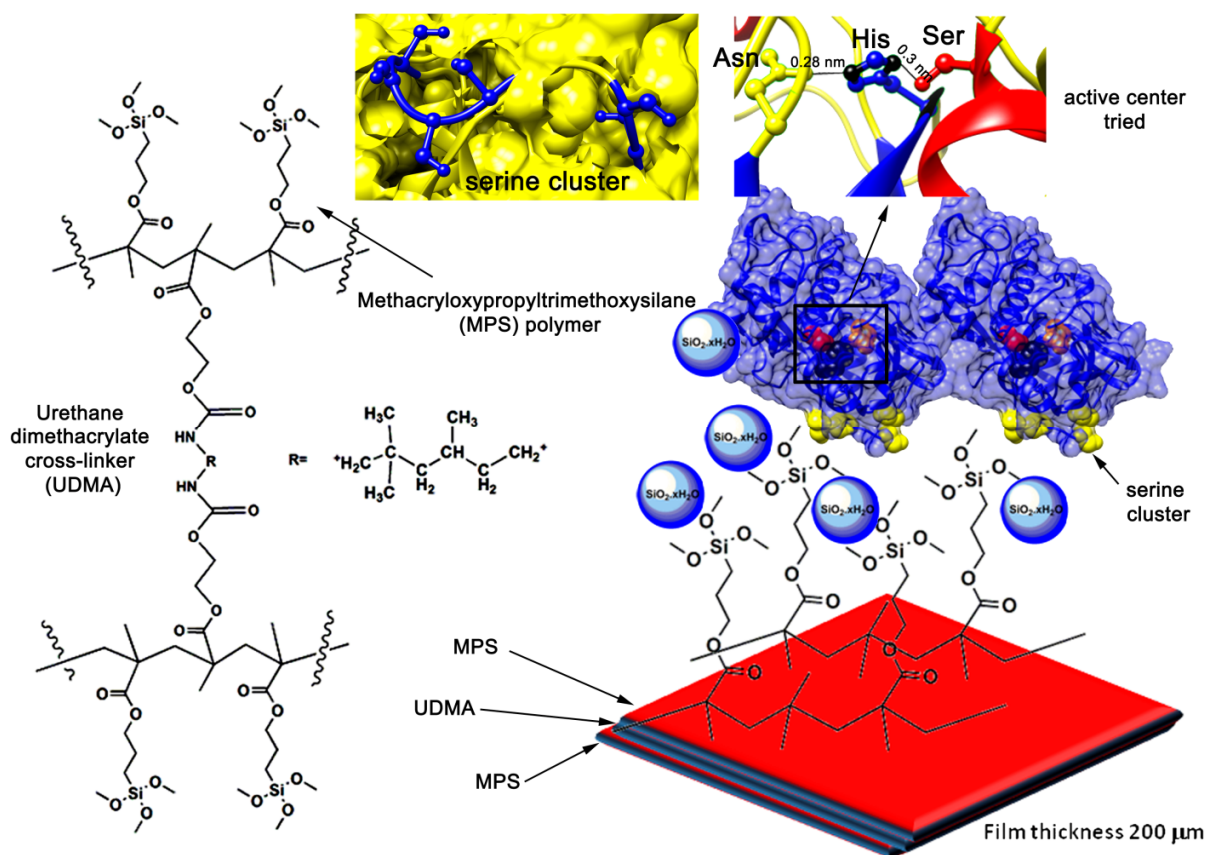
Scheme 4.1 the chemical structure of P(UDMA-*co*-MPS) copolymer formed by free radical polymerization and the suggested facial interaction (hydrogen bond) between the surface silanol groups and the serine cluster of recombinant silicatein-α, the catalytic triad in silicatein active center (serine; Ser #25, histidine; His #165, asparagine; Asn #185) promote the biopolycondensation of orthosilicic acid monomers to form hydrated amorphous silica ($SiO_2.xH_2O$) termed as biosilica (blue spheres).

4.2 Experimental section

4.2.1 Preparation of P(UDMA-*co*-MPS) copolymer

The P(UDMA-*co*-MPS) copolymer carriers were obtained by mixing equal amounts of urethane dimethacrylate (UDMA) and methacryloxypropyltrimethoxysilane (MPS) with a combination of benzoyl peroxide and photoinitiator. The mixture was cast to shape circular specimens (ca. 200 μm thickness), light cured (400-500 nm, 5 min), and heated (100 °C, 30 min).

4.2.2 Nanoindentation measurements and parameters of the copolymer

To determine elastic modulus and Martens hardness, 20 indents per sample were taken with a Berkovich tip, with a minimum spacing of 50 μm, using a NanoTest Vantage platform (Micro Materials, Wrexham, UK). For the first contact, the indenter velocity was set to 0.2 μms^{-1} and the initial contact force was kept constant to 0.05 mN. A maximum load of 10 mN was applied, with a 0.5 mNs^{-1} loading/unloading rate. To minimize the influence of viscoelastic deformation, the loading history comprised a hold for 120 s at constant maximum load before unloading. During this hold, displacement data were collected to determine the creep response. In the unloading history a second dwell period (300 s) was used at 10 % of the maximum load to assess the thermal drift of the system. The elastic modulus and the hardness were extracted from the unloading data (Oliver & Pharr, 1992; Lee et al., 2007).

4.2.3 Surface-functionalization of P(MMA-co-MPS) carriers

To facilitate the subsequent silicatein-mediated silica polycondensation reaction, the methoxysilyl-functionalized polymer was shortly incubated with 10 mM HCl, thereby converting surface silicon alkoxy side groups to silanol (Schloßmacher et al., 2011). To generate a biosilica-coating, the P(MMA-*co*-MPS) carriers (and the PMMA control) were successively dipped into a solution of 120 μg/ml recombinant mature silicatein-α (aa$_{115-330}$; in phosphate-buffered saline [PBS]) and a solution of 1.0 mM orthosilicate (in 50 mM Tris-HCl, pH 7.4) for 12 and 2 h respectively. Orthosilicate was prepared from prehydrolyzed tetraethyl orthosilicate (TEOS) as described (Wiens et al., 2010c; Natalio

et al., 2010). In short, a stock solution of 5 mM TEOS was mixed in a 1:3 M ratio with 1 mM HCl for 30 min and subsequently neutralized.

4.2.4 Analysis techniques for copolymer and immobilized silicatein

FTIR spectroscopy has been used in the attenuated total reflectance (ATR) mode to investigate the surface chemistry (FTIR-ATR; Varian 660-IR spectrometer with Golden Gate ATR accessory), and scanning electron microscopy (SEM; LEO Gemini 1530; Zeiss, Oberkochen, Germany). Spectra were collected at a resolution of 4 cm^{-1} and averaging for 32 scans over the range of 4000–550 cm^{-1}.

For immunodetection of surface-immobilized silicatein, the PMMA and P(MMA-*co*-MPS) carriers were incubated for 90 min (RT) with silicatein specific primary antibodies (diluted 1:1,000 in 15% blocking solution [Roche Applied Science, Mannheim, Germany]), followed by an incubation with Cy3-labeled species-specific secondary antibodies (diluted 1:8,000; 90 min, RT) (Dianova, Hamburg, Germany) (Wiens et al., 2009). Then, the samples were inspected by a Zeiss 710 CLSM (Carl Zeiss GmbH, Göttingen, Germany), using the 543 nm line of the helium/neon laser.

4.2.5 Mineralization of osteoblastic SaOS-2 cells on P(MMA-*co*-MPS) carriers

To investigate the effect of the biosilica-coated P(MMA-*co*-MPS) carriers on mineralization of osteoblastic cells, HA formation of SaOS-2 cells was analyzed. For this purpose, SaOS-2 cells (ATCC HTB-85) were cultured in McCoy's Medium Modified, supplemented with 15 % fetal calf serum in a humidified incubator at 37 °C and 5 % CO2. For the experiments, cells were seeded in multiwell plates onto P(MMA-*co*-MPS) discs (or PMMA as control) with a thickness of 200 μm. Where indicated, the discs had been coated with biosilica *via* immobilized silicatein. Furthermore, where indicated, the medium was supplemented after 3 d with DAAG cocktail (10 nM dexamethasone, 50 μM ascorbic acid, and 5 mM β-glycerophosphate) to stimulate mineralization for 7 d as previously described (Wiens et al., 2010b). To study mineralization by CLSM, cells on discs were washed several times with PBS, fixed in 4% [w/v] paraformaldehyde (5 min, RT), and permeabilized with 0.2 % [v/v] Triton X-100 (5 min, RT). Then, cells were

blocked with 1 % [v/v] bovine serum albumin (in PBS; 30 min) and stained with OsteoImage (HA stain; Lonza, Cologne, Germany). Finally, the cells were counterstained with rhodamine phalloidin (actin cytoskeleton stain; Life Technologies, Darmstadt, Germany) and DRAQ5 (nuclear stain; Biostatus Ltd., Shepshed, UK), according to the manufacturers' instructions. Micrographs were acquired on a Zeiss 710 CLSM. The argon laser line of 488 nm was used to excite OsteoImage, whereas the 543 nm and the 633 nm line of a helium/neon laser were used to excite rhodamine phalloidin and DRAQ5 respectively. Concurrently, to quantitatively assess mineralization by fluoroscopy, cells were washed several times with PBS and fixed in ethanol for 20 min. Following incubation with OsteoImage and further washing, fluorescence was quantified using a Varioskan plate reader (Thermo Fisher) at 492/520 nm (excitation/emission wavelengths).

4.2.6 Alkaline phosphatase activity as an osteogenic marker of osteoblastic SaOS-2 cells

To investigate the alkaline phosphatase (ALP) activity, SaOS-2 cells were cultivated as described above on P(UDMA) or silanol-functionalized P(UDMA-*co*-MPS) carriers in medium supplemented with DAAG for 7 days. The carriers had been treated with silicatein/orthosilicate or remained untreated. For semi-quantitative analyses, an ALP kit (Sigma-Aldrich, Taufkirchen, Germany) was used. Hence, the cells were fixed, incubated in the ALP staining solution (containing naphthol AS-BI phosphate and fast red violet LB salt) for 15 min (RT), and counterstained with hematoxylin for 2 min, according to the manufacturer's protocol. Subsequently, the stained cells were inspected by phase contrast microscopy (EVOS XL, Life Technologies). Concurrently, ALP activity was determined spectrophotometrically for quantitative analyses. Thus, the cells were lysed in 10 mM Tris, 1 mM $MgCl_2$, and 0.1 % (v/v) Triton X-100, followed by three freeze-thawing cycles (at -80 °C and 37 °C). After centrifugation (15,000 g, 15 min, 4 °C), the supernatants were collected and used to determine both protein concentrations (QuantiPro BCA Protein Assay Kit, Sigma-Aldrich) and ALP activity. The latter one was calculated as the rate of p-nitrophenol production from p-nitrophenyl phosphate substrate (pNPP; SIGMAFAST p-nitrophenyl phosphate tablets, Sigma-

Aldrich). For this purpose, 200 µl of a pNPP solution (1.0 mg/ml pNPP, in 0.2 M Tris and 5 mM MgCl$_2$) were added to 5 µl of cell lysate. After incubation at 37 °C for 10 min, the reaction was stopped by addition of 50 µl of 3 M NaOH. Then, the amount of p-nitrophenol produced was determined spectrophotometrically (405 nm) based on a corresponding standard curve. To calculate the ALP activity, the amount of p-nitrophenol was normalized by the total protein content.

4.2.7 Statistical analysis

Data are expressed as means ± SD of five replicates. Statistical differences between the samples were assessed by Student's t-test.

4.3 Results and discussion

To assess whether the resulting silanol-functionalized P(UDMA-*co*-MPS) has altered surface mechanical properties (compared to conventional PUDMA, prepared without addition of MPS), the elastic modulus and Martens hardness were determined by nanoindentation. Whereas hardness defines the resistance of a material to plastic deformation, the elastic modulus represents the elastic deformation of a material upon force application. Both of these mechanical properties may be used to predict wear resistance (Leyland & Matthews, 2000). Accordingly, 20 indents per sample were taken with a Berkovich tip, applying a maximum load of 10 mN, with a 0.5 mNs^{-1} loading/unloading rate (Fig. 4.1). The elastic modulus and the hardness were extracted from the unloading data (Oliver & Pharr, 1992; Lee et al., 2007). The subsequent comparison between the P(UDMA-*co*-MPS) and PUDMA polymers revealed only slightly altered values, which are close to those recently reported for PMMA (Skarmoutsou et al., 2012; Briscoe et al., 1998). Thus, the hardness of the copolymer was reduced by ca. 3.2 % (268 ± 4.0 vs. 277 ± 4.0 MPa; [mean ± SD]). Concurrently, a slightly decreased (ca. 4.5 %) elastic modulus was observed (5.71 ± 0.07 vs. 5.98 ± 0.06 GPa). These values are indicative of overall unaltered surface mechanical properties of the copolymer compared to plain PUDMA. Consequently, the effect of the

surface mechanics such as higher stiffness on the cellular behaviors can be neglected and any osteogenic cellular response could be attributed to surface modification with biosilica.
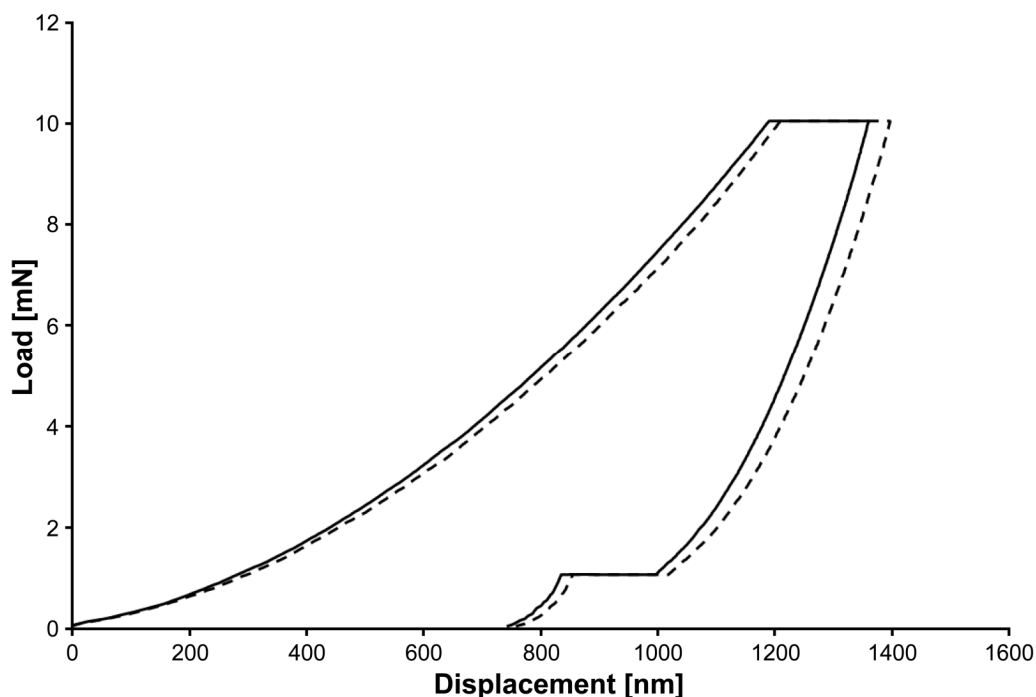

Fig. 4.1 Load-displacement curves of plain PUDMA (solid line) and P(UDMA-*co*-MPS) (dashed line), obtained by nanoindentation.

To generate a biosilica coating, the polymer carriers were incubated for 12 h with 120 µg/ml recombinant mature silicatein-α (aa$_{115-330}$; in phosphate-buffered saline [PBS]) and, then, for 2 h with 1.0 mM orthosilicate (prepared from pre-hydrolyzed tetraethyl orthosilicate [TEOS]) (Wiens et al., 2010c). During this time, surface silanol groups were cross-linked to soluble orthosilicate, resulting in a three-dimensional surface silica network. Silicatein immobilization and biosilica formation was confirmed by Fourier transform infrared spectroscopy with attenuated total reflection (FTIR-ATR), confocal laser scanning microscopy (CLSM), and scanning electron microscopy (SEM).

Fig. 4.2 shows the spectra obtained by FTIR-ATR. Compared to the PUDMA control (spectrum A), the spectrum of P(UDMA-*co*-MPS) (B) revealed the characteristic Si–O–C stretching bands at 814 (symmetric) and 1078 cm^{-1} (asymmetric), which decreased or disappeared upon treatment with HCl (D) (Alexander et al., 1985; Pantoja et al., 2009; Emmons et al., 2007). This hydrolysis of the MPS alkoxide gives Si–OH groups, reflected by a broad band at 865-910 cm^{-1} (Pantoja et al., 2009). Furthermore, some of the silanol groups reacted with each other through autocondensation, resulting in the formation of mostly linear structures, which can be followed by the characteristic Si–O–Si stretching bands at 1110 (symmetric) and 1153 cm^{-1} (asymmetric) (Rubio et al., 1998). As expected, the aforementioned peaks can't be detected in the PUDMA control sample prepared without MPS (A), and treatment with HCl does not affect its spectrum (C). Following immobilization of recombinant silicatein on HCl-treated P(UDMA-co-MPS), the spectrum (E) shows additional bands at 1034 and 1633 cm^{-1} that correspond to Ser C–O stretching and C=O stretching (amide I band) vibrations respectively, characteristic for the presence of protein (Barth, 2007) and, thus, indicative of the immobilization of silicatein onto P(UDMA-co-MPS). This immobilization might be facilitated by hydrogen-bonding e. g., between the hydroxyl groups of a cluster of serine residues and the silanol groups, which would explain the decreased Si–OH band intensity at 865-910 cm^{-1} in (E) compared to (D). Ultimately, incubation with orthosilicate of surface-functionalized P(UDMA-*co*-MPS) samples that carried surface-immobilized silicatein increased the intensities of the characteristic Si–O–Si stretching bands of cyclic structures at 1050-1086 (symmetric) and 1200 cm^{-1} (asymmetric), which can be assigned to a three-dimensional cross-linking of silanol groups (F) (Rubio et al., 1998; Chang et al., 2007). Furthermore, the formation of such a surface silica network is supported by both the decreased linear siloxane band intensities at 1110 and 1153 cm^{-1} (compared to (D)) and the appearance of a band at 3187 cm^{-1}, which is exclusive to this spectrum and might arise from hydrogen-bonded silanol groups and polymerization of orthosilicate (Watanabe et al., 1995).
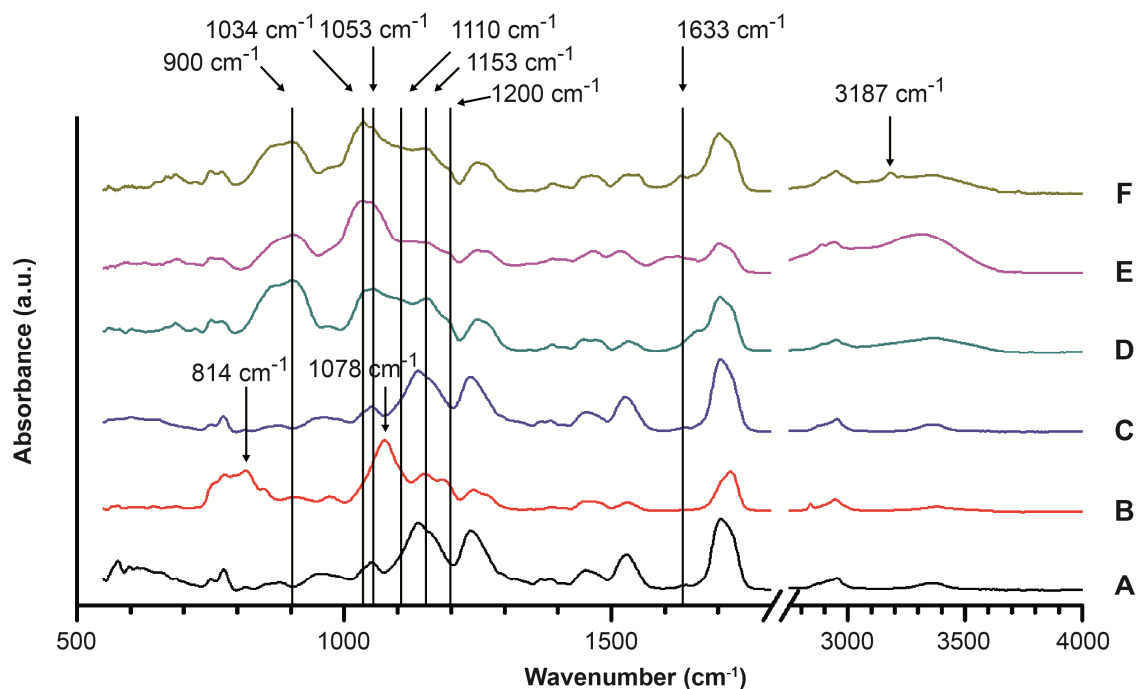
Fig. 4.2 Comparison of FTIR-ATR spectra of PUDMA and P(UDMA-co-MPS). As-prepared PUDMA (A) and P(UDMA-*co*-MPS) (B); HCl-treated PUDMA (C) and P(UDMA-*co*-MPS) (D); P(UDMA-*co*-MPS) incubated with recombinant silicatein (E) or with recombinant silicatein and orthosilicate (F).

Furthermore, surface-immobilized silicatein was immunodetected with a combination of specific primary antibodies, Cy3-labeled secondary antibodies, and CLSM, using the 543 nm line of the helium–neon laser. Fig. 4.3 (A, B) depicts immunodetected silicatein on the surface of PUDMA and P(UDMA-*co*-MPS) samples. Whereas, in case of the control PUDMA sample (A) the resulting weak fluorescence signals are indicative of a marginal and unspecific binding of the enzyme, the P(UDMA-*co*-MPS) sample (B) emitted strong signals, demonstrating a substantial immobilization of silicatein onto the surface. As suggested by the FTIR-ATR results, this immobilization might be facilitated by the surface silanol groups that interact with the hydroxyl groups of a silicatein-specific cluster of serine residues. These hydroxyl groups have been proposed to cross-link the enzyme to orthosilicate and silica, acting as a template for biosilica deposition (Wang et al., 2012). Concurrently, the samples were analyzed by SEM. Fig. 4.3 (C, D) compares the surface morphology of a pristine PUDMA control (C) with that of a

P(UDMA-*co*-MPS) sample (D), both of which had been incubated with silicatein and orthosilicate. Whereas the PUDMA control featured a relatively smooth and non-porous surface morphology, the P(UDMA-*co*-MPS) sample revealed not a homogenous matrix but rather a distinct and porous surface-coating, similar to that previously obtained by coating of cell culture plates with silicatein/biosilica (Wiens et al., 2010c).
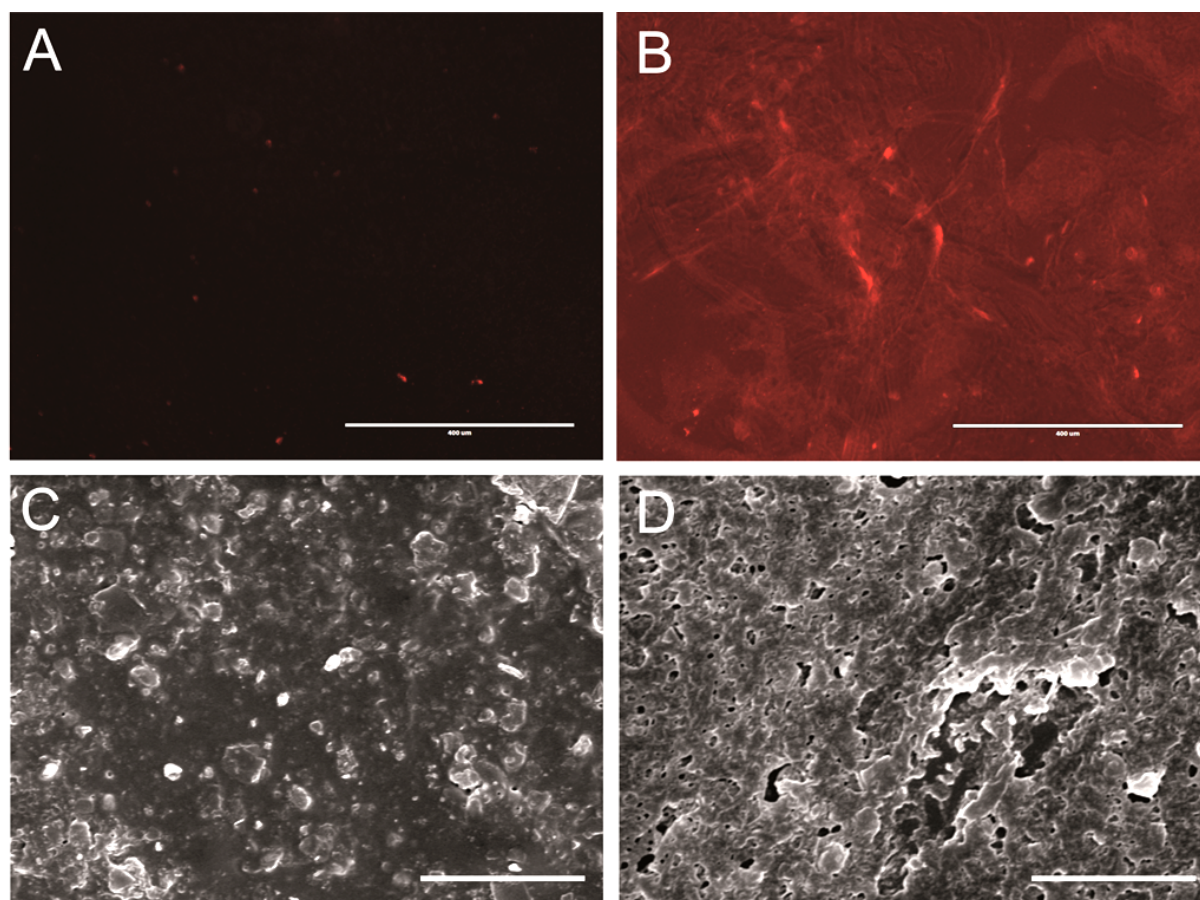

Fig. 4.3 Surface-functionalized P(UDMA-*co*-MPS) carriers. (A, B) Immunodetection: Surface-immobilized silicatein was immunodetected with a combination of specific primary antibodies, Cy3-labeled secondary antibodies, and CLSM on PUDMA (A; control) or P(UDMA-*co*-MPS) (B). (C, D) SE micrographs of surface morphologies: PUDMA (C) or P(UDMA-*co*-MPS) (D). Bars, 400 μm (A, B); 10 μm (C, D).

To investigate the effect of the biosilica-coated P(UDMA-*co*-MPS) on mineralization of osteoblastic cells, HA formation of SaOS-2 cells was analyzed. SaOS-2 cells have a mature osteoblastic phenotype and possess a high matrix mineralization capacity (Müller et al., 2011). Consequently, they are a suitable model for assessing the osteogenic potential of various materials. For the experiments, SaOS-2 cells were seeded in multiwell plates onto PUDMA or P(UDMA-*co*-MPS) membranes. Where indicated, McCoy's Medium Modified was supplemented with DAAG cocktail (10 nM dexamethasone, 50 µM ascorbic acid, and 5 mM β-glycerophosphate) to stimulate mineralization for 7 d as described previously (Wiens et al., 2010b). Then, the cells were washed and fixed. To study mineralization by CLSM, cells on discs were stained with OsteoImage (HA stain), and counterstained with rhodamine phalloidin (actin cytoskeleton stain) as well as DRAQ5 (nuclear stain). In Fig. 4.4, the upper panel of CLSM micrographs depicts the effect of both biosilica coating of pristine PUDMA carriers and presence of DAAG cocktail in the culture medium on mineral deposition by SaOS-2 cells (A-D). In detail, (A) and (B) show SaOS-2 cells seeded on pristine PUDMA and cultured in medium without osteogenic DAAG cocktail. Whereas in (A) no significant OsteoImage staining of mineral deposits can be observed, multiple small deposits are detected in (B), possibly caused by silicatein-synthesized biosilica that had adsorbed to PUDMA. As expected, supplementation of the culture medium with DAAG triggered formation of mineralized nodules by SaOS-2 cells, as shown in (C) and (D). However, the deposits are more abundant and bulkier in (D) than in (C), which might be due to the synergistic effect of DAAG and PUDMA-adsorbed biosilica on mineralization. The lower panel of CLSM micrographs, again, depicts the effect of biosilica coating and DAAG cocktail on mineralization of SaOS-2 cells (E-H). In this set of experiments, however, the cells were grown on silanol-functionalized P(UDMA-*co*-MPS) carriers. (E) and (F) show SaOS-2 cells that were cultured in medium without DAAG cocktail. In both cases, the OsteoImage staining of HA is more pronounced than in the corresponding PUDMA samples (A) and (B). This suggests an enhanced bioactivity, probably caused by surface silanol groups.
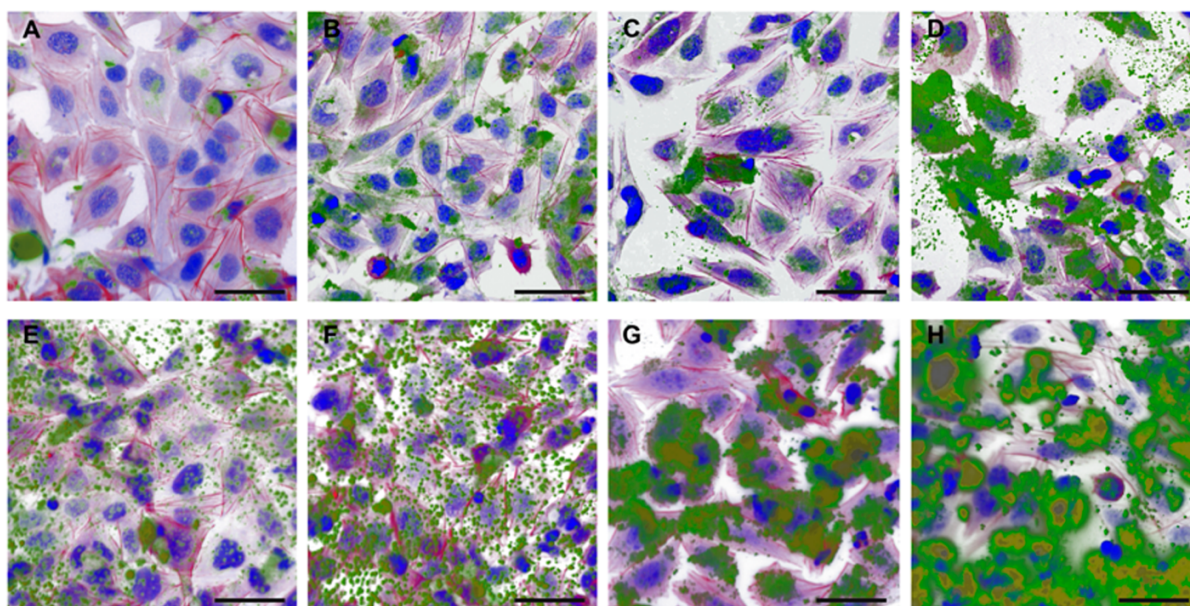
Fig. 4.4 Mineralization of SaOS-2 cells, qualitatively assessed by CLSM. Prior to cell seeding the PUDMA and P(UDMA-co-MPS) carriers had been incubated with recombinant silicatein and orthosilicate (+silicatein/OS) or had remained untreated (–silicatein/OS) as indicated. The culture medium was supplemented with dexamethasone, ascorbic acid, and β-glycerophosphate (medium plus DAAG) or it remained devoid of supplements (medium minus DAAG). Note the differences in staining intensity and pattern of mineralization. Cell nuclei, cytoskeleton, and mineral deposits were fluorescently stained with DRAQ5, rhodamine phalloidin, and OsteoImage respectively. Bars, 50 µm.

Additionally, the silicatein-synthesized and surface-immobilized biosilica facilitated cell mineralization in (F), probably by triggering osteogenic cellular signal cascades (Wiens et al., 2010b; Wiens et al., 2010c). This trend is continued in (G) and (H), where supplementation of the medium with DAAG further increased mineral deposition, resulting in abundant and bulky HA aggregates that cover the carrier more extensively in (H) than in (G) (and in both more extensively than in the corresponding PUDMA samples (D) and (C)). Concurrently, mineralization was quantified fluorometrically, using OsteoImage staining of HA. Thus, SaOS-2 cells were cultivated on PUDMA or P(UDMA-*co*-MPS) discs that had been treated with silicatein/orthosilicate. Where indicated, the medium had been supplemented with DAAG for 7 d. Fig. 4.5 shows that DAAG supplementation stimulated mineralization of cells grown on both PUDMA

(control) and P(UDMA-*co*-MPS) as expected. However, on the latter samples HA formation was increased by ca. 1.9-fold, compared to the DAAG supplemented control. Furthermore, even without DAAG stimulation, mineralization was considerably enhanced in case of the P(UDMA-*co*-MPS) carriers (ca. 5.4-fold; compared to the non-supplemented control). In contrast, fluorescence of the PUDMA samples without DAAG supplementation remained negligible. These results show that even in the absence of osteogenic DAAG supplements the surface-functionalized P(UDMA-*co*-MPS) copolymer triggers mineral deposition in cell culture, consequently demonstrating its osteogenic potential.
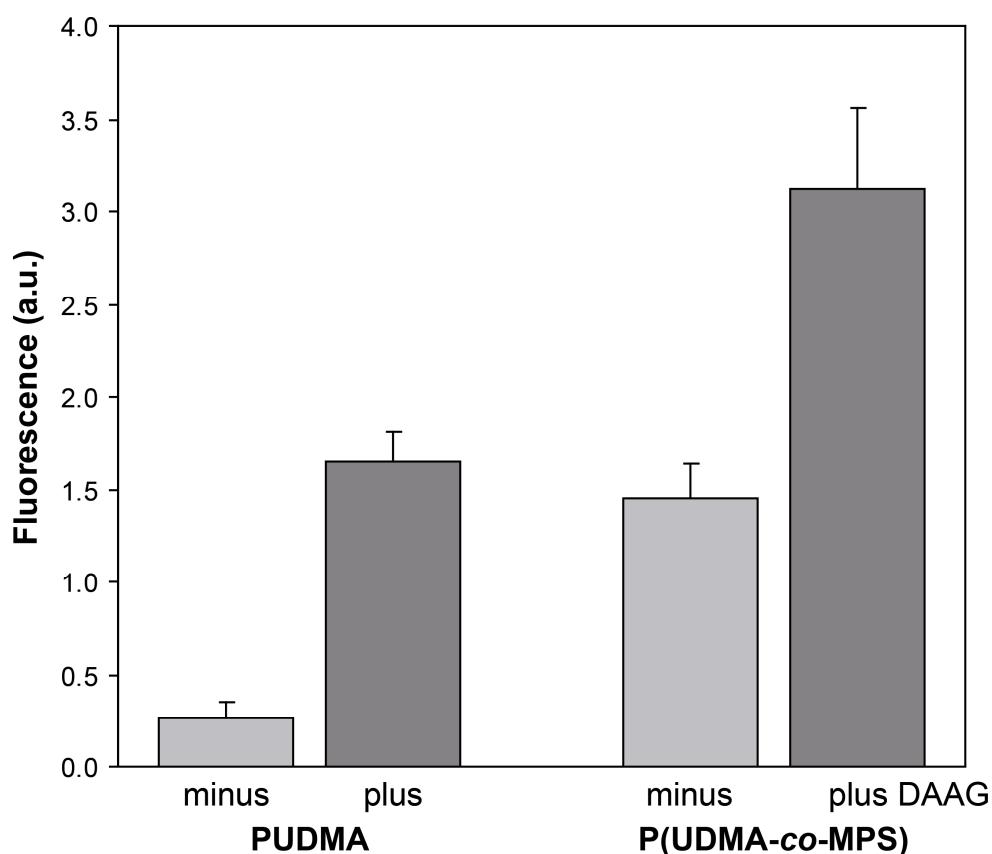

Fig. 4.5 Mineralization of SaOS-2 cells, quantitatively assessed by fluoroscopy. Cells were grown on PUDMA or P(UDMA-*co*-MPS) carriers that had been treated with recombinant silicatein and orthosilicate. Medium was supplemented with DAAG (dark grey columns) or remained non-supplemented (light grey). Mineral deposits were stained with OsteoImage.

Finally, alkaline phosphatase (ALP) activity as a marker for osteogenic activity was determined (Fig. 4.6) (Müller et al., 2011). For this purpose, SaOS-2 cells were cultivated in DAAG supplemented medium on PUDMA or P(UDMA-*co*-MPS) discs that had remained untreated (A, C) or had been treated with silicatein/orthosilicate (B, D) respectively. Subsequently, the cells were incubated in an ALP staining solution and inspected by optical microscopy. (A) and (B) depict the staining of cells grown on PUDMA carriers: Compared to (A), the staining of (B) indicates an increased ALP activity, possibly caused by silicatein-synthesized biosilica that had adsorbed to PUDMA. Furthermore, (C) and (D) depict the staining of cells grown on P(UDMA-co-MPS). In both cases, the staining is more pronounced than in the corresponding PUDMA samples (A) and (B) and, additionally, more pronounced in (D) than in (C), which might be due to the synergistic effect of biosilica and surface silanol groups. In parallel, ALP activity was quantified spectrophotometrically by determining the release of p-nitrophenol from the chromogenic substrate p-nitrophenyl phosphate (pNPP). Upon normalization of the data to the total protein amount, ALP activity, then, was expressed as micromoles per minute per milligram of protein (E). Thus, PUDMA samples that had been treated with silicatein/orthosilicate revealed an ALP activity increased by ca. 14 % as compared to the pristine PUDMA control. Furthermore, growth of cells on uncoated P(UDMA-*co*-MPS) carriers caused an increased ALP activity (ca. 35 %) as compared to the pristine PUDMA control. Lastly, the biosilica coating of P(UDMA-*co*-MPS) carriers resulted in a higher ALP activity (ca. 28 %) than compared to the uncoated P(UDMA-*co*-MPS) carriers. These observations corroborate not only the abovementioned ALP staining experiments but also the results of both the qualitative (*via* CLSM) and quantitative (*via* fluoroscopy) assessment of HA formation, clearly demonstrating the osteogenic potential of the biosilica-coated P(UDMA-*co*-MPS) carriers.
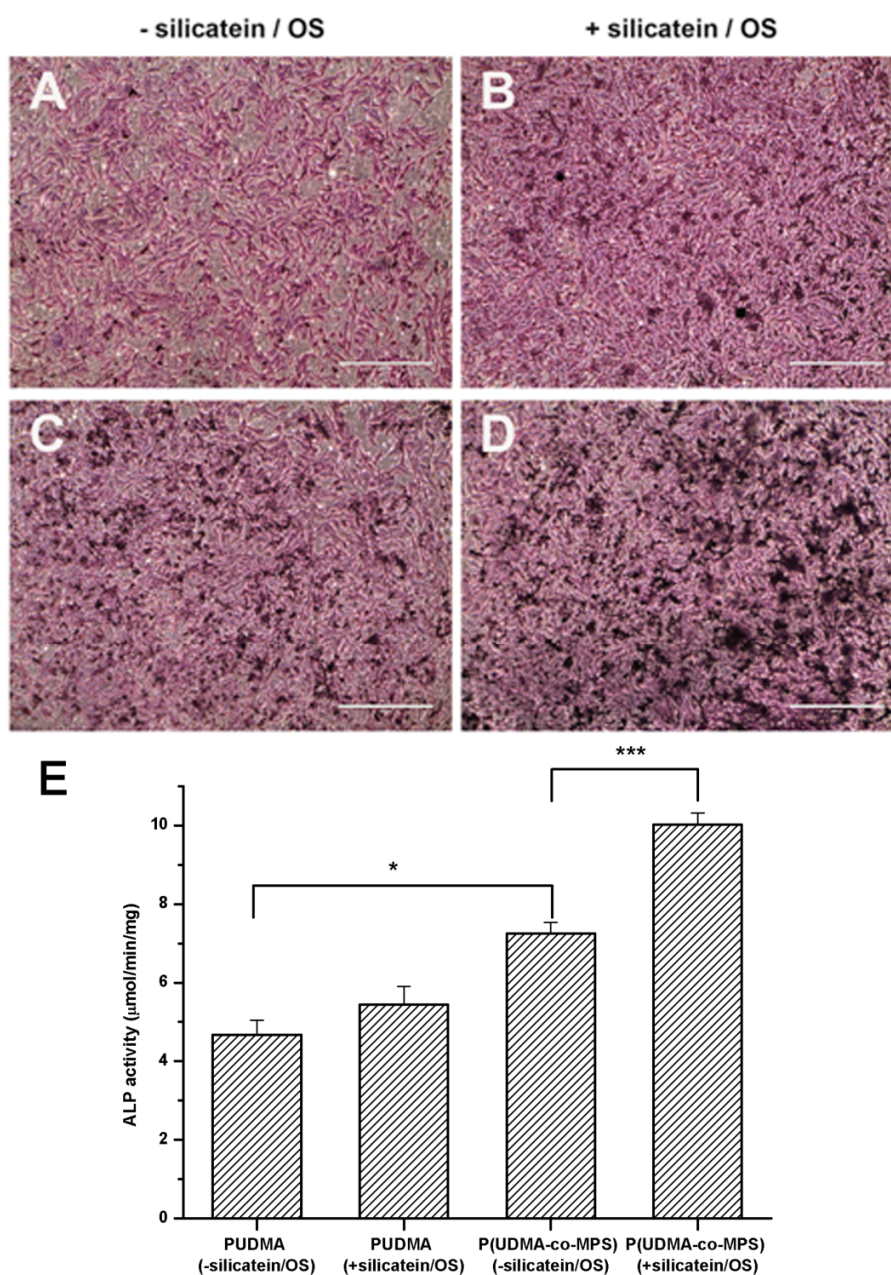
Fig. 4.6 Alkaline phosphatase (ALP) activity of SaOS-2 cells, Cells were grown in DAAG supplemented medium on PUDMA (A, B) or P(UDMA-*co*-MPS) (C, D) carriers. The carriers were untreated (A, C; – silicatein/OS) or had been treated with silicatein and orthosilicate (B, D; + silicatein/OS) prior cell culture. ALP activity was visualized microscopically with a solution containing naphthol AS-BI phosphate and fast red violet LB salt. Cells were counterstained with hematoxylin. Bars, 400 μm. Concurrently, ALP activity was quantified spectrophotometrically through conversion of p-nitrophenyl phosphate to p-nitrophenol (E). Data represent mean ± S.D.

In conclusion, enzymatically controlled surface-functionalization of P(UDMA-*co*-MPS) *via* silicatein and orthosilicate provides access to a composite material that combines the inherent osteogenic potential of a biosilica coating with the bioactivity, hardness, and elastic modulus of the copolymer. This tailored combination of properties might be explored for fabricating advanced materials, which provide structural support and facilitate the formation of stable bone-material interfaces and, consequently, represent an alternative to PUDMA or other acrylics conventionally used in the field of orthopedics and dentistry.

4.4 References

Alexander J.D., Gent A.N. & Henriksen P.N. (1985). Inelastic electron tunneling spectroscopy of silane coupling agents adsorbed on alumina. *The Journal of chemical physics* 83, 5981-5987.

André R., Tahir M.N., Link T., Jochum F.D., Kolb U., Theato P., Berger R., Wiens M., Schröder H.C., Müller W.E.G. & Tremel W. (2011). Chemical Mimicry: Hierarchical 1D TiO2@ ZrO2 Core−Shell Structures Reminiscent of Sponge Spicules by the Synergistic Effect of Silicatein-α and Silintaphin-1. *Langmuir 27*, 5464-5471.

Arcos D. & Vallet-Regí M. (2010). Sol–gel silica-based biomaterials and bone tissue regeneration. *Acta Biomaterialia* 6, 2874-2888.

Barth A. (2007). Infrared spectroscopy of proteins. *Biochimica et Biophysica Acta* 1767, 1073-1101.

Briscoe B.J., Fiori L. & Pelillo E. (1998). Nano-indentation of polymeric surfaces. *Journal of Physics D: Applied Physics* 31, 2395-2405.

Cha J.N., Shimizu K., Zhou Y., Christiansen S.C., Chmelka B.F., Stucky G.D. & Morse D.E. (1999). Silicatein filaments and subunits from a marine sponge direct the polymerization of silica and silicones in vitro. *Proceedings of the National Academy of Sciences 96*, 361-365.

Chang K.C., Chen Y.K. & Chen H. (2007). Preparation of superhydrophobic silica-based films by using polyethylene glycol and tetraethoxysilane. *Journal of applied polymer science* 105, 1503-1510.

Czekanska E.M., Stoddart M.J., Richards R.G. & Hayes J.S. (2012). In search of an osteoblast cell model for *in vitro* research. *European Cells and Materials* 24, 1-17.

Deb S., Aiyathurai L., Roether J.A. & Luklinska Z.B. (2005). Development of high-viscosity, two-paste bioactive bone cements. *Biomaterials* 26, 3713-3718.

Emmons E.D., Kraus R.G., Duvvuri S.S., Thompson J.S. & Covington A.M. (2007). High-pressure infrared absorption spectroscopy of poly (methyl methacrylate). *Journal of Polymer Science Part B: Polymer Physics* 45, 358-367.

Hench L.L. (2006). The story of Bioglass®. *Journal of Materials Science: Materials in Medicine* 17, 967-978.

Jaeblon T. (2010). Polymethylmethacrylate: properties and contemporary uses in orthopaedics. *Journal of the American Academy of Orthopaedic Surgeons* 18, 297-305.

Kanie T., Arikawa H., Fujii K. & Inoue K. (2004). Physical and mechanical properties of PMMA resins containing γ-methacryloxypropyltrimethoxysilane. *Journal of Oral Rehabilitation* 31, 166-171.

Kenny S.M. & Buggy M. (2003). Bone cements and fillers: a review. *Journal of Materials Science: Materials in Medicine* 14, 923-938.

Lee S.H., Teramoto Y., Wang S., Pharr G.M. & Rials T.G. (2007). Nanoindentation of biodegradable cellulose diacetate-graft-poly (L-lactide) copolymers: Effect of molecular composition and thermal aging on mechanical properties. *Journal of Polymer Science Part B: Polymer Physics* 45, 1114-1121.

LeGeros R.Z. (2008). Calcium phosphate-based osteoinductive materials. *Chemical reviews* 108, 4742-4753.

Lewis G. (2011). Viscoelastic properties of injectable bone cements for orthopaedic applications: State-of-the-art review. *Journal of Biomedical Materials Research Part B: Applied Biomaterials* 98, 171-191.

Leyland A. & Matthews A. (2000). On the significance of the *H/E* ratio in wear control: a nanocomposite coating approach to optimised tribological behaviour. *Wear* 246, 1-11.

Müller W.E.G., Boreiko A., Wang X., Krasko A., Geurtsen W., Custódio M.R., Winkler T., Lukić-Bilela L., Link T. & Schröder H.C. (2007). Morphogenetic activity of silica and bio-silica on the expression of genes controlling biomineralization using SaOS-2 cells. *Calcified tissue international* 81, 382-393.

Müller W.E.G., Wang X., Cui F. Z., Jochum K. P., Tremel W., Bill J., Schröder H.C., Natalio F., Schloßmacher U. & Wiens M. (2009). Sponge spicules as blueprints for the biofabrication of inorganic–organic composites and biomaterials. *Applied microbiology and biotechnology* 83, 397-413.

Müller W.E.G., Wang X., Diehl-Seifert B., Kropf K., Schloßmacher U., Lieberwirth I., Glasser G., Wiens M. & Schröder H.C. (2011). Inorganic polymeric phosphate/polyphosphate as an inducer of alkaline phosphatase and a modulator of intracellular Ca^{2+} level in osteoblasts (SaOS-2 cells) in vitro. *Acta biomaterialia* 7, 2661-2671.

Natalio F., Link T., Müller W.E.G., Schröder H.C., Cui F.Z., Wang X. & Wiens M. (2010). Bioengineering of the silica-polymerizing enzyme silicatein-α for a targeted application to hydroxyapatite. *Acta biomaterialia* 6, 3720-3728.

Oliver W.C. & Pharr G.M. (1992). Improved technique for determining hardness and elastic modulus using load and displacement sensing indentation experiments. *Journal of materials research* 7, 1564-1583.

Oudadesse H., Derrien A.C., Martin S., Lucas-Girot A. & Cathelineau G. (2007). Comparison of the bony remodelling of two synthetic biomaterials: aragonite 55% and aragonite 55% with active substance. *Biomedical Materials* 2, S65-S70.

Pantoja M., Díaz-Benito B., Velasco F., Abenojar J. & Del Real J.C. (2009). Analysis of hydrolysis process of γ-methacryloxypropyltrimethoxysilane and its influence on the formation of silane coatings on 6063 aluminum alloy. *Applied Surface Science* 255, 6386-6390.

Rubio F., Rubio J. & Oteo J.L. (1998). A FT-IR study of the hydrolysis of tetraethylorthosilicate (TEOS). *Spectroscopy Letters* 31, 199-219.

Schloßmacher U., Wiens M., Schröder H.C., Wang X., Jochum K.P. & Müller W.E.G. (2011). Silintaphin-1–interaction with silicatein during structure-guiding bio-silica formation. *FEBS Journal* 278, 1145-1155.

Schröder H.C., Wiens M., Schloßmacher U., Brandt D. & Müller W.E.G. (2012). Silicatein-mediated polycondensation of orthosilicic acid: modeling of a catalytic mechanism involving ring formation. *Silicon* 4, 33-38.

Skarmoutsou A., Charitidis C.A., Gnanappa A.K., Tserepi A. & Gogolides E. (2012). Nanomechanical and nanotribological properties of plasma nanotextured superhydrophilic and superhydrophobic polymeric surfaces. *Nanotechnology* 23, 505711.

Sugino A., Miyazaki T. & Ohtsuki C. (2008). Apatite-forming ability of polyglutamic acid hydrogels in a body-simulating environment. *Journal of Materials Science: Materials in Medicine* 19, 2269-2274.

Tsukeoka T., Suzuki M., Ohtsuki C., Sugino A., Tsuneizumi Y., Miyagi J., Kuramoto K. & Moriya H. (2006). Mechanical and histological evaluation of a PMMA-based bone cement modified with γ-methacryloxypropyltrimethoxysilane and calcium acetate. *Biomaterials* 27, 3897-3903.

Van Landuyt K.L., Snauwaert J., De Munck J., Peumans M., Yoshida Y., Poitevin A., Coutinho E., Suzuki K., Lambrechts P. & Van Meerbeek B. (2007). Systematic review of the chemical composition of contemporary dental adhesives. *Biomaterials* 28, 3757-3785.

Wang X., Schloßmacher U., Wiens M., Batel R., Schröder H.C. & Müller W.E.G. (2012). Silicateins, silicatein interactors and cellular interplay in sponge skeletogenesis: formation of glass fiber-like spicules. *FEBS Journal* 279, 1721-1736.

Watanabe S. (1995). In-situ infrared characterization of a chemically oxidized silicon surface dissolving in aqueous hydrofluoric acid. *Surface science* 341, 304-310.

Wiens M., Bausen M., Natalio F., Link T., Schlossmacher U. & Müller W.E.G. (2009). The role of the silicatein-α interactor silintaphin-1 in biomimetic biomineralization. *Biomaterials* 30, 1648-1656

Wiens M., Link T., Elkhooly T.A., Isbert S. & Müller W.E.G. (2012). Formation of a micropatterned titania photocatalyst by microcontact printed silicatein on gold surfaces. *Chemical Communications* 48, 11331-11333.

Wiens M., Wang X., Natalio F., Schröder H.C., Schloßmacher U., Wang S., Korzhev M., Geurtsen W. & Müller W.E.G. (2010 a). Bioinspired Fabrication of Bio-Silica-Based Bone-Substitution Materials. *Advanced Engineering Materials* 12, B438-B450.

Wiens M., Wang X., Schloßmacher U., Lieberwirth I., Glasser G., Ushijima H., Schröder H.C.& Müller W.E.G. (2010 b). Osteogenic potential of biosilica on human osteoblast-like (SaOS-2) cells. *Calcified tissue international* 87, 513-524.

Wiens M., Wang X., Schröder H.C., Kolb U., Schloßmacher U., Ushijima H. & Müller W.E.G. (2010 c). The role of biosilica in the osteoprotegerin/RANKL ratio in human osteoblast-like cells. *Biomaterials* 31, 7716-7725.

Will J., Gerhardt L.C. & Boccaccini A.R. (2012). Bioactive Glass-Based Scaffolds for Bone Tissue Engineering. *Advances in Biochemical Engineering/Biotechnology* 126, 195-226.

Chapter 5

Cellular response on microcrystalline chitosan-polycaprolactone graft immobilized with enzymatically formed biosilica

5.1 Introduction

Amphiphilic polymers are usually designed for bone tissue engineering to overcome the individual deficiencies in each polymer phase. Furthermore, amphiphilic polymers provide moderate wettability on their surfaces which was found favorable for cells adhesion (Arima & Iwata, 2007). Therefore, several methods have been established to combine the properties of both hydrophilic chitosan (CHS) and hydrophobic polycaprolactone (PCL) for biomedical applications by blending using miscible solvents (Sarasam & Madihally, 2005) or one common solvent (Wan et al., 2008), grafting *via* amine (Feng & Dong, 2006) or hydroxyl (Duan et al., 2010) groups of CHS backbone, crosslinking agent (Aroguz et al., 2011), semi-interpenetrating network (García Cruz et al., 2009), electrospinning (Yang et al., 2009) and by using emulsifiers (Zhong et al., 2011). PCL is hydrophobic aliphatic polyester that has been used for decades in biomedical fields such as drug carries, wound dressings, dentistry, and scaffold for tissue engineering, as it has FDA approval (Woodruff & Hutmacher, 2010). However, PCL main disadvantages as scaffolding material involve the (a) absence of cell recognition sites, (b) its inherent hydrophobicity and (c) its relatively slower degradation rate compared to other polyesters ((Woodruff & Hutmacher, 2010; Neves et al., 2011). On the other hand, CHS is polycationic semicrystalline polymer extracted from natural source (e.g. crustacean shells) and has been widely used for decades in different biomedical areas. However, its disadvantages that restrict its usage as scaffold for tissue engineering, are its high swelling index causing loss in CHS scaffolds integrity and its weak mechanical properties in wet state (Dash et al., 2011). Therefore, we attempted to combine both CHS and PCL properties *via* covalent chemical conjugation to overcome the aforementioned disadvantages of both polymers. Chitosan polymorphs

have high content of amine groups at C_2 position of the glucosamine units; therefore, its reactivity for chemical modification is promoted at higher pH value (Dash et al., 2011). However, at alkaline media, chitosan tend to precipitate due to the deprotonation of its amine groups (pKa ~ 6.3), therefore; the morphology and crystallinity of the precipitated chitosan polymorph after its neutralization are highly dependent on the experimental conditions such as pH value, solution temperature, water removal rate, organic solvents, etc. One of precipitated chitosan polymorph is microcrystalline chitosan (MCCS) which was previously prepared by controlling several experimental parameters including neutralization, depolymerization, coagulation, and aggregation of chitosan macromolecules (Struszczyk, 1987). Different morphologies have been reported for MCCS such as oval, spherulites, needle, and sheet like crystals [Struszczyk, 1987; Dong et al., 2002; Lewandowska, 2012). Few studies have been conducted on the applicability of MCCS as an artificial extracellular matrix for bone cells adhesion and proliferation. Despite, it has been proven as biocompatible and active polymorph for sealing arterial puncture sites by providing hemostasis (Hoekstra et al., 1998). Furthermore, MCCS membrane has been suggested recently for bone regeneration due to its high binding efficiency and slow release to transforming growth factor beta-1 (TGF-β1) (Michalska et al., 2013). MCCS was shown to be easily biodegradable in aqueous solution at room temperature, however, the degradation rate accelerated by increasing the temperature and the presence of microorganisms (Struszczyk et al., 2003). Osteogenesis, osteoinduction, and osteoconduction are essential requirements for the success of bone regeneration (Murugan & Ramakrishna, 2005). Osteoconductive grafts are mostly used to serve as a scaffold through which the host bone infiltrate and regenerate a new bone tissue. Most of the synthetic bone grafts such as polymer scaffold acquires osteoconductivity by depositing hydroxyapatite acellularly for direct bonding with host bone. However, inducement of cellular differentiation and mineralization by regulating the signal transduction cascade of bone cells is highly desirable for providing an osteogenic and osteoinductive grafts. Scaffolds loaded with growth factor have regulated cellular growth and related functions in a better way (Wilson et al., 2005). However, due to the expense and short life time of these cytokines, some inorganic particles could be used alternatively to stimulate bone

forming cells precursors for osteogenic properties. Silica particles formed by sol-gel chemistry and biosilica formed enzymatically by silicatein have been used extensively to regulate osteoblast morphogenesis (Beck Jr et al., 2012; Wiens et al., 2010; Müller et al., 2007). Therefore, the immobilization of silica nanoparticles on polymeric surfaces might provide inductive interface for better cellular response (Lipski et al., 2008). In this chapter, we grafted PCL onto CHS backbone by using amine coupling agent DCC/NHS at slightly alkaline pH, the resultant graft composed of shapeable MCCS-PCL that has been molded into membranes for studying the interaction of osteoblast like cells SaOS-2 on their surface. Furthermore, PCL fraction in the membranes was aminolyzed with diamine to enrich the surface with ionized amines for ionic binding with silicatein, which subsequently mediate the polycondensation of biosilica in order to enhance the cellular osteogenicity of the polymer surface.
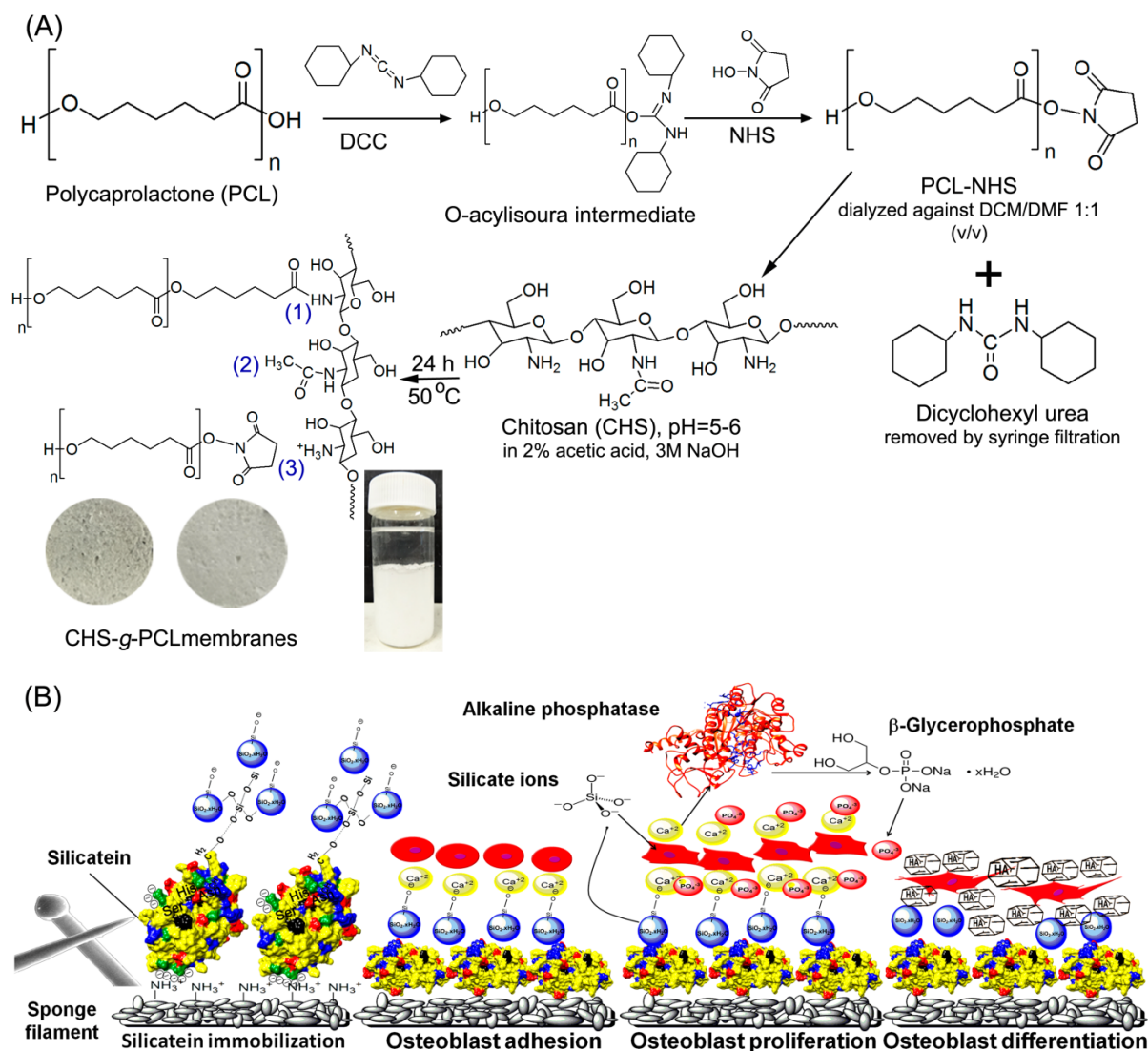
Scheme 5.1 represents the synthetic route of CHS-*g*-PCL amphiphilic polymer (A) and the suggested cellular response to its surface after functionalizing with silicatein and biosilica (B). (A) Polycaprolactone (PCL) carboxylic terminus are initially activated with N,N'-Dicyclohexylcarbodiimide (DCC) which then stabilized by N-Hydroxysuccinimide (NHS) forming polycaprolactone succinimide ester (PCL-NHS), after removal of insoluble by-product dicyclohexylurea, The activated PCL-NHS is added to chitosan (CHS) solution dissolved in acetic acid/sodium hydroxide solution (pH 5-6) and the reaction between the two polymer is conducted for 24 h at 40°C. Stable secondary amide bond is formed only between PCL-NHS and the deprotonated amine groups of the chitosan backbone (1), while, acetamide (2) and protonated amines (3) groups in chitosan backbone remain unreacted. (B) Recombinant silicatein-α expressed in *E. Coli* based on its encoded gene identified in the axial filament of *Suberites domuncula* spicules. Recombinant silicatein-α molecules are ionically bounded to the CHS-*g*-PCL surface enriched with

protonated amines originated from chitosan backbone or introduced to the carbonyl group of PCL fractions by PCL aminolysis. The bounded enzyme mediates the biopolycondensation of biosilica from orthosilicic acid soluble precursor. The surface functionalized biosilica accelerate the osteoblasts differentiation thereby upregulating the secretion of the membrane bounded alkaline phosphatase (ALP). ALP cleaves β-glycerophosphate resulting in higher concentrations of inorganic phosphate ions which react with the interfacial calcium ions forming amorphous calcium phosphate which rapidly crystallize on biosilica into hexagonal bone-like hydroxyapatite.

5.2 Experimental section

5.2.1 Fabrication of chitosan-polycaprolactone graft

The carboxylic end groups of the aliphatic polyester poly-ε-caprolactone (PCL, Aldrich, 70-90 KDa) were activated by N,N'-Dicyclohexylcarbodiimide (DCC, Fluka) and N-Hydroxysuccinimide (NHS, Aldrich) for direct conjugation with chitosan (CHS, 140-220 KDa, DD 93%, Aldrich) by amidation reaction. The number of PCL chains per chitosan glucosamine units was calculated by changing the molar feed ratios of PCL to CHS to be 9 %. Shortly, 2% chitosan solution was prepared by dissolving in 2% (v/v) acetic acid in a glass beaker with moderate stirring for 30 hrs to ensure the complete dissolution of chitosan, thereafter; the viscous chitosan solution was centrifuged at 5,000 rpm, 40°C for 1 h. The pH of the supernatant was adjusted with 3M NaOH to 5.5-6 near the pK$_a$ value of chitosan (~ 6.3) at which 50% of its amine groups are deprotonated (Dash et al., 2011). The deprotonation of chitosan amine groups is essential step to improve the efficiency of conjugation, because of the activated succinimide ester reacts with primary amines at physiologic to slightly alkaline conditions (pH 7.2 to 9) to yield stable secondary amide bonds (Brinkley, 1992). PCL (2 gm) were dissolved in 50 ml of 50:50 % (v/v) DMF/DCM, after complete dissolution of PCL, 10 equivalents of both DCC (0.52 g, 2.5 mmol) and NHS (0.03 g, 2.5 mmol) were co-dissolved with PCL. The activation reaction of the carboxylic end group of PCL with NHS by using DCC as catalysis was accomplished for 12 h at room temperature. The insoluble by-product of this reaction dicyclohexylurea was removed by centrifugation (10 min, 5000 rpm, 15°C), subsequently filtrated using 0.45 μm PTFE membrane syringe filter. To ensure the

complete removal of the excess of DCC/NHS coupling reagents, the activated PCL solution was dialyzed against 10 fold volume of DMF/DCM using 10 KDa cutoff dialysis membrane for 1 day. Excess of activated PCL (PCL-NHS) solution was added into 50 ml of CHS solution (pH= 5.5-6) and stirred for 24 h at 50°C. The obtained shapeable gummy-like material was washed by immersing it in tetrahydrofuran (THF), 30% ethanol and 30% isopropanol and molded between two glass plates to form thin membrane by slight pressing. The membrane was dried under vacuum and then cut into circular shapes with the same diameter of 48 cell culture well plates (10 mm) (Greiner Bio-One, Frickenhausen, Germany). Scheme 5.1 shows the chemical reaction and the shape of the resultant CHS-*g*-PCL polymer for the obtained bulk and the molded membranes.

5.2.2 *In vitro* degradation and swelling index

Dry cubic specimens (50±10 mg, ~ 30 mm^2, n=3) were immersed in phosphate buffered saline (PBS) solution (0.2 M, pH 7.4, 0.05 wt% NaN$_3$) or an enzymatic solution at 37°C in a reciprocal shaking incubator at 60 rpm to examine their degradation according to previously described method (Wan et al., 2008; Castilla-Cortázar et al., 2012). Enzymatic degradation was performed by incubating CHS-*g*-PCL specimens with 1 mg/ml lysozyme from chicken egg white (Sigma) for targeting chitosan glycosidic bonds and 1 mg/ml Lipase from Pseudomonas sp. (Sigma) for targeting PCL ester bonds. Both enzymes were prepared in 0.2 M PBS containing 0.05 wt% of sodium azide for bacterial infection. The weight loss percentage was calculated for different time intervals (1, 2, 3 and 4 weeks) by formula published previously (Wan et al., 2008). The remaining polymer for 1 month samples were centrifuged and then washed several times with deionized water, subsequently their ATR-FTIR spectra were recorded on a Varian 660-IR spectrometer. Furthermore, the swelling index (SI) was employed for evaluating the water absorption capacity of grafted polymer. SI was calculated after immersion in PBS for 1, 2, 3 and 4 weeks. The mass of the swollen samples was measured after removal of the surface water with filter paper. SI of cubic samples was calculated by previously published equation (Castilla-Cortázar et al., 2012).

5.2.3 Surface functionalization of the grafted polymer (Surface aminolysis)

Targeting chitosan amine groups by conjugation with PCL-NHS is expected to decrease the electrostatic binding of the grafted polymer due to the formation of stable secondary amide bond. Therefore, to increase the amine density onto CHS-g-PCL membranes, aminolysis reaction via nucleophilic attack of diamine compounds at the carbonyl of PCL ester groups was previously recommended for functionalization of PCL polymer to enhance the biomacromolecules immobilization including even chitosan (Mattanavee et al., 2009). For this reason, CHS-g-PCL grafted membranes were immersed in an ethanolic aqueous solution 1:1 (v/v) for 2-3 h to cleanse the surface and then washed with water. Subsequently, 10 wt% 1,6-hexamethylenediamine (HMD, Aldrich) were dissolved in isopropanol solutions and then used to aminolyze the membranes surface for 3 h at 37 °C in the shaker at 120 rpm. The aminolyzed specimens were then rinsed with deionized water for 24 h at RT to remove unreacted HMD and dried under vacuum at 30 °C until of a constant weight.

5.2.4 Silicatein immobilization and biosilica formation

The aminolyzed CHS-g-PCL membranes were treated in 20 mM HCl solution for 30 min at RT and washed with a large amount of water to ensure the protonation of amine groups prior to silicatein immobilization. 500 µg/ml of lyophilized recombinant mature silicatein-α (aa$_{115-330}$) folded as previously described in chapter 3 were dissolved in Tris/HCl buffer (pH 7.5). The isoelectric point of silicatein is around 5 (Murr. & Morse, 2005), accordingly at neutral pH, the protein acquires negatively charged surface for direct binding with protonated amine groups on CHS-g-PCL surface. The functionalized protonated membranes were incubated with silicatein solution at RT for 2 h with gentle agitation. Afterwards, the samples were washed with deionized water and the supernatants were collected for protein concentration assay. In order to coat the membranes with biosilica, the membranes immobilized with silicatein-α were immersed into pre-hydrolyzed tetraethyl orthosilicate (1 mM, TEOS, Aldrich) solution in 50 mM Tris/HCl buffer (pH 7.4, 37°C) (Schröder et al., 2005). The membranes were washed

three times with deionized water and lyophilized overnight at 75°C, <100 mTorr, thereafter, the membranes were stored at 4°C for further use.

5.2.5 Characterization of the immobilized silicatein

After silicatein immobilization, the protein concentration in the supernatants was estimated using Bradford analysis (Roti-Quant solution, Roth, Karlsruhe; Germany) for the remaining unbound silicatein. Otherwise, for silicatein immunodetection on CHS-*g*-PCL membranes, specific anti-silicatein polyclonal antibody (PoAb-aAQP_SUBDO) was used as described before (Wiens et al., 2013). Shortly, the membranes immobilized with silicatein were initially blocked [10% v/w blocking solution (PBS/BSA)] for 1h at RT. After washing with TBS-T [(Tris-buffered saline), pH 7.5 + 0.05% Tween®-20], primary anti-silicatein antibody (1:1,000 dilution in PBS/BSA 10% v/w) was incubated for 1 h at RT. Subsequently, the membranes were washed three times with TBS-T for 5 min each, and incubated with Cy-3 conjugated goat anti-rabbit IgG (1:2,000 dilution, PBS/BSA 10% v/w) for 1 h at RT. Thereafter, the surfaces were washed with TBS-T/TBS and analyzed by a Zeiss 710 CLSM (Carl Zeiss GmbH, Göttingen, Germany), using the 543 nm line of the argon laser. Furthermore, the distribution of immobilized protein on the CHS-*g*-PCL membranes was visualized by protein specific comassie blue reagent. The samples were incubated with EZblue gel staining (sigma) for 10 min at RT, thereafter, washed five times with water as was described before (Natalio et al., 2010). After drying, the surfaces were photographed using VHX-1000 keyence digital microscope.

5.2.6 Further characterization techniques

Attenuated total reflection Fourier transforms infrared spectroscopy (ATR-FTIR) spectra of each sample were generated by Varian 660-IR spectrometer. The spectra were obtained by accumulating 36 scans in the range of 550–4000 cm^{-1} with a resolution of 4 cm^{-1}. The crystallinity of CHS-*g*-PCL polymer membranes were then characterized by Philips X'pert MPD diffractometer using Cu Ka generated at 40 KV and 40 mA and scanned from 10 to 90° with a step size of 0.02^o and a count rate of 3.0^o/min. Thermal stability measurements were performed using a TA- Instrument Model Q 5000 system in nitrogen environment. TGA test was performed in alumina crucibles where samples (5–

10 mg weight) were placed on the balance and the temperature rose from room temperature to 800°C at a heating rate of 10 $^{\circ}$C/min. The mass of the sample pan was continuously monitored as a function of temperature. Contact angle measurement was applied to determine the change in surface Wettability for CHS-*g*-PCL polymer, aminolyzed surface, after immobilization of silicatein alone and silicatein/biosilica. For static water contact angle measurements, digital images of a water droplet (5 μl) on the investigated surfaces were taken using a UK1117 camera (EHD imaging GmbH, Germany) and analyzed by using Northern Eclipse software. The presented values were the average of three measurements for different samples. The thickness and the morphology of immobilized silicatein on grafted polymer surface was measured by a MFP-3D BioAFM (Asylum, Mannheim) in AC mode using a commercial Si_3N_4 cantilever with a spring constant of 7.5 N/m (μMasch) in air. The AFM was used in a closed loop operation mode on all three axes with the tip scanning back and forth at 0° along the horizontal line in the range of 80 μm. Obtained topographic images were evaluated with the corresponding software IGOR. For further morphological assessments, the samples under investigation were placed on carbon stubs and sputtered with palladium-gold. The morphology of the samples was observed by Philips XL30 field-emission environmental scanning electron microscope (Philips XL30 ESEM-FEG). Elemental analyses were performed using the energy dispersive X-ray fluorescence spectroscopic unit (EDX) with a liquid nitrogen cooled Sapphire Si(Li) detector. For the spectra collection, the microscope was operated a 100 μm aperture, concurrently, selected image area was scanned.

5.2.7 SaOS-2 cells incubation conditions

The human osteogenic sarcoma cells (SaOS-2 cells line (Pautke et al., 2004)) were cultured in McCoy's medium with 26.19 mM $NaHCO_3$ (Biochrom, Berlin) supplemented with 15% heat-inactivated FCS, 2 mM L-glutamine, and 50 μg/ml gentamicin in 25-cm^2 flasks (Orange Scientifique, Braine-l'Alleud, Belgium) in a humidified incubator at 37°C and 5% CO_2 as described previously (Wiens et al., 2013).

For all cell culture experiments, freshly thawed cells were seeded on the membrane specimens (10 mm in diameter x 0.5 mm in thickness) in 48 well plate (Greiner Bio-One, Frickenhausen, Germany) at a density of 50 000 cells/ml (1 ml) at 37°C for different time intervals in the medium described above. The samples were sterilized with 70% ethanol and then exposed for 1 h to laminar hood UV light prior to cell seeding. For the samples immobilized with silicatein, the membranes were sterilized after functionalizing their surfaces with HMD. Thereafter, the immobilization and biosilica formation procedures were performed under aseptic conditions.

5.2.7.1 Cell viability/growth test

Cell growth and cytotoxicity was determined using MTT reagent (Sigma), as an indirect marker for viable cells which are able to cleave the yellow tetrazolium salt MTT to produce purple formazan crystals and can be measured by spectrophotometer after crystals dissolution. The level of the reduction of MTT by mitochondrial succinate dehydrogenase into formazan crystals is equivalent to the level of viable cell metabolism. At certain culture times, 900 μL of pre-warmed McCoy's medium without fetal calf serum (FCS) and 100 μL of MTT stock solution (5 mg/mL in PBS) were added to each sample and incubated for 4 h at 37°C under humidified atmosphere. The medium was then aspirated and the precipitated formazan crystals on the material surfaces were dissolved in 1 ml of anhydrous dimethyl sulfoxide (DMSO, Sigma-Aldrich) for 60 min. Afterwards, 200 μL (in triplicate) of formazan solution were transferred from each well to a 96-well flat-bottom plate, and the absorbance was determined at 570 nm using Varioskan plate reader (Thermo Fisher). Controls without cells were carried out to subtract the color produced by non- biological processes.

5.2.7.2 Immunocytochemistry with silicatein antibody

To visualize the cell adhered on silicatein immobilized surface after 3 and 7 days of cell culture, both silicatein and cellular nuclei were stained with fluorescent dyes and visualized by confocal laser microscope and bright fluorescence microscope. Shortly, the cells were fixed in 4% (w/v) paraformaldehyde (PFA, Sigma-Aldrich) and then

blocked with 5% blocking solution+ 0.1% Triton x-100 diluted in Dulbecco's phosphate buffer saline (DBPS, Gibco® life technologies) for 1 h at RT with shaking. The membranes immobilized only with silicatein were incubated with silicatein primary antibody (PoAb-aAQP_SUBDO) produced in rabbits at a dilution of 1:1000 in blocking solution while shaking at 4°C for overnight. After washing with DPBS-T (0.1% Tween-20) twice, 5 min each, the membranes were incubated with the 2nd silicatein antibody conjugated with Cy3 diluted 1:2000 in blocking solution for 1 h with shaking. Afterwards, the cell nuclei were stained with 10 μM deep red fluorescing agent DRAQ5 (Biostatus Ltd., Shepshed, UK). As control, the 1st and 2nd antibodies were incubated with grafted polymer membranes that haven't been immobilized with silicatein for detection of any non-specific binding. In addition to EVOS fluorescence microscope, high magnification images were inspected by CLSM using argon laser with excitations 543 nm and 633 nm for Cy3-labeled specific secondary antibodies and for the blue-stained nuclei (DRAQ5), respectively.

5.2.7.3 Mineralization analysis and bone nodule visualization

Quantitative and qualitative investigations of the mineral deposited by SaOS-2 cells on different surfaces were accomplished by Alizarin red S (AR-S, Sigma) and Osteoimage fluorescent dye (Lonza, Cologne, Germany). The difference between two staining procedures is that osteoimage binds to hydroxyapatite phase specifically; however, anthraquinone dyes (AR-S) form a complex with the calcium of any calcium phosphate phases (Langenbach et al., 2011). SaOS-2 cells were cultured on each membrane and empty TCPS for 3 days until 70-75% confluence, and then the growth of the cells was stopped by adding osteogenic medium consists of 10 nM dexamethasone (DEX), 50 µM ascorbic acid (AA), and 5 mM β-glycerophosphate (β-GP) to culture medium to promote the ECM mineralization for 7 days as previously described (Wiens et al., 2013). After cell fixation with 4% PFA, 500 µL of 1% AR-S solution prepared in 1:100 (v/v) ammonium hydroxide/water mixtures were added to the membranes and empty well for 30 min with shaking. After complete removal of the AR-S stain, the specimens were rinsed extensively with deionized water tell the disappearance of the red color in the supernatant. Thereafter, the membranes surface were photographed with keyence

VHX-1000 digital microscope, the intensity of red stain was quantitatively assessed by dissolving calcium-bound AR-S complex in 10% hexadecylpyridinium chloride monohydrate (HDPC; Fluka) prepared in sodium phosphate buffer (10 mM, pH 7.0) for 1 h. The absorbance of the resulting deep blue solution was measured at 562 nm and the corresponding concentration of bound ARS was determined for each sample after generating a calibration curve from different concentrations of AR-S in HDPC (2000-3.75 μM). For osteoimage mineralization assay, the F-actin filaments of the cytoskeleton, cell nuclei, and hydroxyapatite nodules were stained with Rhodamine phalloidin (Life Technologies, Darmstadt, Germany), DRAQ5, and osteoimage, respectively, according to the manufacturers' instructions. Briefly, cells on membranes surfaces were washed three times with PBS, fixed in 4% [w/v] paraformaldehyde (30 min, RT), and permeabilized with 0.2 % (v/v) Triton X-100 (5 min, RT). Then, cells were blocked with 1 % (v/v) bovine serum albumin (in PBS; 30 min). Thereafter, cells were incubated for 30 min with Rhodamine Phalloidin (100 nM in DPBS) and then DRAQ5 (10 μM in DPBS) for 10 min. The micrographs were inspected by CLSM and fluorescence microscope (AMG EVOSfl).

5.2.7.4 Alkaline phosphatase (ALP) analysis

SaOS-2 cells were cultured on investigated surfaces tissue culture polystyrene plates (TCPS) for 4 and 10 days in normal medium and 10 days in osteogenic medium to evaluate ALP activity. Each membrane in 48 well plates was rinsed with PBS after removal of the culture medium. Alkaline lysis buffer (10 mM Tris-HCl, 1 mM MgCl$_2$, 0.1% (v/v) Triton-X100, pH 10) was added, and then the membranes were exposed to three freeze-thawing cycles (at -80 °C and 37 °C) to ensure complete removal of the cellular component. The supernatants were collected after centrifugation and used to determine both total protein concentrations (QuantiPro BCA Protein Assay Kit, Sigma-Aldrich) and ALP activity. ALP activity was measured using a colorimetric assay (pNPP; SIGMAFAST p-nitrophenyl phosphate tablets, Sigma-Aldrich) according to the manufacturer instructions, which quantified the conversion of p-nitrophenol phosphate (pNPP) to yellow p-nitrophenol (pNP) by ALP enzyme. Briefly, 5 μl of the cell lysate and

200 µl of the assay buffer solution of 5 mM pNPP were added together to a 96-well plate. After 1 hours of incubation, the reaction was stopped by adding 50 µl of 3M NaOH and then the absorbance was read at 405 nm in a microplate reader (Varioskan, Thermo Fisher). A standard curve was made from standards (0–200 µM) prepared with a pNPP (Aldrich) solution. The amount of converted pNP for each sample in triplicates were determined from the standard curve and normalized by the total protein content in the cell lysate. Furthermore, the membrane bounded ALP on the membrane surface was qualitatively visualized by using an ALP staining kit (leukocyte alkaline phosphatase kit, Sigma-Aldrich, Taufkirchen, Germany). After cell fixation in 4% PFA, they were incubated in the ALP staining solution (containing naphthol AS-BI phosphate and fast red violet LB salt) for 15 min (RT), and counterstained with hematoxylin for 2 min, according to the manufacturer's protocol. The stained ALP was visualized by phase contrast microscopy (EVOS XL, Life Technologies).

5.2.7.5 Cells dehydration and morphological studies by SEM

For scanning electron microscopy, the membranes seeded with SaOS-2 cells for 4 days were washed with DPBS trice and fixed 4% PFA in PBS for 30 minutes at RT. Post-fixation was performed in 1% osmium tetroxide (Sigma) in DPBS, and then the membranes were dehydrated in ethanol solution of varying concentrations (i.e., 50, 70, 80, 95, and 100%, respectively) for ~10 min at each concentration. Thereafter, the membranes were dried in ethanol (EtOH) / hexamethyldisilazane (HMDS, Aldrich) mixture with different ratio (EtOH:HMDS: 1:1,1:3 and 100% HMDS) for ~ 15 min at each concentration, the specimens were coated with palladium gold and examined with the use of Philips XL30 ESEM-FEG at voltage of 20 kV.

5.2.8 Samples abbreviation

Hereinafter, polycaprolactone, chitosan, CHS-*g*-PCL polymer, CHS-*g*-PCL functionalization with diamine, CHS-*g*-PCL immobilized ionically with protein (silicatein), and CHS-*g*-PCL immobilized with silicatein and afterwards incubated with pre-

hydrolyzed TEOS for biosilica formation will be referred to as PCL, CS, CP, CPNH, CPP, and CPPS, respectively.

5.2.9 Statistics

Statistical analysis was performed using the Student's t-test with a minimal confidence level of 0.05 for statistical significance. Each experiment was repeated at least three times with a minimum of 3 samples per termination point. Statistically significant differences (*$p < 0.05$ or **$p < 0.005$ or ***$p < 0.001$) were indicated in the figures.

5.3 Results and discussion

5.3.1 Structural analyses of CHS-*g*-PCL polymer
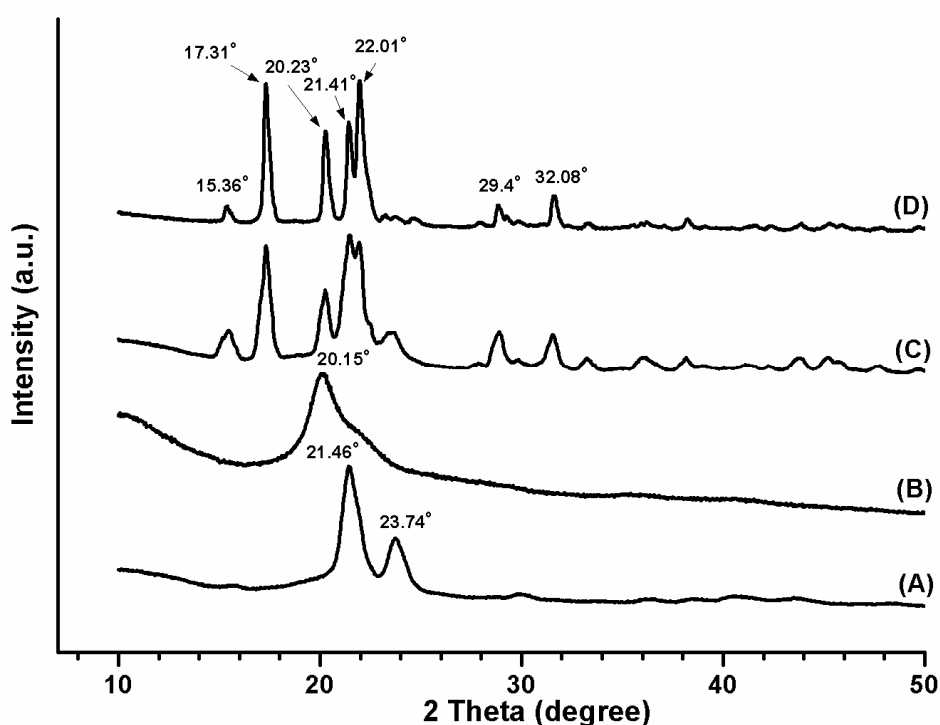
Fig 5.1 X-ray diffraction patterns of grafted CS-*g*-PCL polymer compared to the pristine polymers. (A) PCL membrane, (B) chitosan powder, (C) CS-*g*-PCL polymer membrane (CP), and (D) CP treated with lipase for 1 month (CPL).

The crystallographic structures of CHS, PCL, and CHS-*g*-PCL polymers were determined by XRD, as presented in Fig. 5.1 For the pristine PCL (Fig. 5.1A), two distinct diffraction peaks are observable for its orthorhombic crystalline structures at 2Θ= 21.46^{o} and 2Θ= 23.74^{o} and indexed as 110 and 200 diffraction planes, respectively (Castilla-Cortázar et al., 2012). Moreover, the diffraction pattern of the pristine chitosan powder (Fig. 5.1B) showed only one board peak at 2Θ of 20.15° which is related to hydrated crystal (form II) in the highly deacetylated chitosan (Ren et al., 2005; Zhang et al., 2005). Several sharp new peaks appeared at 2Θ of 15.36, 17.31, 20.23, 21.41, 22.01, 23.74, 29.4, and 32.08^{o} (Fig 5.1C), indicating that the crystallization of chitosan is promoted after conjugation of CHS with PCL-NHS. The same experimental procedures were carried out in the absence of PCL-NHS by mixing chitosan solution (2% in acetic acid, pH 5.5) with DCM/DMF (1/1) mixture at 50°C overnight and no crystallites of chitosan were observed. The chitosan crystalline phase was extracted of by hydrolyzing the PCL phase enzymatically using lipase for different time intervals; enzymatic degradation will be discussed later. XRD pattern of the sample treated with lipase for one month (CPL) showed decrease in both 200 and 110 diffraction planes of PCL segments which might be due to the degradation of the ester linkage in PCL backbone. The peak at 21.41^{o} might be assigned to the remaining hydrocarbon chains attached covalently to chitosan crystal via secondary amide bond (Fig 5.1D). After removal of PCL from the grafted polymer, the assignment of the remaining peaks at 2Θ= 20.23 and 22.01^{o} might be related to hydrated crystalline chitosan (Ogawa, 1991), however, the peak around 21.41^{o} can be ascribed to PCL backbone. Furthermore, the rise of the sharp peak at 2Θ= 17.31^{o} might be related to the formation of organized structure due to the formation of amide linkage between free deprotonated amine groups and succinimide ester attached to the PCL terminus. Similarly, the appearance of new diffraction peaks and increase in chitosan crystallinity were shown to be affected by the different crosslinking bonds with chitosan amine groups (Kumbar et al., 2002) or with chitosan N-acylation with long acyl chain (Le Tien et al., 2003). Finally, the detection of less intense peak at 2Θ=15.36° might be related to the formation of small quantity of anhydrous chitosan polymorph with the hydrated one as has been suggested by Ogawa (Ogawa, 1991).
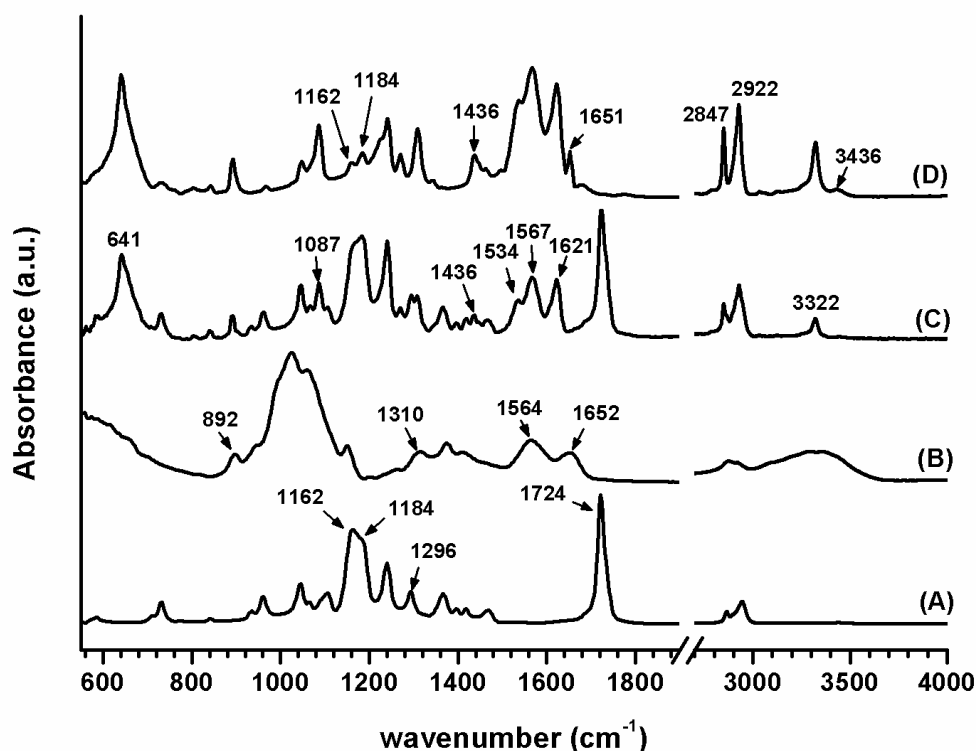
Fig. 5.2 ATR-FTIR absorbance spectra for detection of surface functional groups due to polymers grafting and enzymatic degradation, (A) pure PCL casted membrane, (B) CHS casted membrane, (C) CHS-*g*-PCL grafted polymer (CP), (D) CP treated with lipase for 1 month.

The generation of new functionality through covalent grafting and the influences of both grafting and enzymatic degradation on the polymers function groups were examined using ATR-FTIR (Fig. 5.2), which gives molecular vibrations about the top 1–5 μm of the material. PCL and CHS cross-linking using DCC/NHS linker involves the activation of the terminal carboxylic groups of the PCL, followed by the formation of secondary amide bonds (O=C–NH) between PCL and CHS. For this reason, secondary amide bands were detected at 3322 (N–H str.), 1621 (–C=O str.), 1567 (–N–H bending), 641 cm^{-1} (N–H wagging) in CP spectrum (Fig. 5.2C) (Hendra et al., 1990). Furthermore, the characteristic amide I bands of pristine chitosan for carbonyl stretching at 1652 cm^{-1} was shifted to lower frequency at 1621 cm^{-1} which indicates the formation of new amide bond as a resultant of chemical conjugation (Bhattarai et al., 2007). Moreover, significant decrease in β-(1,4)-glycosidic linkage (C–O–C stretching) band intensities in

range of 890–1150 cm^{-1} due to elevated reaction temperature (50°C) which might causing cleavage of glycosidic bonds between chitosan chains and subsequently forming low molecular weight chitosan (Kittur et al., 2003). These shorter chitosan chains are undergoing recrystallization at neutral pH forming one of the chitosan derivatives termed as microcrystalline chitosan (MCCh) (Struszczyk, 1987; Qin et al., 2004; Pighinelli & Kucharska, 2013). Glycosidic peaks characteristic for polysaccharides are detected at 896 and 1087 cm^{-1} in all spectra except for pure PCL spectrum. To enhance the reactivity between activated NHS esters at PCL terminals and chitosan glucosamine units, deprotonation of amine groups is strongly required at neutral or slightly alkaline environment. It has been reported that the complete deprotonation of chitosan amine groups occurs at pH value above 10 (Boddu et al., 2003), however, at this pH, NHS ester at PCL terminus might hydrolyze lowering the reaction yield. In the current study, the conjugation reaction was achieved at pH 7-8, therefore, the glucosamine units of chitosan are partially protonated and they might not be suitable for coupling with PCL-NHS resulting in an additional shoulder at 1534 cm^{-1} (Fig. 5.2C) assigned to the symmetric –NH$_3^+$ deformation mode (Pearson et al., 1960). On the other hand, several characteristic bands for pristine PCL ester (–CO–O–C–) vibrations (Fig. 5.2A) are located at 1724 (–C=O str.), 1296 (–C–O str. in crystalline phase), 1184 (–OC–O– str.) and broad band at 1162 cm^{-1} (–C–O str. in amorphous phase and Symmetric –COC– stretching) (Elzein et al., 2004). These bands remain unaffected in CHS-g-PCL spectrum (Fig. 5.2C). However, reversal of the absorbance band intensities at 1184 and 1162 cm^{-1} was observed, probably due to the partial degradation of PCL chains by NaOH initially added to the soluble CHS solution for deprotonation of its amine groups. Similar behavior was observed after treating the surface of PCL plates with NaOH solution to generate carboxylate groups in order to enhance the PCL ability to deposit biomineral (Oyane et al., 2005). The alkaline and enzymatic cleavage of PCL ester groups produces shorter chains with carboxylic acid and alcohol terminal groups. Accordingly, the absorbance band at 1436 cm^{-1} (C–O–H in-plane bending) due to carboxylic acid (Stuart, 2004) was detected in CP spectrum (Fig. 5.2C) and further increase in its intensity was detected in lipase treated graft (Fig. 5.2D) due to hydrolysis of PCL fraction in CHS-g-PCL. The effect of ester specific lipase enzyme can be clearly

seen in spectrum (Fig 5.2D) due to the disappearance of all aforementioned ester bands of PCL, concurrently, new peaks appeared at 1651 and 3436 cm^{-1} due to carboxylic (–C=O H-bonded) and hydroxyl (–OH str.), respectively (Stuart, 2004). Finally, the higher intensities of CH- vibration bands at 2922 and 2847 cm^{-1} (Fig 5.2 C and D) compared to the pristine polymers (Fig 5.2 A and B) clearly indicate the coexistence of two polymers hydrocarbon backbone.

5.3.2 Thermal, hydrolytic and enzymatic degradations of CHS-*g*-PCL polymer

Thermogravimetric analyses (TGA) of CP compared to the pristine CHS powder and PCL pellet were carried out to evaluate their degradation profiles, composition ratio, and thermal stability upon grafting. The thermogram of pristine chitosan (Fig. 5.3A, dashed line) exhibited two degradation steps, the first one is located in the range of 10-100°C with maximum DTG peak at 61°C due to the loss of bonded water in chitosan. The second stage started at 250°C with maximum peak around 298°C attributed previously to dehydration, depolymerization and decomposition of the saccharide units in chitosan backbone (García Cruz et al., 2009). PCL thermogram (Fig. 5.3A, solid line) exhibits one stage of degradation from 370 to 467°C with a maximum degradation temperature (Fig 5.3B) at 412°C which is ascribed to PCL chain scissions (García Cruz et al., 2009). The TG/DTG curves of CHS-*g*-PCL (Fig. 5.3 A and B, dotted line) exhibited two distinctive stages of degradation related to two immiscible phases: chitosan phase in sample CP appeared to be less thermally stable than the pristine CS, starting to decompose first in range of 160–260°C with a maximum around 240°C. This behaviour has been observed in the thermogram of depolymerized crystalline chitosan (Qin et al., 2004) or PCL grafted onto chitosan amine groups (Feng & Dong, 2006). In this study, the low thermal stability of CP polymer might be related to the increase of chitosan crystallinity (Fig. 5.1C) due to the depolymerization of chitosan at elevated reaction temperature followed by recrystalization of shorter chitosan chains. Moreover, PCL phase in the grafted polymer showed earlier thermal decomposition started from 350°C to 467°C with shifted maximum peak at 400°C compared to PCL thermogram. The

thermal analysis suggests that the majority ~ 85 wt% of the polymer matrix consists of microcrystalline chitosan, however, PCL contributed only 15 wt% of the total weight.
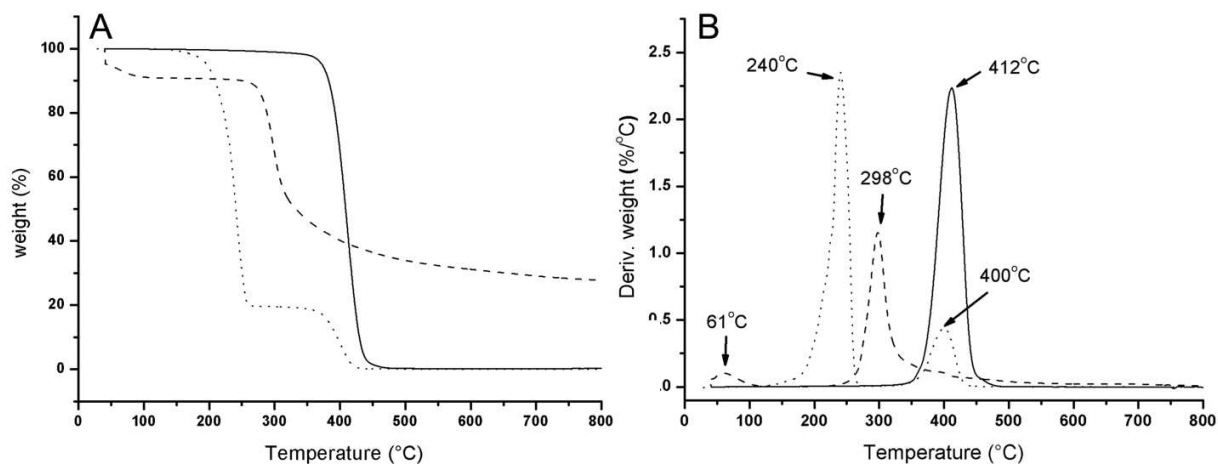

Fig 5.3 Thermogravimetric (TGA) and differential thermogravimetric (DTG) analyses of chitosan, polycaprolactone and grafted polymer, (A) TGA thermograms obtained for PCL (solid line), CHS (dashed line) and, CP (dotted line) (B) The derivative of the TGA trace (DTG) for PCL (solid line), CHS (dashed line) and, CP (dotted line).

On the other hand, the hydrolytic and enzymatic degradation of CHS-*g*-PCL polymer were investigated. After one week of incubation with lipase, turbidity in the PBS buffer was observed and the weight loss of both bulk material and the floating materials was calculated about 13±0.6%. The dissociation CHS-*g*-PCL specimens upon treatment with lipase might indicate that the CHS crystals are interconnected with PCL chains. There were no statistically differences in the weight loss after incubation for 2, 3 and 4 weeks due to the inability of lipase to degrade chitosan crystals and the complete dissociation of PCL chains after 1 week of incubation. On the other hand, the lysozyme had negligible influence on the weight loss of CHS-*g*-PCL matrix even though the majority of matrix consists of chitosan crystalline phase, as it has shown less weight loss profile 2.86± 0.36, 3.38± 0.39, 4.90± 0.60, 5.53± 0.15 after 1, 2, 3 and 4 weeks, respectively. The inability of lysozyme to cleave the glycosidic bond of chitosan polysaccharide units might be related to either the crystalline polymorph of chitosan or the depolymerization of chitosan backbone. Moreover, upon incubation with enzymes free PBS solution, the samples didn't show significant weight loss for the first three weeks about 2.8±0.1 %,

samples didn't show significant weight loss for the first three weeks about 2.8±0.1 %, however, the weight loss increased to 4.25±0.3 % after one month. It has been reported that the degradation rate of pure PCL scaffolds is very slow due to its inherent hydrophobicity and crystallinity as it showed maximum weight loss of 1% over 10 weeks of immersion in the PBS solution (Wan et al., 2008). Therefore, grafting of PCL onto chitosan chains increased the weight loss of PCL phase to around 4 % after shorter incubation time which is close to the weight loss values reported for different ratio of PCL/CHS blend over same time intervals (Wan et al., 2008).

5.3.3 Immobilization of silicatein and biosilica on CHS-*g*-PCL polymer surface
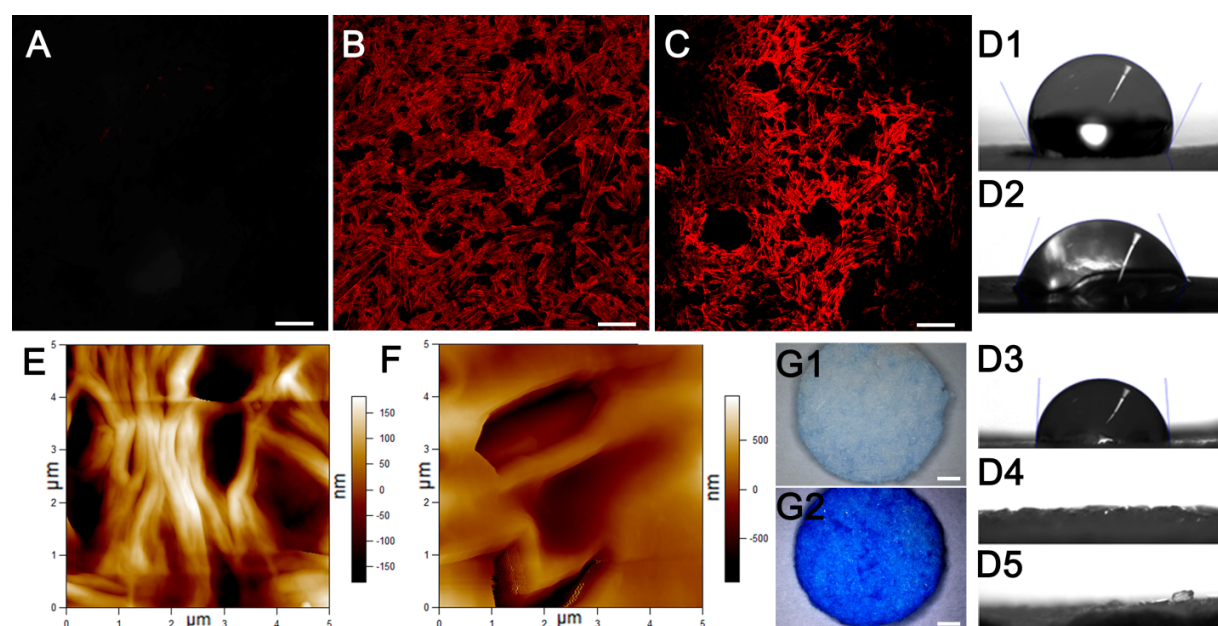
Fig 5.4 Visualization of immobilized silicatein on CHS-*g*-PCL polymer (CP) surfaces and the investigation of surfaces wettability, (B) CLSM micrographs of silicatein immobilized on, (C) on the diamine functionalized CHS-*g*-PCL polymer; CPNH, (A) CHS-*g*-PCL surface treated with a combination of anti-silicatein primary antibodies, Cy3-labeled secondary antibodies as negative control; bar 50 μm. Contact angle images on casted PCL membrane (D1), CP membrane (D2), CPNH membrane (D3), CPNH immobilized with only silicatein (D4) and CPNH immobilized with silicatein/biosilica (D5). AFM height images of grafted polymer CP surface (E) and CPNH surface immobilized with silicatein CPP (F). Coomassie protein staining of non-immobilized sample CPNH (G1) as negative control and silicatein immobilized surface CPP (G2); bar 750 μm

Biosilica formed enzymatically by silicatein was proven to improve the cellular response *via* osteoinductive and osteogenic potential (Wang et al., 2012). Therefore, silicatein was immobilized on CHS-*g*-PCL surface *via* ionic interactions between the negatively charged silicatein and positively charged polymer surfaces, requiring no complex or aggressive chemistries (Jochems et al., 2011). Therefore, CHS-*g*-PCL aminolysis was preformed to increase the density of ionized amine groups for electrostatic interaction with silicatein, based on the detection of PCL carbonyl groups peak at 1724 cm^{-1} in ATR-FTIR spectrum of CP sample (Fig. 5.2C) which could be targeted with diamine. The silicatein immobilized on both CP surface and the diamine functionalized surface (CPNH) was detected using immunostaining techniques. Both surfaces were exposed to polyclonal antibodies (PoAb-aSilic) rose against silicatein and subsequently incubated with secondary goat anti-rabbit antibodies fluorescent Cy3-labeled to be monitored by CLSM (Fig. 5.4 B and C). Strong fluorescent signals were elicited from CPNH surface (Fig. 5.4C) compared to CP surface (Fig. 5.4B), indicating the enhancement of silicatein immobilization by PCL aminolysis. The CLSM images show that the fluorescent signals are intensely observed at crystals circumference, supposedly because of the presence of chitosan functional groups and PCL polymer. As a control, non-immobilized surface with silicatein treated with only 1st and 2nd antibodies shows no fluorescence after blocking of non-specific binding sites (Fig. 5.4A). Quantitatively, the immobilized silicatein concentration was measured by Bradford assay to be 200±20 $\mu g/cm^2$ after incubating CPNH specimens, while this value was lesser (100±15 $\mu g/cm^2$) on the non-functionalized CP sample, which is consistent with the aforementioned intense fluorescent signal for sample CPNH. Initial cell adhesion, proliferation, and migration are significantly affected by the wettability of cell-biomaterials interface as the moderate hydrophilic surfaces are preferable (Arima & Iwata, 2007). The surface wettability of CP and the surface functionalized CPNH polymers was assessed by the sessile drops water contact angle measurement and compared to the surface of PCL membrane prepared by casting 2% PCL dissolved in DCM into films. The video contact angle images of different surfaces are shown in Fig. 5.4D. The casted PCL film surface showed hydrophobic surface with a contact angle of 115 ± 1°. In case of CHS-*g*-PCL, a decrease in the contact angle values (80 ± 5°) was

observed, due to the presence of hydrophilic functional groups, such as carbonyl, carboxylic, hydroxyl, protonated amine and amide groups in consistent with ATR-FTIR results. Further, the membrane surface treated with diamine became more hydrophilic with contact angle value decreasing to 75 ± 3°. On the other hand, complete wettability was observed for CPP and CPPS surfaces corresponding to water contact angles of 0° for surfaces that had been immobilized with silicatein and silicatein/biosilica, probably due to the solubilization of silicatein on the lyophilized sample surfaces. On the other hand, limited extent in swelling of polymeric matrix is required to infiltrate the cells inside the matrix and release the incorporated bioactive compound, as high swelling index causes lost in the material integrity in the aqueous media. The swelling behavior of sample CP was quantified by measuring the changes in sample weight as a function of immersion time in PBS at RT and neutral pH. The time-dependent swelling index (SI) profile showed an increase in sample weight to 12.17±0.44, 14.92±0.48, 15.66±0.65, 18.58±0.23 after 1, 2, 3 and 4 weeks, respectively. The increase in grafted polymer membrane ability to retain water after 1 week and 1 month might be related to the detection of ionized amine band at 1534 cm^{-1} in its ATR spectrum (Fig. 5.2C) as well as the porosity of the amphiphilic network. The AFM analysis was performed to investigate the morphology of the surface before and after immobilization with silicatein. When the surface morphology of both CP and CPP was probed with AFM, three-dimensional surface plots of height (Fig. 5.4 E and F) showed that CHS-*g*-PCL surface was rough and exhibited network of fiber bundles. Immobilization of silicatein resulted in a smooth surface and the increases in the height. Furthermore, for monitoring the distribution of immobilized protein by digital images, both CPNH and CPP samples were incubated with the protein stain SimplyBlue Coomassie. The surface immobilized with silicatein elicited an intense blue color (Fig. 5.4G2) compared to faint color of non-immobilized surface (Fig. 5.4G1), indicating that the protein is well distributed on the surface. For further morphological assessment, SEM images of sample CP (Fig. 5.5 A1-A3) showed 3D network of microcrystalline chitosan (MCCS) elongated crystals with different lengths, assumably caused by different degree of chitosan chains depolymerization. The sharp characteristic peaks for chitosan observed in the XRD pattern (Fig. 5.1.C) is in good agreement with the morphology of crystals shown by SEM images.
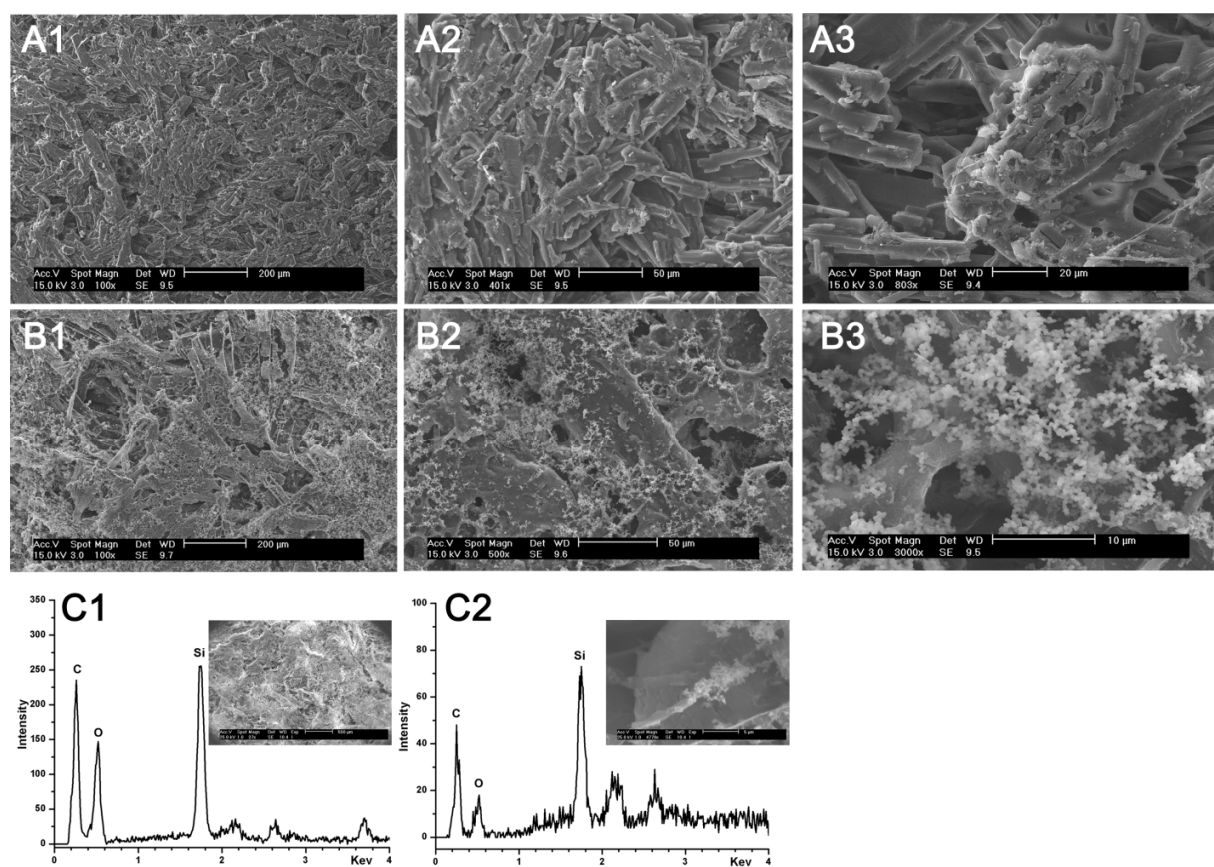
Fig. 5.5 SEM images of CHS-*g*-PCL network (A1-A3) and CHS-*g*-PCL surface immobilized with silicatein/biosilica (B1-B3 and C1, C2).

Hydrophobic PCL chains are expected to stabilize the MCCS into 3D structure by formation of junction zones, which connect MCCS crystals together by intermolecular hydrophobic aggregation (Philippova et al., 2001) as can be seen in high magnification SEM image (Fig. 5.5A3). The ability of chitosan derivatives to assemble in solution and form different morphologies is highly dependent on the molecular weight, pH value and the concentration. Otherwise, SEM images of the lyophilized samples coated with silicatein and biosilica are shown in Fig. 5.5 B1-B3. In consistency with immunostaining results, coated silicatein is well dispersed on the crystals surface showing network feature, probably due to the incomplete dehydration of the surface coated silicatein after lyophilization. Furthermore, biosilica nanoparticles are co-localized with silicatein, as

silicatein provides surface features for direct binding with the silanol functionality on the inorganic silica particles, this binding can be seen with high magnification image (Fig 5.5C2). Additionally, the selected area EDAX spectra Fig (5.5 C1 and C2) indicated the presence silica peak at 1.74 Kev as well as 0.25 and 0.52 Kev for carbon and oxygen respectively due to either protein skeleton or the polymers backbone.
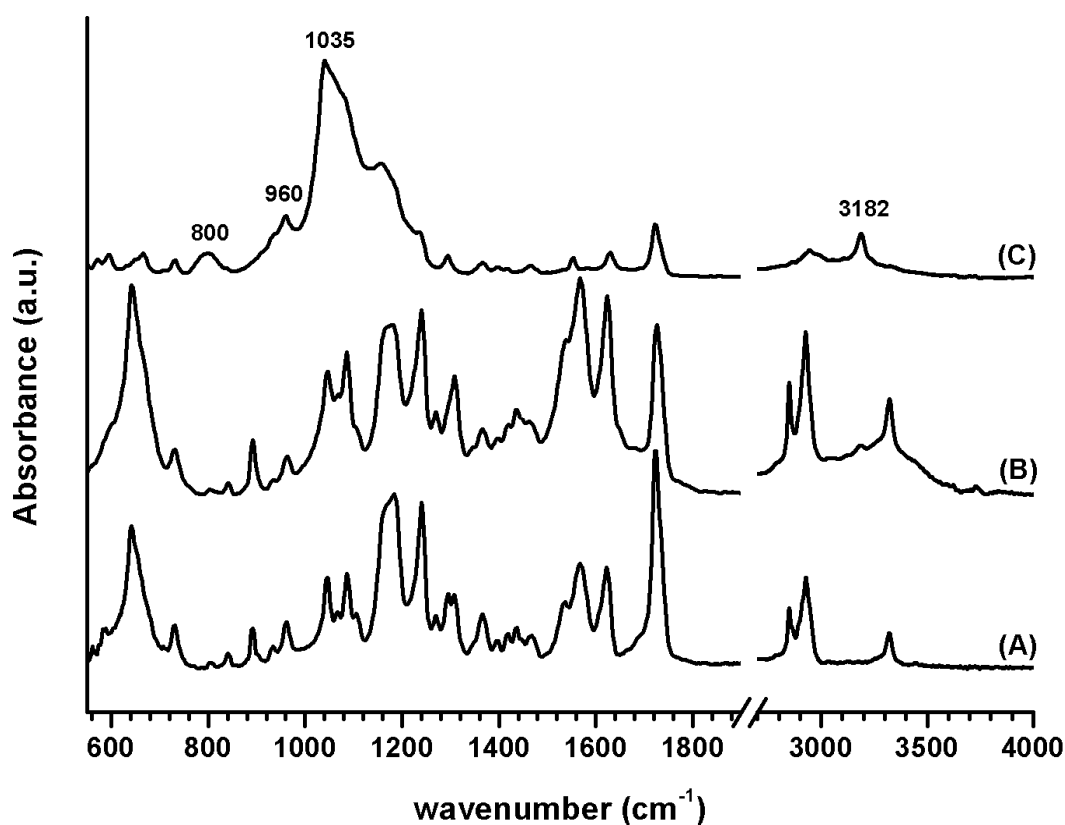
Fig. 5.6 ATR-FTIR spectroscopy of silicatein and silicatein/biosilica immobilized on CHS-*g*-PCL surface, (A) CHS-*g*-PCL surface (CP), (B) CHS-*g*-PCL surface immobilized with silicatein (CPP), (C) CHS-*g*-PCL surface immobilized with silicatein/biosilica layer (CPPS)

Finally, the layer of either silicatein or silicatein/biosilica coated electrostatically on the CHS-*g*-PCL surfaces was further assessed with ATR-FTIR spectroscopy (Fig. 5.6). The spectral analysis gave three distinct bands with enhanced related to silica species at

800, 960, and 1035 cm^{-1}, attributed to Si−O−Si bending, Si−OH, and Si−O−Si stretching vibrations respectively (Fig. 5.6C). The spectra in the range of 1700-1500 cm^{-1} are correlated with amide I, amide II and amide III of both chitosan and protein; however, it showed enhanced intensity in the presence of protein layer (Fig. 5.6B). The peak appeared at 3182 cm^{-1} in CPP spectrum with low intensity and in CPPS spectrum with higher intensity might be related to the hydrogen bond formed between silicatein surface serine residues or the polymerized biosilica with CP surface functional groups, especially carboxylic acid groups. This peak was detected in chapter 4 after immobilizing the enzymatically formed biosilica on silanol rich surface (Wiens et al., 2013). The reduction in the spectral intensities of -NH wagging at 642 cm^{-1}, amide II at 1567 cm^{-1} and –NH stretching at 3322 cm^{-1} of secondary amide bond (Fig. 5.6C) might be attributed to either the inability to be detected by ATR technique because of the coated silica layer thickness exceeded 5 μm or the ability of the secondary amide bonds to form hydrogen bond with silica particles through their interaction with free electron pair on its nitrogen atoms. Similar interaction has been proposed for the actylated chitosan with other metal oxide particles (Bhattarai et al., 2007).

5.3.4 Cellular response to the surfaces under investigation

5.3.4.1 Cytotoxicity and proliferation of SaOS-2 cells

Figure 5.7 shows the absorbance values of solubilized formazan crystals as an evidence for SaOS-2 cells viability and proliferation on the surfaces of tissue-culture polystyrene plate (TCPS), CHS-*g*-PCL polymer (CP), silicatein coated on CP surface (CPP) and silicatein/biosilica coated on CP surface (CPPS) on days 2 to 6 after cell culturing. All of the investigated surfaces were non-toxic to the cells, since the average absorbance values were all close to that of TCPS. Interestingly, all of the average absorbance values for biosilica coated surface (CPPS) were much higher than TCPS surface, suggesting that biosilica might be able to enhance the focal adhesion of SaOS-2 cells cytoskeleton and consequently allowing more cells to spread and divide on its surface. Furthermore, the negatively charged silanol groups on the biosilica surface might be responsible for adsorbing essential proteins from the FCS commonly

supplemented in the culture medium providing suitable sites for cell adhesion (Ning et al., 2005).
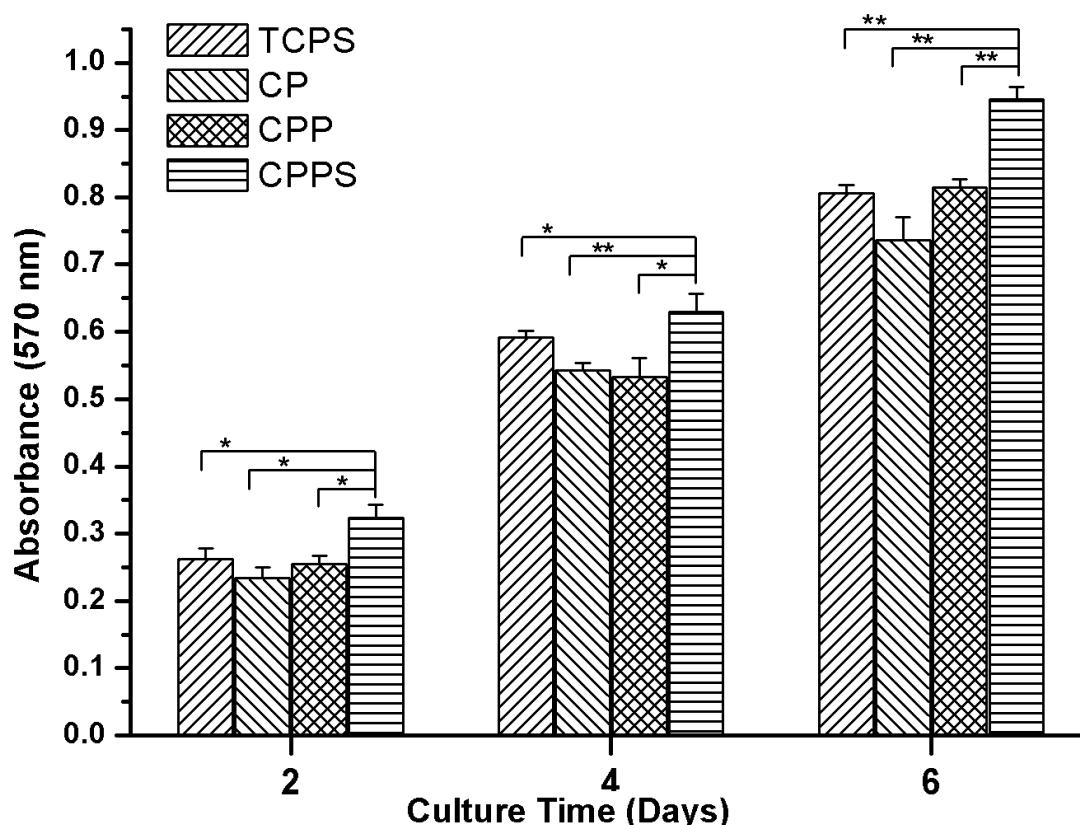

Fig. 5.7 Cytotoxicity and proliferation assay of SaOS-2 osteoblast like cells cultured on different surfaces over 6 days, tissue-culture polystyrene plate (TCPS), CHS-*g*-PCL polymers (CP), silicatein electrostatically immobilized on CP surface (CPP), biosilica formed enzymatically by the immobilized silicatein on CP surface (CPPS).

5.3.4.2 Immunocytochemistry

The distribution both cells and silicatein on silicatein immobilized surface (CPP) after 3 and 6 days of SaOS-2 cells incubation was visualized by immunostaining with specifics antibodies against silicatein and the fluorescent DNA dye (DRAQ5) for cellular nuclei (Fig. 5.8). As mentioned before in section 5.3.3, the fluorescent signals are strong at the

surrounding area of the chitosan microcrystals (Fig. 5.8 C and D), at which the diamine functionalized PCL segments are attached to the circumference of the crystals providing positively charged sites for silicatein adhesion. Concurrently, the blue fluorescent signals for the cellular nuclei were found to be overlapped with the red signal for Cy3 labeled silicatein antibodies indicating that the non-toxicity of immobilized silicatein. Furthermore, the fluorescence images with low magnifications show that the cell density was higher after 6 days (Fig. 5.8A) of incubation with SaOS-2 cells compared to 3 days incubation period (Fig. 5.8B). These fluorescent images indicate that the electrostatic immobilization of silicatein was stable in cell culture medium up to 6 days of incubation, providing compatible interface for cells adhesion.
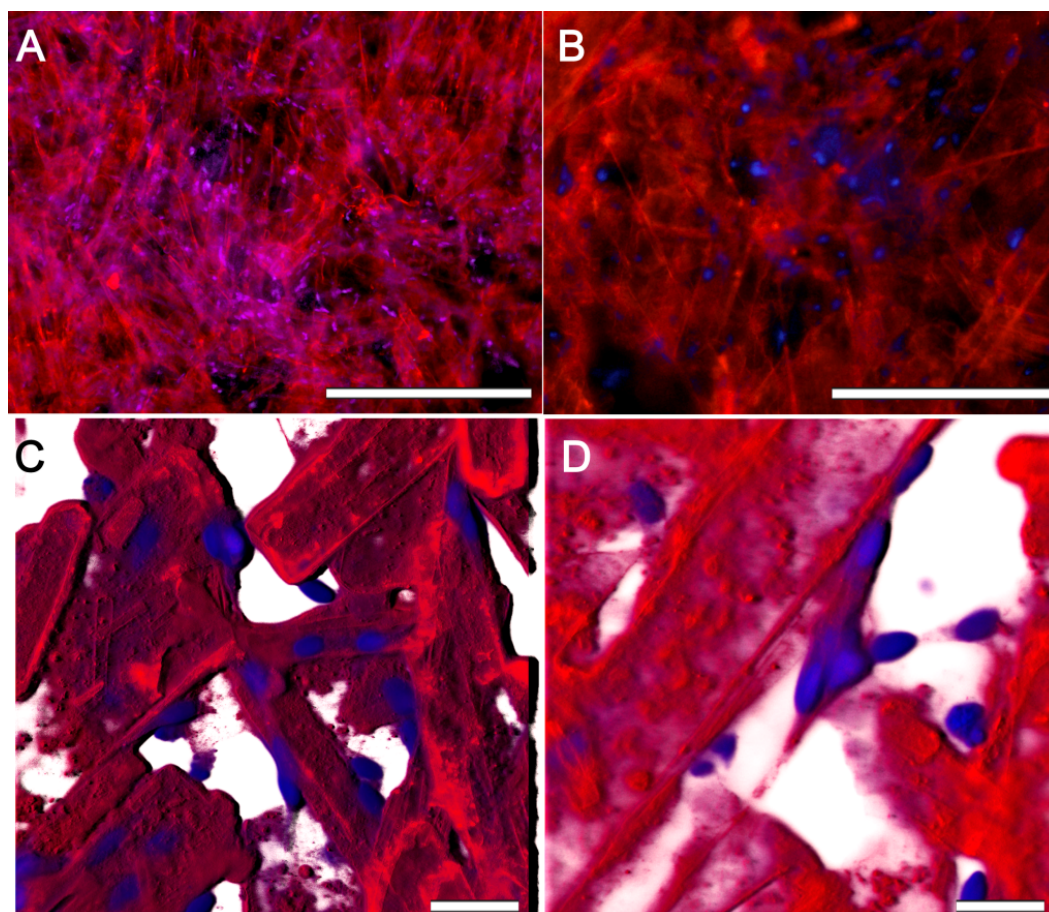
Fig. 5.8 Fluorescent visualization of silicatein primary antibodies and SaOSs-2 cells nuclei on CS-*g*-PCL surface after 3 and 6 days of cell culture, fluorescence images after 3 (B) and 6 (A) days; bars 200 μm and 400 μm respectively, 3D fluorescence image stacks by CLSM after 3 (C) and 6 (D) days; bars 50 μm

5.3.4.3 Quantitative and qualitative mineralization assays
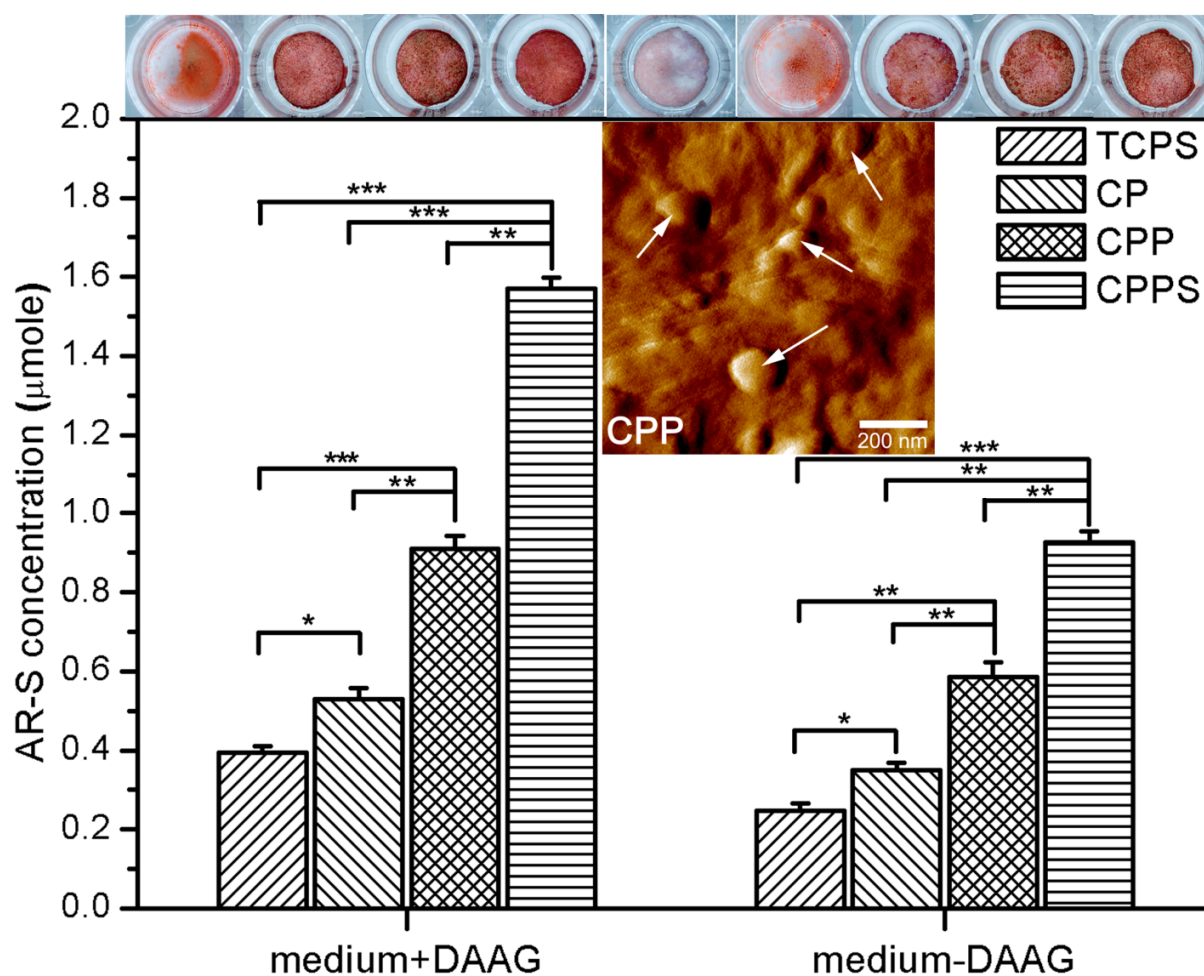
Fig. 5.9 Effects of the surface immobilization with silicatein and biosilica on biomineralization in SaOS-2 osteoblast-like cells, the upper figures show the optical images of Alizarin red S (AR-S) staining for mineralization after 10 days of seeding SaOS-2 cells on TCPS, CP, CPP and CPPS surfaces in the osteogenic medium (10 nM dexamethasone, 50 μM ascorbic acid, and 5 mM β-glycerophosphate) and normal medium, the lower figure shows the quantification of mineral deposition by AR-S staining. The upper figures have the same order corresponding to the columns in the lower figures. The inset is AFM image of CPP surface with higher magnification than in Fig 5.4F showing silicatein aggregates embedded in lyophilized protein.

The quantification of AR-S (Fig. 5.9) showed that immobilization of silicatein on CHS-*g*-PCL surface (CPP) increases the mineralization significantly by ~72% in osteogenic

medium and by ~67% in normal medium compared to CP surface. This might be attributed to the interaction between immobilized silicatein and calcium ions in the renewed culture medium through surface accessible amino acid residues of silicatein such as aspartic, glutamic acids, and serine. Furthermore, silicatein is well known as polymerizable protein that can assemble rapidly in an aqueous solution into aggregates in the absence of urea (Müller et al., 2013a). The deposition of these aggregates on CHS-*g*-PCL surface might provide solid protein interface for heterogeneous nucleation of hydroxyapatite on their surface initiated by ionic interaction between the protein aggregates surface and calcium ions. Through the interaction between silicatein mature oligomers and calcium ions, flexible calcite spicules have been fabricated artificially, whereas, recombinant silicatein-α was used as an organic matrix to accelerate the crystallization of calcium carbonate and to guide the assembly of microscale spicules *via* protein-protein interaction (Natalio et al., 2013). The AFM image inset of CHS-*g*-PCL surface immobilized with silicatein (Fig. 5.9) shows the formation of silicatein spherical aggregates with diameter ranged from 50-150 nm which might act as an interface for hydroxyapatite deposition. This might be related to the increase of quantified biominerals in case of CPP sample compared to the pristine polymer surface. Otherwise, the biosilica attached to silicatein on CP surface enhanced further the quantified bio-minerals by 72 % in osteogenic medium and by ~58% in normal medium compared to CPP surface. However, the capability of pristine CHS-*g*-PCL surface to increase the deposited HA on its surface by 37% compared to the polystyrene culture plate (TCPS) might be directly related to the detected functional groups in the ATR-FTIR spectrum of sample CP. In fact, both ionized amine group and carboxylate ions might electrostatically attract either phosphate or calcium ions from the culture medium in addition to the minerals produced differentiated cells on the material surface.

In order to calculate the amount of precipitated apatite in case of biosilica coated samples, we considered the molar ratio in alizarin red S-calcium complex (AR-S: Ca^{2+}; 1:2) and the stoichiometric hydroxyapatite molecular structure (HA; $Ca_{10}(PO_4)_6(OH)_2$) for simplicity. Accordingly, after 10 days of cell culture, biosilica coated samples were able to precipitate 315 μg and 186 μg HA in osteogenic medium and normal medium,

respectively. Noteworthy, Osteogenic medium contains dexamethasone, ascorbic acid, and β-glycerophosphate (DAAG) is commonly used in the *in vitro* cell culture model to enhance the biomineralization of osteoblast cells extracted from different sources, however, this medium contains both osteoconductive and osteoinductive supplements that might interfere with the osteogenic properties of the investigated materials (Gaharwar et al., 2013; Coelho & Fernandes, 2000). Therefore, the difference in mineralization increment between the osteogenic and the normal medium was calculated for all investigated surface. The mineralization was increased by average value of 55% (SD = 0.036) after adding the osteogenic compounds for all investigated surface, while, the biosilica coated samples showed 70% increase in mineralization. This difference might be related to the additional osteogenic potential of biosilica on the enhancement of cellular mineral density, probably due to either their partial dissolution resulting in silicate ions release (Mieszawska et al., 2010) or the internalization of detached biosilica after dissolving silicatein on material surface (Gaharwar et al., 2013).

It is well established that the facial deposition of semi-crystalline non-stoichiometric hydroxyapatite on the biomaterial surface precedes either acellularly due to the electrostatic interaction between calcium and phosphate ions with versatile functional moieties on biomaterial interface or intracellularly via matrix vesicles (Boonrungsimana et al., 2012). In either cases, well crystallized hydroxyapatite phase is finally formed by phase transformation of different calcium phosphate phases including amorphous calcium phosphate (ACP), brushite, octacalcium phosphate (OCP) (Dorozhkin, 2010). Therefore, the osteoimage was used additionally for biomineral investigation due to its specific binding to hydroxyapatite nodules compared to Alizarin red that forms complex with calcium sites in any calcium phosphate phase. Concurrently, the nuclei and the cytoskeleton F-actin of SaOS-2 cells were stained with DRAQ5 and Rhodamine-Phalloidin, respectively, to investigate the cellular attachment and spreading on the surfaces under investigation.
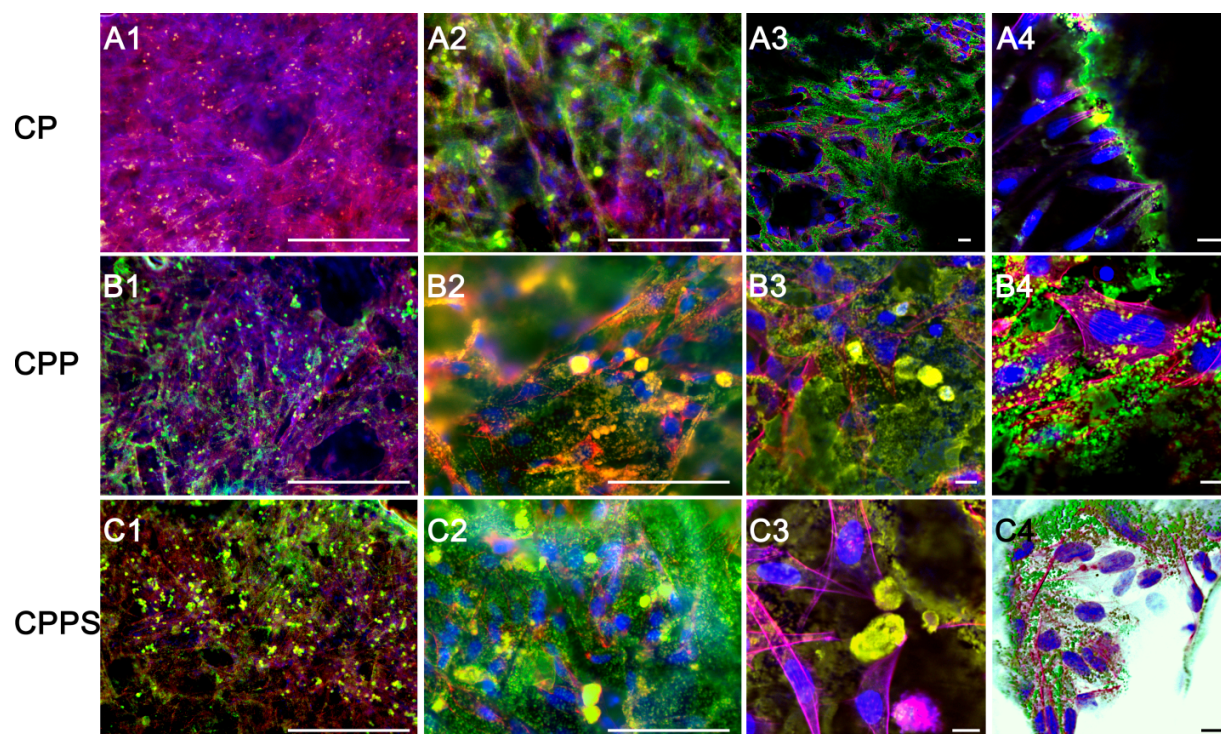
Fig 5.10 Fluorescent staining of SaOS-2 cells for investigation of cellular attachment, spreading and hydroxyapatite (HA) nodules formation. SaOS-2 cells were seeded for 10 days in osteogenic medium on CS-*g*-PCL surface (CP), CP immobilized with silicatein (CPP) and CPP incubated with pre-hydrolyzed TEOS for biosilica formation (CPPS). The first two columns and the second two columns represent fluorescence light microscopy and CLSM images, respectively, of SaOS-2 cells stained with DRAQ5 (blue, nuclei) and Rhodamine-Phalloidin (F-actin, red), HA nodules was stained with osteoimage (green); bars: the first column (400 μm), second column (100 μm), last two columns (10 μm).

Figure 5.10 shows fluorescence microscope images and CLSM images of the ECM hydroxyapatite nodules formed on different surfaces after seeding SaOS-2 cells for 10 days in osteogenic medium. As clearly seen in low magnification images (Fig 5.10 A1, B1 and C1) that the amount and the size of the rounded hydroxyapatite nodules were increased on the surface coated with biosilica due to the acceleration of HA crystallization on biosilica surface. Moreover, the amount of the nodules is higher in the samples coated with silicatein (CPP) compared to non-coated samples (CP), suggesting the role of serine rich protein oligomers to act as nucleation sites for calcium ions and subsequently accelerating the crystallization of HA phase (Fig. 5.10 B1-B4). Additionally, the staining of the nuclei and the F-actin of the SaOS-2 cells (Fig. 5.10 A2,

B2 and C2) on different surfaces shows that the cells have spread on all surfaces and maintained their vitality. The figures also reveal that the cells grow not only at the chitosan microcrystal circumference but also on the crystal interfaces. Figure 5.10 A3 and A4 represents confocal image of the SaOS-2, it can be seen that the cells are well distributed over the CS-*g*-PCL surface and able to extend and bridge between chitosan microcrystals. Fig. 5.10 C3 shows the focal adhesions between spindle-shaped SaOS-2 filopodia and the hydroxyapatite nodules, which probably mediated via acidic non-collagenous protein such as osteopontin that has in its sequence both calcium binding sites and RGD sequence as integrin recognition site (Lian & Stein, 1992). This protein was found highly unregulated in the presence of silicate ions and silica nanoparticles (Müller et al., 2013b; Gaharwar et al., 2013). The 3D stack CLSM image (Fig. 5.10 C4) summarizes all cellular behaviors observed on sample CP coated with silicatein/biosilica such as cell birding, invasion of matrix porosity, adhesion, well spread spindle-like cells. The biomineralization results indicate that the entire surfaces under investigation are apparently osteoconductive due to the formation of HA nodules after culturing with SaOS-2 cells for 10 days. The extent of HA deposition on the surface are assumedly governed by many factor like the difference in the surface charge due to silicatein and/or biosilica, silicatein oligomerization, the topography/roughness of the polymeric surface, and the partial dissolution of biosilica.

5.3.4.4 Alkaline phosphatase (ALP) activity

Alkaline phosphatase (ALP) belongs to a group of membrane-bound glycoproteins found on the cell surface and in matrix vesicles of the bone-forming cells, therefore, it is considered to be an important marker of their differentiation and mineralization at a relatively early bone forming stage (Golub & Boesze-Battaglia, 2007). During the initial cell adhesion and proliferation, ALP expression and activity are steady and low, however, on substrates that promote cells differentiation, ALP activity increases and participates in the process of preparation of the ECM for the deposition of minerals and then decreases as mineralization progresses.
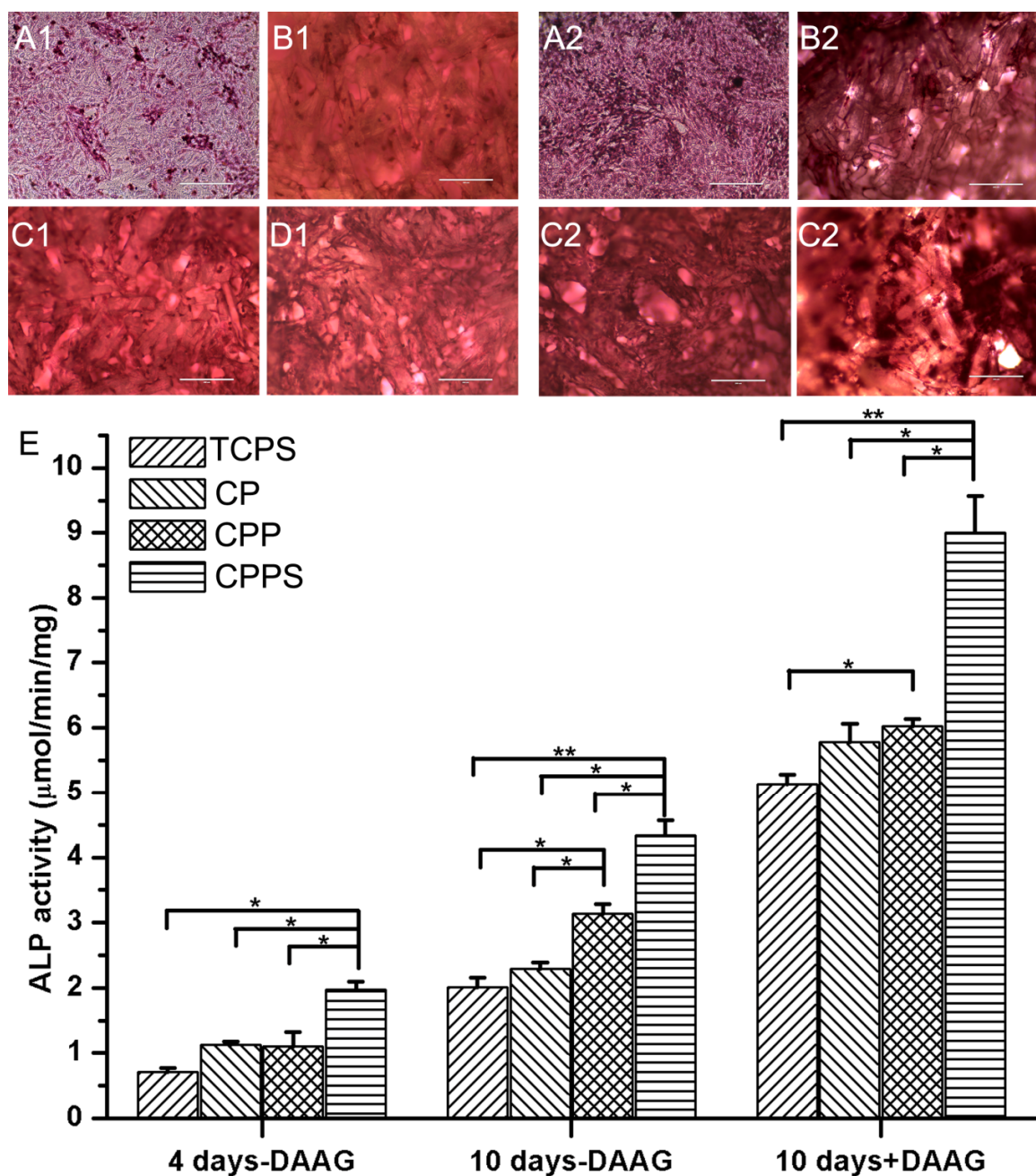
Fig. 5.11 Qualitative and quantitative analyses of alkaline phosphatase activity for the investigated surfaces after 4 and 10 days in normal medium and 10 days in osteogenic medium, Cells were either seeded on different surfaces in normal medium (A1-C1) or osteogenic medium (A2-C2) and then the surfaces stained against ALP enzyme with naphthol AS–BI phosphate and fast red violet LB salt (A) TCPS, (B) CP, (C) CPP, and (D) CPPS; bars, 200 μm. Additionally, (E) Alkaline phosphatase activity of SaOS-2 cell lysate extracted from each abovementioned surface and normalized by the total cellular proteins.

SaOS-2 cell differentiation and mineralization was assayed qualitatively by ALP staining on the cell surface (Fig. 5.11; upper panel) and quantitatively by ALP activity assay (Fig. 5.11; lower panel). Both analyses are based on the ability of active ALP to hydrolyze phosphate esters compounds (i.e naphthol AS-BI phosphate and p-nitrophenyl phosphate) at alkaline environment. Saos-2 cells on the biosilica coated surface showed stronger ALP staining than other surfaces in both osteogenic and normal mediums on day 10 after culturing, as shown in Fig. 5.11 D1 and D2: upper panel. Furthermore, Fig. 5.11 (lower panel) illustrates the ALP activity of the cells cultured for 4 and 10 days on different surfaces in the presence and absence of the osteogenic compounds. A significant increase (~76%) in ALP activity was only noticed for biosilica coated sample at 4 days which might indicate that biosilica exert a significant impact on osteoblastic phenotype of SaOS-2 cells and accelerate their differentiation. In the absence of osteogenic compounds at day 10, ALP activity was increased for silicatein coated surface (CPP) by ~37 % compared to both CP and TCPS surface which might be related to the increase of calcium ions adsorption by negatively charged silicatein (PI=5.1) at neutral cell culture medium. It was proposed that the calcium ions release in extracellular matrix to certain concentration has stimulatory influence on ALP activity partly (Zhou et al., 2010; 2012 Chai et al., 2012). It is not yet known why does immobilized silicatein alone increases ALP activity. It could be linked to their ability to enhance the deposition of calcium phosphate as has been observed by AR-S staining or stimulating of the expression of extracellular matrix. The accumulation of acellular HA deposited is highly expected since the culture media were refreshed each 3 days and since the enzyme ionically bound to the surface was stable up to 6 days of incubation (Fig. 5.8 A and C). Generally, the cells cultured in presence of osteogenic medium showed an increase in ALP activity when compared to other surfaces due to presence of dexamethasone (DEX), ascorbic acid (AA) and β-glycerophosphate (β-GP) that participate in cells differentiation, production of the collagenous extracellular matrix, and mineralizing agent contains pounded inorganic phosphate (Pi), respectively (Coelho & Fernandes, 2000). ALP promotes mineralization by degrading inorganic pyrophosphate (PPi) and polyphosphates (polyP) *in vivo* or β-GP in cell culture model generating free Pi ions which induce both differentiation and mineralization of osteoblasts (Wang et al.,

2012). Saos-2 on biosilica surface shows significant increase in ALP activity at all time points, with and without osteogenic medium compared to other surfaces, consistent with the well established role of silica and silicate ions to enhance the bone mineral density (Wang et al., 2012; Jugdaohsingh, 2007). The ALP activity results are consistent with the ALP activity profile observed in chapter 4 by seeding SaoS-2 cells on silanol rich copolymer immobilized with biosilica formed enzymatically using silicatein.

5.3.4.5 Dehydrated cells morphology
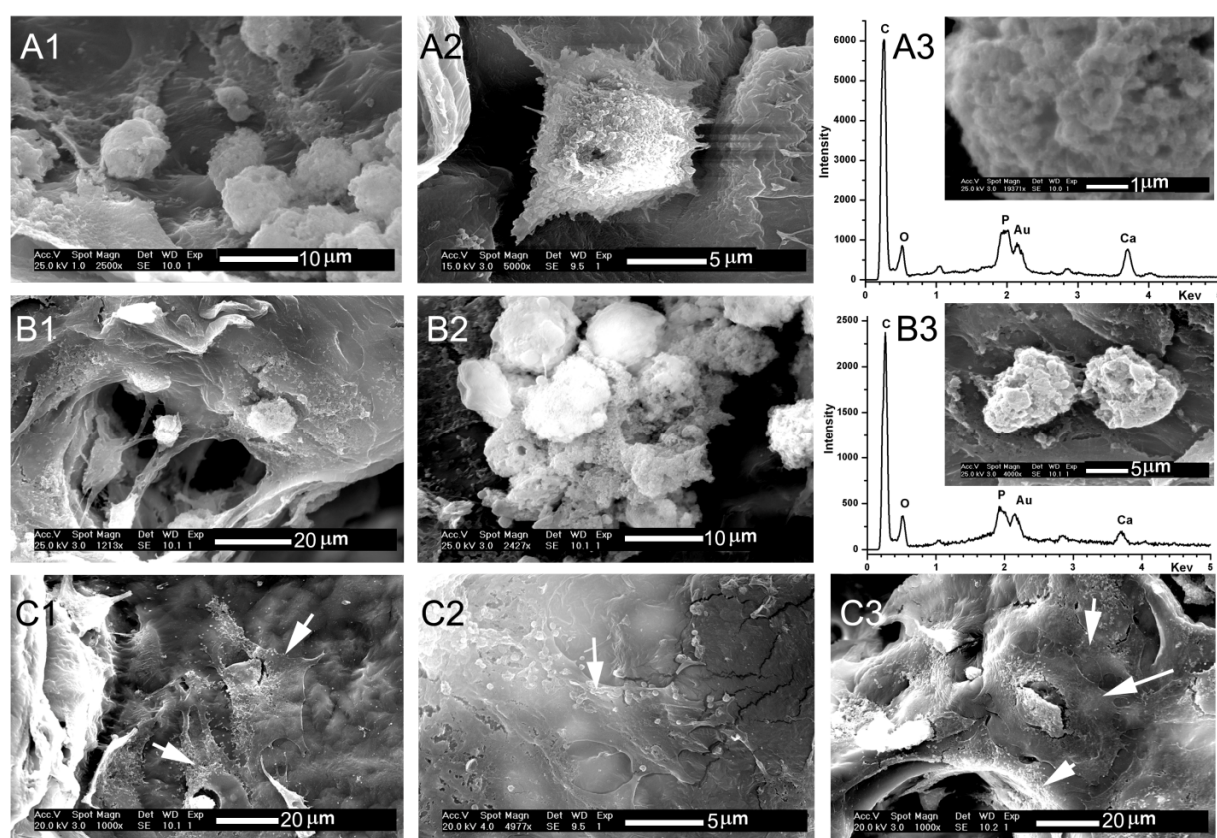
Fig. 5.12 SEM images and EDX spectra of CP, CPP, and CPPS surfaces seeded with 50,000 SaOS-2 cells cultured for 4 days in normal medium. (A) CP surface, (B) CPP surface, and (C) CPPS surface, the inserts represent the selected area images for EDX analysis.

SEM after SaOS-2 cell dehydration (Fig. 5.12) was used to show the effect of immobilized silicatein and biosilica on the osteoblastic phenotype compared to the CHS-

g-PCL surface in the absence of osteogenic compounds and correlated with the ALP results at 4 days after culture. The observed small and rounded shape morphology (A1) on the CS-*g*-PCL surface (CP) was consistent with a very early stage of adhesion, while at higher magnification image (A2), cells showed cytoplasmic extensions (filopodia), indicating cells spread on CP surface. Similar rounded shape cellular morphology with short radial-growth of filopodia was observed at day 3 by previous report on CHS/PCL blend (Shao et al., 2010), however, increasing of PCL percentage in the blend above 25 wt% changed the cellular morphology into spindle like shape with long filopodia. A higher power magnification of SaOS-2 surface (C3), the selected area EDX spectra showed both calcium and phosphorus elements, suggesting the uptake of these ions by SaOS-2 cells for intracellular mineralization (Boonrungsimana et al., 2012). It is noteworthy to mention that the diameter of SaOS-2 is much smaller than the osteoblast cells, around 10 μm and 20 μm in either rounded shape or flattened shape, respectively (Pautke et al., 2004). On the other hand, the flattened polygonal cellular morphology that observed biosilica coated surfaces (indicated by arrow, C1-C3) is usually associated with the fully spread osteoblast that undergo differentiation. Therefore, the cellular morphology at day 4 might emphasize the higher ALP activity (Fig. 5.11E) estimated from the samples coated with biosilica (CPPS) after 4 days. Elongated (anisotropic) cell morphology was observed by other researchers on surfaces coated with silica nanoparticles due to the effect of the silica surface roughness on cells morphology (Lipski et al., 2008). These results might indicate that the biosilica coated surface supports cell adhesion, spreading and differentiation faster that other investigated surface in the current study.

In conclusions, Microcrystalline chitosan-polycaprolactone graft was successfully prepared by a coupling reaction between the carboxylic terminal groups of PCL chains and the amino groups of chitosan by initially modifying the carboxylic terminated PCL to succinimide ester terminated PCL. Needle like chitosan microcrystals were precipitated at slightly alkaline pH necessarily for the coupling reaction and then hydrophobically stabilized by PCL *via* formation of amide linkage. The resultant polymers graft is highly shapeable in wet state and the molded solid membranes showed adequate cellular

adhesion, proliferation and mineralization upon incubation with SaOS-2 cells for different time intervals. PCL aminolysis was used to increase the density of ionized amine groups of the graft surface and subsequently enhanced their immobilization of silicatein ionically for catalyzing the polymerization of biosilica. The graft surface coated with biosilica showed significantly improved cellular response compared to other surfaces including cell adhesion, proliferation, osteoblast phenotype at early stages, enhanced surface mineralization and HA nodules formation accompanied by elevated level of alkaline phosphatase activity. The results in this study suggest that MCCS-*g*-PCL is suitable as orthopedic implant and its osteogenic capability can be stimulated by immobilizing biosilica on the graft surface. Further studies on surface mechanics and *in vivo* implantation in the calvarial bone defect model are currently under investigation.

5.4 References

Arima Y. & Iwata H. (2007). Effect of wettability and surface functional groups on protein adsorption and cell adhesion using well-defined mixed self-assembled monolayers. *Biomaterials* 28, 3074-3082.

Aroguz A.Z., Baysal K., Tasdelen B. & Baysal B.M. (2011). Preparation, characterization, and swelling and drug release properties of a crosslinked chitosan-polycaprolactone gel. *Journal of Applied Polymer Science* 119, 2885-2894.

Beck Jr G.R., Ha S.W., Camalier C.E., Yamaguchi M., Li Y., Lee J.K. & Weitzmann M.N. (2012). Bioactive silica-based nanoparticles stimulate bone-forming osteoblasts, suppress bone-resorbing osteoclasts, and enhance bone mineral density in vivo. *Nanomedicine: Nanotechnology, Biology and Medicine* 8, 793-803.

Bhattarai S.R., Bahadur KC R., Aryal S., Khil M.S. & Kim H.Y. (2007). N-Acylated chitosan stabilized iron oxide nanoparticles as a novel nano-matrix and ceramic modification. *Carbohydrate polymers* 69, 467-477.

Boddu V.M., Abburi K., Talbott J.L. & Smith E.D. (2003). Removal of hexavalent chromium from wastewater using a new composite chitosan biosorbent. *Environmental science & technology* 37, 4449-4456.

Boonrungsiman S., Gentleman E., Carzaniga R., Evans N.D., McComb D.W., Porter A.E. & Stevens M.M. (2012). The role of intracellular calcium phosphate in osteoblast-mediated bone apatite formation. *Proceedings of the National Academy of Sciences* 109, 14170-14175.

Brinkley M. (1992). A brief survey of methods for preparing protein conjugates with dyes, haptens and crosslinking reagents. *Bioconjugate chemistry* 3, 2-13.

Castilla-Cortázar I., Más-Estellés J., Meseguer-Dueñas J.M., Escobar Ivirico J.L., Marí B. & Vidaurre A. (2012). Hydrolytic and enzymatic degradation of a poly(ε-caprolactone) network. *Polymer Degradation and Stability* 97, 1241-1248.

Chai Y.C., Carlier A., Bolander J., Roberts S.J., Geris L., Schrooten J., Van Oosterwyck H. & Luyten F.P. (2012). Current views on calcium phosphate osteogenicity and the translation into effective bone regeneration strategies. *Acta Biomaterialia* 8 3876–3887.

Coelho M.J. & Fernandes M.H. (2000). Human bone cell cultures in biocompatibility testing. Part II: effect of ascorbic acid, *β*-glycerophosphate and dexamethasone on osteoblastic differentiation. *Biomaterials* 21, 1095-1102.

Dash M., Chiellini F., Ottenbrite R.M. & Chiellini E. (2011). Chitosan—A versatile semi-synthetic polymer in biomedical applications. *Progress in Polymer Science* 36, 981-1014.

Dong Y., Sakurai K., Wu Y. & Kondo Y. (2002). Multiple crystalline morphologies of N-Alkyl chitosan solution cast films. *Polymer Bulletin* 49, 189-195.

Dorozhkin S.V. (2010). Amorphous calcium (ortho) phosphates. *Acta biomaterialia* 6, 4457-4475.

Duan K., Chen H., Huang J., Yu J., Liu S., Wang D. & Li Y. (2010). One-step synthesis of amino-reserved chitosan-*graft*-polycaprolactone as a promising substance of biomaterial. *Carbohydrate Polymers* 80, 498-503.

Elzein T., Nasser-Eddine M., Delaite C., Bistac S. & Dumas P. (2004). FTIR study of polycaprolactone chain organization at interfaces. Journal of colloid and interface science, 273(2), 381-387.

Feng H. & Dong C.M. (2006). Preparation and characterization of chitosan-graft-poly (ε-caprolactone) with an organic catalyst. *Journal of Polymer Science Part A: Polymer Chemistry* 44, 5353-5361.

Gaharwar A.K., Mihaila S.M., Swami A., Patel A., Sant S., Reis R.L., Marques A.P., Gomes M.E. & Khademhosseini A. (2013). Bioactive Silicate Nanoplatelets for Osteogenic Differentiation of Human Mesenchymal Stem Cells. *Advanced Materials* 25, 3329–3336.

García Cruz D.M., Coutinho D.F., Mano J.F., Gómez Ribelles J.L. & Salmerón Sánchez M. (2009). Physical interactions in macroporous scaffolds based on poly (ε-caprolactone)/chitosan semi-interpenetrating polymer networks. *Polymer* 50, 2058-2064.

Golub E.E. & Boesze-Battaglia K. (2007). The role of alkaline phosphatase in mineralization. *Current Opinion in Orthopaedics* 18, 444-448.

Hendra P.J., Maddams W.F., Royaud I.A.M., Willis H.A. & Zichy V. (1990). The application of Fourier transform Raman spectroscopy to the identification and characterization of polyamides—I. Single number nylons. *Spectrochimica Acta Part A: Molecular Spectroscopy* 46, 747-756.

Hoekstra A., Struszczyk H. & Kivekäs O. (1998). Percutaneous microcrystalline chitosan application for sealing arterial puncture sites. *Biomaterials* 19, 1467-1471.

Jochems P., Satyawali Y., Diels L. & Dejonghe W. (2011). Enzyme immobilization on/in polymeric membranes: status, challenges and perspectives in biocatalytic membrane reactors (BMRs). *Green chemistry* 13, 1609-1623.

Jugdaohsingh R. (2007). Silicon and bone health. *The journal of nutrition, health & aging* 11, 99-110.

Kittur F.S., Vishu Kumar A.B. & Tharanathan R.N. (2003). Low molecular weight chitosans—preparation by depolymerization with *Aspergillus niger* pectinase, and characterization. *Carbohydrate research* 338, 1283-1290.

Kumbar S.G., Kulkarni A.R. & Aminabhavi T.M. (2002). Crosslinked chitosan microspheres for encapsulation of diclofenac sodium: effect of crosslinking agent. *Journal of microencapsulation* 19, 173-180.

Langenbach F., Berr K., Naujoks C., Hassel A., Hentschel M., Depprich R., Kubler N.R., Meyer U., Wiesmann H., Kögler G. & Handschel J. (2011). Generation and differentiation of microtissues from multipotent precursor cells for use in tissue engineering. *Nature protocols* 6, 1726-1735.

Le Tien C., Lacroix M., Ispas-Szabo P. & Mateescu M.A. (2003). N-acylated chitosan: hydrophobic matrices for controlled drug release. *Journal of Controlled Release* 93, 1-13.

Lewandowska K. (2012). Surface studies of microcrystalline chitosan/poly (vinyl alcohol) mixtures. *Applied Surface Science* 263 115–123.

Lian J.B. & Stein G.S. (1992). Concepts of osteoblast growth and differentiation: basis for modulation of bone cell development and tissue formation. *Critical Reviews in Oral Biology & Medicine* 3, 269-305.

Lipski A.M., Pino C.J., Haselton F.R., Chen I. & Shastri V.P. (2008). The effect of silica nanoparticle-modified surfaces on cell morphology, cytoskeletal organization and function. *Biomaterials* 29, 3836-3846.

Mattanavee W., Suwantong O., Puthong S., Bunaprasert T., Hoven V.P. & Supaphol P. (2009). Immobilization of biomolecules on the surface of electrospun polycaprolactone fibrous scaffolds for tissue engineering. *ACS Applied Materials & Interfaces* 1, 1076-1085.

Michalska M., Kaplińska K., Mirowski M., Bodek A. & Bodek K.H. (2013). Evaluation of the use of fibrin and microcrystalline chitosan membranes as carriers for transforming growth factor beta-1. *Journal of Applied Polymer Science* 127, 3506-3513.

Mieszawska A.J., Fourligas N., Georgakoudi I., Ouhib N.M., Belton D.J., Perry C.C. & Kaplan D.L. (2010). Osteoinductive silk–silica composite biomaterials for bone regeneration. *Biomaterials* 31, 8902-8910.

Müller W.E.G., Boreiko A., Wang X., Krasko A., Geurtsen W., Custódio M.R., Winkler T., Lukić-Bilela L., Link T. & Schröder H.C. (2007). Morphogenetic activity of silica and bio-silica on the expression of genes controlling biomineralization using SaOS-2 cells. *Calcified tissue international* 81, 382-393.

Müller W.E.G., Schröder H.C., Muth S., Gietzen S., Korzhev M., Grebenjuk V.A., Wiens M., Schloßmacher U. & Wang X. (2013 a). The silicatein propeptide acts as inhibitor/modulator of self-organization during spicule axial filament formation. *FEBS Journal* 280, 1693-1708.

Müller W.E.G., Wang X., Grebenjuk V., Diehl-Seifert B., Steffen R., Schloßmacher U., Trautwein A., Neumann S. & Schröder H.C. (2013 b). Silica as a morphogenetically active inorganic polymer. *Biomaterials Science* 1, 669-678.

Murr M.M. & Morse D.E. (2005). Fractal intermediates in the self-assembly of silicatein filaments. *Proceedings of the National Academy of Sciences* 102, 11657-11662.

Murugan R. & Ramakrishna S. (2005). Development of nanocomposites for bone grafting. *Composites Science and Technology* 65, 2385-2406.

Natalio F., Corrales T.P., Panthöfer M., Schollmeyer D., Lieberwirth I., Müller W.E.G., Kappl M., Butt H. & Tremel W. (2013). Flexible Minerals: Self-Assembled Calcite Spicules with Extreme Bending Strength. *Science* 339, 1298-1302.

Natalio F., Link T., Müller W.E.G., Schröder H.C., Cui F.Z., Wang X. & Wiens M. (2010). Bioengineering of the silica-polymerizing enzyme silicatein-α for a targeted application to hydroxyapatite. *Acta biomaterialia* 6, 3720-3728.

Neves S.C., Moreira Teixeira L.S., Moroni L., Reis R.L., Van Blitterswijk C A., Alves N.M., Karperien M. & Mano J.F. (2011). Chitosan/Poly (ε-caprolactone) blend scaffolds for cartilage repair. *Biomaterials* 32, 1068-1079.

Ning C.Q., Mehta J. & El-Ghannam A. (2005). Effects of silica on the bioactivity of calcium phosphate composites in vitro. *Journal of Materials Science: Materials in Medicine* 16, 355-360.

Ogawa K. (1991). Effect of Heating an Aqueous Suspension of Chitosan on the Crystallinity and Polymorphs (Analytical Chemistry). *Agricultural and biological chemistry* 55, 2375-2379.

Oyane A., Uchida M., Choong C., Triffitt J., Jones J. & Ito A. (2005). Simple surface modification of poly(ε-caprolactone) for apatite deposition from simulated body fluid. *Biomaterials* 26, 2407-2413.

Pautke C., Schieker M., Tischer T., Kolk A., Neth P., Mutschler W. & Milz S. (2004). Characterization of osteosarcoma cell lines MG-63, Saos-2 and U-2 OS in comparison to human osteoblasts. Anticancer research, 24(6), 3743-3748.

Pearson F.G., Marchessault R.H. & Liang C.Y. (1960). Infrared spectra of crystalline polysaccharides. V. Chitin. *Journal of Polymer Science* 43, 101-116.

Philippova O.E., Volkov E.V., Sitnikova N.L., Khokhlov A.R., Desbrieres J. & Rinaudo M. (2001). Two types of hydrophobic aggregates in aqueous solutions of chitosan and its hydrophobic derivative. *Biomacromolecules* 2, 483-490.

Pighinelli L. & Kucharska M. (2013). Chitosan–hydroxyapatite composites. *Carbohydrate polymers* 93, 256-262.

Qin C., Zhou B., Zeng L., Zhang Z., Liu Y., Du Y. & Xiao L. (2004). The physicochemical properties and antitumor activity of cellulase-treated chitosan. *Food Chemistry* 84, 107-115.

Ren D., Yi H., Wang W. & Ma X. (2005). The enzymatic degradation and swelling properties of chitosan matrices with different degrees of *N*-acetylation. *Carbohydrate Research* 340, 2403-2410.

Sarasam A. & Madihally S.V. (2005). Characterization of chitosan–polycaprolactone blends for tissue engineering applications. *Biomaterials* 26, 5500-5508.

Schröder H.C., Boreiko O., Krasko A., Reiber A., Schwertner H. & Müller W.E.G. (2005). Mineralization of SaOS-2 cells on enzymatically (silicatein) modified bioactive osteoblast-stimulating surfaces. *Journal of Biomedical Materials Research Part B: Applied Biomaterials* 75, 387-392.

Shao H.J., Lee Y.T., Chen C.S., Wang J.H. & Young T.H. (2010). Modulation of gene expression and collagen production of anterior cruciate ligament cells through cell shape changes on polycaprolactone/chitosan blends. *Biomaterials* 31, 4695-4705.

Struszczyk H. (1987). Microcrystalline chitosan. I. Preparation and properties of microcrystalline chitosan. *Journal of applied polymer science* 33, 177-189.

Struszczyk H., Boryniec S. & Ciechañska D. (2003). Studies on the Biodegradation of Microcry-stalline Chitosan in Aqueous Medium. *Fibres & Textiles in Eastern Europe* 11, 40.

Stuart B.H. (2004). Infrared spectroscopy: fundamentals and applications. *John Wiley & Sons, Inc.*

Wan Y., Wu H., Cao X. & Dalai S. (2008). Compressive mechanical properties and biodegradability of porous poly(caprolactone)/chitosan scaffolds. *Polymer Degradation and Stability* 93, 1736-1741.

Wang X., Schröder H.C., Wiens M., Ushijima H. & Mueller W.E.G. (2012). Bio-silica and bio-polyphosphate: applications in biomedicine (bone formation). *Current Opinion in Biotechnology* 23, 570-578.

Wiens M., Niem T., Elkhooly T.A., Steffen R., Neumann S., Schloßmacher U. & Müller W.E.G. (2013). Osteogenic potential of a biosilica-coated P (UDMA-*co*-MPS) copolymer. *Journal of Materials Chemistry B* 1, 3339-3343.

Wiens M., Wang X., Schröder H.C., Kolb U., Schloßmacher U., Ushijima H. & Müller W.E.G. (2010). The role of biosilica in the osteoprotegerin/RANKL ratio in human osteoblast-like cells. *Biomaterials* 31, 7716-7725.

Wilson C.J., Clegg R.E., Leavesley D.I. & Pearcy M.J. (2005). Mediation of biomaterial-cell interactions by adsorbed proteins: a review. *Tissue engineering* 11, 1-18.

Woodruff M.A. & Hutmacher D.W. (2010). The return of a forgotten polymer–polycaprolactone in the 21st century. *Progress in Polymer Science* 35, 1217-1256.

Yang X., Chen X. & Wang H. (2009). Acceleration of osteogenic differentiation of preosteoblastic cells by chitosan containing nanofibrous scaffolds. *Biomacromolecules* 10, 2772-2778.

Zhang Y., Xue C., Xue Y., Gao R. & Zhang X. (2005). Determination of the degree of deacetylation of chitin and chitosan by X-ray powder diffraction. *Carbohydrate research* 340, 1914-1917.

Zhong X., Ji C., Chan A.K., Kazarian S.G., Ruys A. & Dehghani F. (2011). Fabrication of chitosan/poly (ε-caprolactone) composite hydrogels for tissue engineering applications. *Journal of Materials Science: Materials in Medicine* 22, 279-288.

Zhou H., Wei J., Wu X., Shi J., Liu C., Jia J., Dai C. & Gan Q. (2010). The bio-functional role of calcium in mesoporous silica xerogels on the responses of osteoblasts in vitro. *Journal of Materials Science: Materials in Medicine* 21, 2175-2185.

Extended summary

In this study, several methods have been established to immobilize the enzyme silicatein-α on different materials in the frame of various biomedical and biotechnological applications. Thus, silicatein has been immobilized on the surfaces of (*i*) a P(UDMA-*co*-MPS) copolymer, (*ii*) a CHS-*graft*-PCL polymer, (*iii*) fluorescent core/shell silica nanoparticles and (*iv*) gold (111) carriers. The immobilized recombinant enzyme, then, was used as catalyst for surface functionalization *via* formation of biosilica and biotitania from the respective soluble precursors orthosilicate and titanium bis-(ammonium-lactato)-dihydroxide (TiBALDH).

Chapter 2 describes the bioengineering of a silicatein chimera that carries a thiol-bearing cysteine tag. This affinity tag was shown to facilitate binding of the protein onto gold surfaces as patterned self-assembled monolayers *via* the soft-lithography method of microcontact printing. Subsequently, after folding of the immobilized and printed recombinant silicatein, the active enzyme catalyzed the hydrolysis of the TiBALDH at neutral pH, resulting in a mixture of amorphous titania and anatase crystals on the gold surface, according to the printed patterns of silicatein. The immunodetection of the covalently patterned Cys-tagged silicatein on the gold surface with its specific primary antibody confirmed the stability of enzyme as compared to the physisorbed non-Cys-tagged silicatein, even after extensive washing steps. Furthermore, SEM and CLSM images showed the formation of micropatterns with a line width of ca. 7 μm, separated by non-printed gaps of 6 μm according to the patterned PDMS stamp. After incubation with 250 µM TiBALDH, the type of titania polymorph formed on the patterned enzyme was analyzed by Raman spectroscopy as analytical tool for phase identification. Titanium dioxide (TiO_2) has three crystalline polymorphs termed as anatase, brookite, and rutile (Li et al., 2007). Only anatase and rutile have been commonly synthesized and mediated by biomacromolecules in aqueous solution under mild conditions (Chen et al., 2010; Kröger et al., 2006). There is a distinctive difference between the two polymorphs in their Raman bands: Anatase has six Raman bands, $3E_g$ (144, 197 and

639 cm^{-1}), 2B$_{1g}$ (399 and 519 cm^{-1}) and A$_{1g}$ (513 cm^{-1}), while rutile has four Raman bands: A$_{1g}$ (612 cm^{-1}), B$_{1g}$ (143 cm^{-1}), B$_{2g}$ (826 cm^{-1}) and E$_g$ (447 cm^{-1}) (2009 Zhang et al., 2009). In the current study, only Raman bands were identified that are related to anatase and amorphous titania; the later one correlated with a broadening of the bands. The presence of the anatase phase strongly indicates that silicatein facilitates a nucleophilic attack, which results in the hydrolysis of TiBALDH, comparable to the nucleophilic attack of hydroxyl ions resulting in the hydrolysis of TiBALDH at pH >9 (Kinsinger et al., 2010). Photocatalytic experiments have demonstrated that the silicatein-synthesized biotitania was able to degrade organic dyes such as methylene blue upon exposure to ultraviolet and, thus, confirmed the presence of anatase nanocrysals because amorphous titania has only negligible photocatalytic activity (Ohtani et al., 1997). The mechanism by which anatase degrades organic dyes (Alizarin S, crocein orange G, methyl red, congo red, and methylene blue, etc.) could be attributed to the generation of electron-hole pairs, which generate free radicals that are able to undergo secondary reactions (Lachheb et al., 2002; Luo & Ollis, 1996) Furthermore, it has been observed that the anatase phase is photocatalytically more efficient than other types of titanium oxide (Luo & Ollis, 1996). This superiority originates from a band gap of 3.2 eV, as compared to 3.0 eV for rutile. Accordingly, the conductive zone of anatase is 0.2 eV higher and therefore is more favorable for driving conjugate reactions involving electrons. Being able to choose the titania polymorph is highly desirable for various technological applications and remains a challenging task for protein-mediated synthetic pathways. By using biomacromolecules, the synthesis of the TiO$_2$ polymorph can be tailored in an easier approach than compared to the conventional chemical or thermal methods (Chen et al., 2010). In order to elucidate the role of silicatein on the controlled formation of a titania polymorph, the hydrolytic enzyme lysozyme was recently added to a solution of TiBALDH, resulting in the synthesis of anatase nanocrystals (Chen et al., 2010). Furthermore, lysozyme was found responsible for the precipitation of silica nanoparticles from prehydrolyzed tetramethoxysilane (TMOS) (Luckarift et al., 2006). However, the lysozyme-mediated precipitation of silica or titania might be independent from the enzyme active site and, in contrast to silicatein, depend on the presence of a large amount of hydroxy- and

imidazole-containing amino acid residues of lysozyme (Luckarift et al., 2006; Chen et al., 2010).. Furthermore, silafin (a biosilicifiying protein of diatoms but no enzyme) was reported to contribute to the formation of rutile microcrystals in a non-enzymatic pathway, suggesting a different mechanism for the silicatein-catalyzed formation of biosilica and biotitania (Kröger et al., 2006). In conclusion, microcontact printing (µCP) of silicatein represents offered a simple, flexible, efficient and well-adapted soft-lithographic technique. The covalent bonding of cysteine-tagged silicatein to gold surfaces facilitated the formation of micropatterned titania with photocatalytic activity, according to the printed patterns of silicatein. The range of possible applications could be expanded by applying different silicatein substrates (e.g. gallium nitrate or hexafluorozirconate), which would result in additional patterned metal(loid) oxides with different properties (Brutchey & Morse, 2008).

Chapter 3 describes the bioinspired modification of tyrosine residues on the silicatein surface *via* tyrosinase. The post-translational modification of tyrosine residues of mussel foot proteins to DOPAquinone and DOPA grants both exceptional intermolecular cross-linking and adhesive properties. Accordingly, the objective of the presented study was to establish a simple and fast method by exploring these properties for the formation of mesoscale fibers, consisting of silicatein and fluorescent core/shell silica nanoparticles, for biotechnological application. For a similar objective, β-lactoglobulin amyloid fibrils were used as template to generate closely packed TiO_2 nanoparticles on their surface for photovoltaic devices, organo-electronics and hybrid solar cells (Bolisetty et al., 2012). In case of silicatein, however, the *in vitro* fabrication of self-assembled mesostructures has not been possible so far, in particular because the required protein concentration could not be generated. Accordingly, a new methodological approach for the purification and subsequent folding of silicatein was established. This procedure was based on a reverse dilution method that minimizes the aggregation of partially folded silicatein intermediates. Until then, extraction of recombinant silicatein from inclusion bodies involved high concentrations (6 M) of chaotropic reagents such as urea or guanidine-HCl to solubilize the denatured protein. The former denaturants are efficient on maintaining the solubility of the protein but cause protein denaturation and,

hence, are not compatible with folding procedures. The established procedure for silicatein folding was based on a slow reduction of the denaturant concentrations by slow and drop-wise addition of the refolding buffer to the protein solution and subsequent pelleting of any potentially formed protein aggregate after each dilution step. The yield of silicatein thus obtained was much higher than the yield of silicatein conventionally prepared by dialysis (ca. 1 mg/ml vs. 750 µg/ml). Moreover, the protein could be subsequently concentrated, lyophilized, and resolubilized in its aqueous solvent, allowing concentrations of several milligrams of soluble protein per milliliter. These preparations were used to assess *via* micro-Raman spectroscopy both secondary structures and conformational change of silicatein upon oligomerization in an aqueous environment. The data revealed for example that the secondary structure of silicatein monomers comprises 26 % of α-helices immediately after dissolution of the protein in Tris-HCl buffer at neutral pH. However, after 30 min the predominant secondary structure switched from α-helix to β-sheet due to the oligomerization and the self-assembly of silicatein. These observations are indicative of the hydrophobic interaction and filament formation of silicatein monomers, which have been described previously (Müller et al., 2013). By treating a high concentration of soluble silicatein (2.5 mg/ml) with tyrosinase, the tyrosine residues on the silicatein surface were oxidized to DOPA residues and, subsequently, to DOPAquinone residues that were shown to enhance the cross-linking of silicatein oligomers to microscale aggregates. Through self-assembly of these aggregates silicatein microfibers were obtained. These microfibers were used in an aqueous medium as template for the deposition of core/shell fluorescent silica nanoparticles, ultimately resulting in fluorescent hybrid mesofibers. The molecular self-assembly of silicatein aggregates occurred *via* non-covalent interactions. This might be related to the three hydrophobic recognition sites identified on the silicatein surface that are accessible to the aqueous solvent (Murr et al., 2009). Hydrophobic interaction was reported to contribute significantly in the stabilization of fibril peptides and self-assembly of proteins in aqueous environments (Meijer et al., 2007). In a different approach using tyrosinase treated silicatein oligomers, the core/shell fluorescent silica nanoparticles were first coated with silicatein by converting DOPAquinone to cohesive DOPA residues in a reducing regime by using

ascorbic acid. The conversion from DOPAquinone to DOPA residues was confirmed by infrared spectroscopy, as the band corresponding to DOPAquinone significantly reduced in its intensity. Thereafter, due to the hydrophobic recognition sites on the silicatein surface (scheme 1.2), an inorganic-organic fibrous composite was assembled, exhibiting well-integrated and -distributed inorganic particles within the protein matrix. This novel immobilization has significantly decreased the relatively large number of steps required for conventional conjugation of biomacromolecules onto silica particles (e.g. Knopp et al., 2009): Usually, the assembly of silica particles into defined pattern or hierarchical structures is mediated by immobilization of biomacromolecules with specific recognition motif on their surfaces. For instance, β-cyclodextrin was immobilized previously on silica particles *via* covalent bonding to permit their assembly into 2D patterns (Mahalingam et al., 2004). The former immobilization technique requires surface modification of the silica particles with carboxyl or amine groups and subsequently interaction with the functional groups of the biomacromolecules *via* active ester intermediates. Our novel method of immobilization is not restricted to silicatein as it can be applied to various other proteins with surface tyrosine residues or even to partially unfolded proteins that are rich in tyrosine residues and are considered as good candidates for tyrosinase treatment (Hellman et al., 2011). To the best of our knowledge, this is the first report wherein tyrosinase is used to modify the surface tyrosine residues of any protein for their direct immobilization onto nanoparticles surface to mediate the assembly of organic–inorganic composite. However, in another recent approach tyrosinase has been used to immobilize onto TiO_2 surfaces the cytoskeleton F-actin recognizing peptide (RGD-Y) bearing terminal tyrosine residue *via* a metal coordinate covalent bond (Park & Park, 2011).

In contrast to the aforementioned approaches with their considerable biotechnological potential, in Chapter 4 and 5 silicatein/biosilica-based approaches are presented that have improved the osteoinductive and osteogenic properties of different organic biocompatible polymers, which are conventionally used as bone substitutes and for bone regeneration. It is well established that the incorporation of biosilica in different biomaterials promotes the biomineralizing activity of osteoblasts and, concurrently,

represses the demineralizing activity of osteoclasts (Wiens et al., 2010b). However, by which mechanisms biosilica affects cellular mineralization is not completely understood. Nevertheless, biosilica had been shown to upregulate the expression of the bone morphogenetic protein-2 (BMP-2) (Wiens et al., 2010a), which belongs to the transforming growth factor (TGF)-β-family of growth factors and is considered an osteoinductive agent (Albrektsson & Johansson, 2001). Concurrently, biosilica was previously shown to promote the expression of osteoinductive proteins such as osteoprotegerin (OPG) and alkaline phosphatase (ALP) (Wang et al., 2012; Wiens et al., 2010b). Consequently, biosilica should be considered an indirect osteoinductive agent that is able to accelerate the differentiation of immature osteoblastic cells and to promote the biomineralization of osteoblastic cells. Accordingly, synthetic biomaterial scaffolds that have only osteoconductive properties were functionalized with biosilica *via* immobilized silicatein.

In chapter 4, photo-induced free radical polymerization was used to polymerize the bifunctional monomers of methacryloxypropyltrimethoxysilane (MPS), which carry a terminal vinyl group and can be copolymerized with urethane dimethacrylate (UDMA) as a cross-linker between the MPS chains. These acrylate-based polymers have a long history for being used as bone cement and inlay for both orthopedic and dental applications, respectively (Farrar, 2012). Due to the bifunctionality of MPS, which belongs to silane coupling agent compounds, the resulting P(UDMA-*co*-MPS) copolymer after photopolymerization carries ethoxy groups that can be converted to silanol groups through acid hydrolysis. The conversion of ethoxy groups to silanol groups has been confirmed by infrared spectroscopy. These silanol groups proved to be good anchors for silicatein immobilization because of their ability to form hydrogen bonds with the surface accessible serine clusters of silicatein (Müller et al., 2008). Silicatein immobilization onto silanol-rich surface was confirmed by immunoassay with a combination of primary silicatein antibodies and secondary Cy3-labeled species-specific antibodies. Subsequently, the polymeric surfaces coated with silicatein were inspected with confocal laser microscope.

On the other hand, in Chapter 5, low percentages of the hydrophobic polymer polycaprolactone (PCL) were covalently grafted on to the backbone of hydrophilic polymer chitosan (CHS) by using cross-linking agents DCC/NHS, with the overall aim to synthesize an amphiphilic polymer as carrier for silicatein and biosilica. Thus, the carboxylic acid terminus in PCL was initially activated with active ester intermediates (DCC/NHS) to facilitate stable amide bonding with deprotonated amine groups of CHS. After grafting of both polymers *via* covalent amide linkage, the resultant polymeric bulk material exhibited gummy-like properties with high flexibility and moldability, allowing the fabrication of customized scaffolds for orthopedic application. Furthermore, the structural analyses including infrared spectroscopy and X-ray diffraction revealed the formation of secondary amide bonds, confirming the conjugation of both polymers and the increased crystallinity of the resultant graft due to the formation of microcrystalline chitosan (MCCS), respectively. Generally, the response of cells upon growth on crystalline polymers is dependent on the cell type. Thus, adhesion, proliferation, and differentiation of cells might be promoted or inhibited, based on how the specific cell type interacts with the higher surface roughness and stiffness induced by polymer crystallization (Wang et al., 2010; Washburn et al., 2004; Helen & Sinko, 2012). Therefore, the surface of CHS-*g*-PCL specimens has been functionalized with silicatein to mediate the subsequent formation of an osteoconductive/osteoinductive biosilica layer that improves the cellular response, independent of the cell type to be used. For silicatein immobilization, the carbonyl groups of PCL in the grafted polymers (CHS-*g*-PCL) were further aminolyzed with diamine, generating protonated amine groups that facilitate binding of the negatively charged silicatein at neutral pH (PI~5) to CHS-*g*-PCL specimens through ionic interactions. The immobilized silicatein, then, was used to mediate the polycondensation of orthosilicic acid in order to functionalize the graft surface with osteogenic biosilica. Immobilized silicatein was visualized by immunodetection, Coomassie staining, and atomic force microscopy. Furthermore, quantification of the protein immobilized on the aminolyzed surfaces revealed a considerably higher amount of silicatein (ca. 200 $\mu g/cm^2$) compared to the non-functionalized surface (ca. 100 $\mu g/cm^2$).

The polymers used in the current study, which are either natural such as chitosan or synthetic such as polycaprolactone and derivatives of acrylate, are usually non-osteogenic materials: They lack the functional groups that act as specific ligands for binding to receptors on the bone cell surface and, consequently, intracellular signaling cascade(s) involved in bone formation can not be triggered (Wang et al., 2013). Therefore, functionalization of the polymer surfaces is required, e.g. through immobilization of the RGD peptide or cytokines and growth factors. As mentioned above, enzymatically-synthesized biosilica can be used alternatively as an indirect osteoinductive layer on the material surface to enhance osteoblast adhesion, proliferation, differentiation and mineralization. For evaluation of cellular biomineralization, the frequently used stains Alizarin Red S and Osteoimage were employed. Whereas Alizarin Red S binds to the calcium of calcium phosphate, the fluorescence dye Osteoimage specifically detects hydroxyapatite (Langenbach et al., 2011). According to both approaches, both biosilica-functionalized P(UDMA-*co*-MPS) and CHS-*g*-PCL demonstrated a significant increase in hydroxyapatite deposition after growth of osteoblast-like cells (SaOS-2) compared to non-functionalized polymers. This enhanced mineralization of SaOS-2 cells correlated with an increased ALP activity at different time points. Among the major osteogenic markers, an upregulated ALP activity is considered a key event during early osteogenesis. Our results indicate that biosilica can promotes ALP activity even without the addition of further osteogenic supplements (10 nM dexamethasone, 50 µM ascorbic acid, and 5 mM β-glycerophosphate), as has been illustrated in Chapter 5 after four days incubation with SaOS-2 cell line. Surprisingly, when SaOS-2 cells were cultivated on CHS-*g*-PCL samples that carried only immobilized silicatein but no biosilica, an enhanced HA formation was observed. This phenomenon might be caused by the enzymatic activity of silicatein, which converted silicate that is always present in cell media to biosilica. However, and most likely, the mechanism might be correlated with to the high content of aspartate (5%), tyrosine (7.5%) and serine (13.5%) amino acid residues in the mature sequence of silicatein ($aa_{115-330}$). These amino acids, if present on the protein surface, are responsible for heterogeneous nucleation and deposition of hydroxyapatite by attracting calcium and phosphate ions within the culture medium, especially upon formation of a

solid interface on the material surface upon silicatein oligomerization. On the other hand, these amino acids might have a bioactive influence on the adhesion and proliferation of osteoblast-like cells as has been suggested previously for sericin proteins, which have a high content of serine and aspartic acid residues (Zhang et al., 2008). Moreover, sericin-functionalized surfaces improved the ALP activity of osteoblasts similar to the increased ALP activity observed on silicatein-coated CHS-*g*-PCL surfaces that had been incubated with SaOS-2 cells without osteogenic medium. However, the molecular signal cascades that trigger ALP activity remain enigmatic for both silicatein and sericin. Furthermore, microscopic analyses of SaOS-2 cells grown on the surface of CHS-*g*-PCL coated with biosilica showed the flattened polygonal morphology of cells that are well spread and differentiated as compared to the control. Therefore, it can be concluded that with the enzymatically controlled surface-functionalization of biomaterial carrier *via* silicatein and orthosilicate, inorganic/organic composite materials could be fabricated with inherent osteogenic potential.

In several previous studies four potential explanations for the osteogenic potential of silica have been proposed. Firstly, silica that might occur in the extracellular matrix or in the cytoplasm upon endocytosis, can affect gene expression of osteoblastic cells due to the release of silicate ions (Quignard et a., 2012). It was reported that the degradation of silica nanoparticles in silk fibroin matrices enhances the gene expression of bone sialoprotein (BSP) and collagen type 1 (Col 1) in human mesenchymal stem cells (hMSCs) (Mieszawska et al., 2010). It was shown recently that small particle sizes (diameter, ~ 10 nm) of the negatively charged silica decrease fibroblast cell viability, probably due to the interaction of silica with nuclei and/or DNA or the formation of free radicals that cause oxidative stress (Quignard et al., 2012). However, in case of silicatein-synthesized biosilica, particles sizes of up to 300 nm were observed (Tahir et al., 2004), which have no negative impact on cell viability. The intracellular dissolution of these biogenic particles might activate the expression of osteoinductive proteins (Quignard et al., 2012). Otherwise, the negatively charged silanol groups of silica might be responsible for the acellular deposition of positively charged calcium ions in the cell culture medium by electrostatic interaction. This process is usually fast and followed by

another ionic interaction between the interfacial calcium and phosphate ions, forming an amorphous phase of calcium phosphate (ACP) layer on the surface. Because of its amorphous nature, re-dissolution of ACP causes a locally increased ion concentration around osteoblasts, which seems to be responsible for osteoinduction properties of silica, by trigging the expression of osteocalcin (OCN), bone sialoprotein (BSP) (Chou et al., 2005) and ALP (Golub & Boesze-Battaglia, 2007). Finally, the nanoroughness provided by a coated layer of silica nanoparticles appears to be favorable for cell differentiation because it promotes cell stasis and arrests their locomotion (Lipski et al., 2008). Because of all aforementioned impacts of silica nanoparticles on the osteogenic behaviors of bone building cells, the integration of biosilica with different biomaterials either on the surface or within the matrix might greatly enhance their performance and applicability. They are not only capable of forming direct bonds to the host bone *via* acellular hydroxyapatite deposition (osteoconductive property) but also can induce expression of the osteoinductive mediators required for enhancing the cellular mineralization capacity (osteogenic property).

References

Albrektsson T. & Johansson C. (2001). Osteoinduction, osteoconduction and osseointegration. *European Spine Journal* 10, S96-S101.

Bernard A., Renault J.P., Michel B., Bosshard H.R. & Delamarche E. (2000). Microcontact printing of proteins. *Advanced Materials* 12, 1067-1070.

Bolisetty S., Adamcik J., Heier J. & Mezzenga R. (2012). Amyloid Directed Synthesis of Titanium Dioxide Nanowires and Their Applications in Hybrid Photovoltaic Devices. *Advanced Functional Materials* 22, 3424-3428.

Brutchey R.L. & Morse D.E. (2008). Silicatein and the translation of its molecular mechanism of biosilicification into low temperature nanomaterial synthesis. *Chemical reviews* 108, 4915-4934.

Chen G., Li M., Li F., Sun S. & Xia D. (2010). Protein-Mediated Synthesis of Nanostructured Titania with Different Polymorphs at Room Temperature. *Advanced Materials* 22, 1258-1262.

Chou Y.F., Huang W., Dunn J.C., Miller T.A. & Wu B.M. (2005). The effect of biomimetic apatite structure on osteoblast viability, proliferation, and gene expression. *Biomaterials* 26, 285-295.

Farrar D.F. (2012). Bone adhesives for trauma surgery: A review of challenges and developments. *International Journal of Adhesion and Adhesives* 33, 89-97.

Golub E.E. & Boesze-Battaglia K. (2007). The role of alkaline phosphatase in mineralization. *Current Opinion in Orthopaedics* 18, 444-448.

Guo C., Ge M., Liu L., Gao G., Feng Y. & Wang Y. (2010). Directed synthesis of mesoporous TiO_2 microspheres: catalysts and their photocatalysis for bisphenol A degradation. *Environmental science & technology* 44, 419-425.

Helen C.U.I. & SINKO P.J. The role of crystallinity on differential attachment/proliferation of osteoblasts and fibroblasts on poly (caprolactone-co-glycolide) polymeric surfaces. *Frontiers of Materials Science* 6, 47-59.

Hellman M., Mattinen M.L., Fu B., Buchert J. & Permi P. (2011). Effect of protein structural integrity on cross-linking by tyrosinase evidenced by multidimensional heteronuclear magnetic resonance spectroscopy. *Journal of biotechnology* 151, 143-150.

Kinsinger N.M., Wong A., Li D., Villalobos F. & Kisailus D. (2010). Nucleation and Crystal Growth of Nanocrystalline Anatase and Rutile Phase TiO_2 from a Water-Soluble Precursor. *Crystal Growth & Design* 10, 5254-5261.

Knopp D., Tang D. & Niessner R. (2009). Review: bioanalytical applications of biomolecule-functionalized nanometer-sized doped silica particles. *Analytica chimica acta* 647, 14-30.

Kröger N., Dickerson M.B., Ahmad G., Cai Y., Haluska M.S., Sandhage K.H., Poulsen N. & Sheppard V.C. (2006). Bioenabled synthesis of rutile (TiO_2) at ambient temperature and neutral pH. *Angewandte Chemie* 118, 7397-7401.

Lachheb H., Puzenat E., Houas A., Ksibi M., Elaloui E., Guillard C. & Herrmann J.M. (2002). Photocatalytic degradation of various types of dyes (Alizarin S, Crocein Orange G, Methyl Red, Congo Red, Methylene Blue) in water by UV-irradiated titania. *Applied Catalysis B: Environmental* 39, 75-90.

Langenbach F., Berr K., Naujoks C., Hassel A., Hentschel M., Depprich R., Kubler N.R., Meyer U., Wiesmann H., Kögler G. & Handschel J. (2011). Generation and differentiation of microtissues from multipotent precursor cells for use in tissue engineering. *Nature protocols* 6, 1726-1735.

Li J.G., Ishigaki T. & Sun X. (2007). Anatase, brookite, and rutile nanocrystals via redox reactions under mild hydrothermal conditions: phase-selective synthesis and physicochemical properties. *The Journal of Physical Chemistry* C 111, 4969-4976.

Lipski A.M., Pino C.J., Haselton F.R., Chen I. & Shastri V.P. (2008). The effect of silica nanoparticle-modified surfaces on cell morphology, cytoskeletal organization and function. *Biomaterials* 29, 3836-3846.

Luckarift H.R., Dickerson M.B., Sandhage K.H. & Spain J.C. (2006). Rapid, Room-Temperature Synthesis of Antibacterial Bionanocomposites of Lysozyme with Amorphous Silica or Titania. *Small* 2, 640-643.

Luo Y. & Ollis D.F. (1996). Heterogeneous photocatalytic oxidation of trichloroethylene and toluene mixtures in air: kinetic promotion and inhibition, time-dependent catalyst activity. *Journal of Catalysis* 163, 1-11.

Mahalingam V., Onclin S., Péter M., Ravoo B.J., Huskens J. & Reinhoudt D.N. (2004). Directed self-assembly of functionalized silica nanoparticles on molecular printboards through multivalent supramolecular interactions. *Langmuir* 20, 11756-11762.

Meijer J.T., Roeters M., Viola V., Löwik D.W., Vriend G. & van Hest J.C. (2007). Stabilization of peptide fibrils by hydrophobic interaction. *Langmuir* 23, 2058-2063.

Mieszawska A.J., Fourligas N., Georgakoudi I., Ouhib N.M., Belton D.J., Perry C.C. & Kaplan D.L. (2010). Osteoinductive silk–silica composite biomaterials for bone regeneration. *Biomaterials* 31, 8902-8910.

Müller W.E., Schröder H.C., Muth S., Gietzen S., Korzhev M., Grebenjuk V.A., Wiens M., Schloßmacher U. & Wang X. (2013). The silicatein propeptide acts as inhibitor/modulator of self-organization during spicule axial filament formation. *FEBS Journal* 280, 1693-1708.

Müller W.E., Jochum K.P., Stoll B. & Wang X. (2008). Formation of giant spicule from quartz glass by the deep sea sponge Monorhaphis. *Chemistry of Materials* 20, 4703-4711.

Murr M.M., Thakur G.S., Li Y., Tsuruta H., Mezic I. & Morse D.E. (2009). New pathway for self-assembly and emergent properties. *Nano Today* 4, 116-124.

Ohtani B., Ogawa Y. & Nishimoto S.I. (1997). Photocatalytic activity of amorphous-anatase mixture of titanium (IV) oxide particles suspended in aqueous solutions. *The Journal of Physical Chemistry B* 101, 3746-3752.

Park K.M. & Park K.D. (2011). Facile surface immobilization of cell adhesive peptide onto TiO2 substrate via tyrosinase-catalyzed oxidative reaction. *Journal of Materials Chemistry* 21, 15906-15908.

Quignard S., Mosser G., Boissière M. & Coradin T. (2012). Long-term fate of silica nanoparticles interacting with human dermal fibroblasts. *Biomaterials* 33, 4431-4442.

Tahir M.N., Théato P., Müller W.E.G., Schröder H.C., Janshoff A., Zhang J., Huth J. & Tremel W. (2004). Monitoring the formation of biosilica catalysed by histidine-tagged silicatein. *Chemical communications* 024, 2848-2849.

Wang K., Cai L., Hao F., Xu X., Cui M. & Wang S. (2010). Distinct Cell Responses to Substrates Consisting of Poly (ε-caprolactone) and Poly (propylene fumarate) in the Presence or Absence of Cross-Links. *Biomacromolecules* 11, 2748-2759.

Wang X., Schröder H.C., Feng Q., Draenert F. & Müller, W.E.G. (2013). The Deep-Sea Natural Products, Biogenic Polyphosphate (Bio-PolyP) and Biogenic Silica (Bio-Silica), as Biomimetic Scaffolds for Bone Tissue Engineering: Fabrication of a Morphogenetically-Active Polymer. *Marine drugs* 11, 718-746.

Wang X., Schröder H.C., Wiens M., Ushijima H., & Mueller W.E.G. (2012). Bio-silica and bio-polyphosphate: applications in biomedicine (bone formation). *Current Opinion in Biotechnology* 23, 570-578.

Washburn N.R., Yamada K.M., Simon Jr C.G., Kennedy S.B. & Amis E.J. (2004). High-throughput investigation of osteoblast response to polymer crystallinity: influence of nanometer-scale roughness on proliferation. *Biomaterials* 25, 1215-1224.

Wiens M., Wang X., Schloßmacher U., Lieberwirth I., Glasser G., Ushijima H., Schröder H.C.& Müller W.E.G (2010 a). Osteogenic potential of biosilica on human osteoblast-like (SaOS-2) cells. *Calcified tissue international* 87, 513-524.

Wiens M., Wang X., Schröder H.C., Kolb U., Schloßmacher U., Ushijima H. & Müller, W.E.G. (2010 b). The role of biosilica in the osteoprotegerin/RANKL ratio in human osteoblast-like cells. *Biomaterials* 31, 7716-7725.

Zhang F., Zhang Z., Zhu X., Kang E.T. & Neoh K.G. (2008). Silk-functionalized titanium surfaces for enhancing osteoblast functions and reducing bacterial adhesion. *Biomaterials* 29, 4751-4759.

Zhang Z., Brown S., Goodall J., Weng X., Thompson K., Gong K., Kellici S., Clark R.J.H., Evans J.R.G. & Darr J.A. (2009). Direct continuous hydrothermal synthesis of high surface area nanosized titania. *Journal of Alloys and Compounds* 476, 451-456.

List of Figures

Erklärung

Hiermit versichere ich, die vorliegende Arbeit selbständig verfasst und keine anderen als die genannten Hilfsmittel verwendet zu haben. Des weiteren versichere ich, dass diese Dissertation nicht als Prüfungsarbeit für eine andere Prüfung oder die gleiche oder Teile der Abhandlung als Dissertation bei einer anderen Fakultät oder einem anderen Fachbereich eingereicht wurde.

Mainz,